J. Fluid Mech. (1998), *vol.* 365, *pp.* 23–88. Printed in the United Kingdom

Physical analysis of the transition to turbulence in the wake of a circular cylinder by three-dimensional Navier–Stokes simulation

By HÉLÈNE PERSILLON AND MARIANNA BRAZA

Institut de Mécanique des Fluides de Toulouse, Unité Mixte de Recherche CNRS-INPT N° 5502, Avenue du Professeur Camille Soula, 31400 Toulouse, France

(Received 11 June 1996 and in revised form 23 December 1997)

The transition to turbulence of the flow around a circular cylinder is studied by a three-dimensional numerical simulation of the Navier–Stokes equations system in the Reynolds number range 100–300. The numerical method is second-order accurate in space and time and Neumann boundary conditions are used at the two boundaries in the spanwise direction; non-reflecting boundary conditions are specified for the outlet downstream boundary. This study predicts the frequency modulation and the formation of a discontinuity region delimited by two frequency steps within the present Reynolds number range. These features are related to the birth of streamwise vorticity and to the kinetic energy distribution in the near wake. The development of the mean dynamic quantities, the Reynolds stress correlations and the variation of their maximum values are provided in this region, where the similarity laws do not hold. The spatial evolution of the von Kármán mode and of its spectral amplitude are quantified and the variation laws of the maximum spectral amplitude and of its location as a function of Reynolds number are established. The critical Reynolds number for the appearance of the first discontinuity in the present flow system is evaluated by the fully nonlinear approach.

1. Introduction

The study of the transition to turbulence and the wake formation behind bluff bodies has received a great deal of attention over more than a century from an experimental and a numerical point of view. Concerning the experimental studies, Roshko (1954) first observed the existence of a transition regime in the wake of the cylinder and found distinct irregularities in the wake velocity fluctuation. He showed that there exist three different regimes of the flow at low to moderate Reynolds number, which are the laminar, transition and irregular turbulent regimes. In the transition regime, he reported distinct irregularities in the wake velocity fluctuation. Bloor (1964) suggested that the low-frequency irregularities obtained experimentally are related to the presence of three-dimensionalities in the flow which lead to the development of turbulent motion farther downstream. The inception of small-scale structures in the wake (Hama 1957; Gerrard 1966, 1978) has been also associated with the transition regime.

In the late eighties, Williamson (1988*a*, *b*, 1992) and Eisenlohr & Eckelmann (1989) achieved new insight into the transition to turbulence in the wake of a circular cylinder, concerning the conditions of the parallel vortex shedding mode and the

Strouhal–Reynolds number relationship in the low Reynolds number range. These studies provided a thorough analysis of the vortex shedding fundamental frequency relation with Reynolds number and explained the reasons for the appearance of a considerable difference in this frequency according to different experimental works in terms of the end conditions in the spanwise direction. Therefore, the end conditions were set in order to ensure parallel shedding and to provide a universal Strouhal–Reynolds number relationship (Williamson 1988 *a*, *b*). Furthermore, Williamson (1992) observed the existence of two modes of formation of streamwise vorticity in the near wake, each occurring at a different range of Reynolds numbers and both being related to the three-dimensional transition between Reynolds numbers from 180 to 260. The first mode occurs beyond Reynolds number 180 and is characterized by a discontinuous change in the wake formation as the primary vortices become unstable and generate large-scale vortex loops. The second, beyond Reynolds number 240, corresponds to the appearance of small-scale streamwise vortex structures. Both modes involve length scales of the streamwise vortex structures which are less than one primary wavelength of the vortex street. Moreover, Williamson (1992) demonstrated that the transition regime involves massive spot-like structures caused by 'vortex dislocations' which form between spanwise cells of different frequency, when the main von Kármán vortices in each cell move out of phase with each other. He reported a growth of these structures to a size of the order of 10–20 primary wavelengths. He suggests that this phenomenon is mostly responsible for the low-frequency fluctuations (large intermittent velocity irregularities) reported by Roshko and Bloor to characterize the transition regime and the appearance of the turbulence motion.

The same kinds of physical phenomena have been observed in other experimental works for different body shapes, such as reported by Gaster (1969), for slender cone configurations and recently in an extended study by Leweke & Provansal (1995) for the wake of a cylinder and of a torus. These phenomena, which apparently have a general character in the process of transition to turbulence constitute fascinating challenges to analyse by means of numerical simulation.

Among the experimental and theoretical studies devoted to the analysis of the transition to turbulence in the wake of the circular cylinder, a detailed investigation of the first bifurcation for the Bénard–Kármán instability near the oscillation threshold is offered by Provansal, Mathis & Boyer (1987). Above this threshold, the oscillatory behaviour of the flow is studied and well described by the Stuart–Landau model. According to that study, the nonlinearity is essential to evaluate the correct amplitudes of the instability process, although it plays a minor role in the determination of the values of the fundamental frequency oscillations. It is also clearly pointed out by the authors that their phenomenological approach does not describe the vortex shedding mechanism any better than the exact Navier–Stokes equations do.

Concerning the analysis of this flow in the moderate Reynolds number range (100 to 300), the detailed experimental and theoretical study provided by Leweke & Provansal (1995) for the wakes of a cylinder and a torus gives a more universal character to the frequency modulations in the discontinuity regions related to the transition to turbulence in wakes around bodies. The waviness of the vortex street occurring in the vicinity of the first discontinuity has been attributed, according to that work, to an Eckhaus instability and it was proved that the mechanism can be represented satisfactorily by the Guinzburg–Landau model equation. Indeed, this model has been employed in that study as an extension of the Landau model, valid for the lower Reynolds number regime (40–50), towards the higher Reynolds

number range (150–300). In that study, the instability of the periodic vortex shedding marking this higher transition range has been characterized as the Benjamin–Feir instability of the coupled oscillation of the near wake. Also the Strouhal–Reynolds number relationship including the first discontinuity point has been qualitatively reproduced by the Ginzburg–Landau model. In fact this model was firstly employed to investigate time-periodic phenomena occurring at Reynolds number values less than 180 by Albarède & Provansal (1995), where also the chevron pattern was related to this model.

From the numerical point of view, in the last twenty years a large number of numerical studies have been devoted to the analysis of the unsteady flow around a circular cylinder in the low and moderate Reynolds number regimes. The majority of these numerical simulations used the two-dimensional approach for solving the Navier–Stokes equations. As a general characteristic, the majority of them predicted the first bifurcation of the flow system leading to vortex shedding at a Reynolds number higher than 40. These studies include the works of Lin, Pepper & Lee (1976), Jain & Rao (1969) Son & Hanratty (1969), Jordan & Fromm (1972), Daube & Ta Phuoc Loc (1978), Martinez (1978), Ha Minh, Boisson & Martinez (1980), Braza (1981, 1986), and Braza, Chassaing & Ha Minh (1986). These studies provided results in the range of Reynolds numbers 40–500 and were able to simulate correctly the pattern of the alternate vortices in the wake. Furthermore, Braza *et al*. (1986) analysed the birth of secondary vortices in the established flow with vortex shedding at $Re = 1000$ and their interactions with the main alternating vortices. Braza, Chassaing & Ha Minh (1990) showed the generation of the mixing layer vortices in the separated shear layers past the circular cylinder and assessed of their shedding frequency related to the fundamental frequency in the Reynolds number range 2000–10 000. More recent studies by Braza, Persillon & Sers (1993) obtained the maximum amplitude of the shear-layer transition wave frequency in the flow around a circular cylinder for Reynolds numbers 20 000 and 30 000. Concerning the low Reynolds number regime, which is of interest for the present paper, Braza & Sers (1993) and Sers (1992) evaluated the vortex shedding frequency to within one percent of accuracy the physical experiments by Williamson (1988 *a*, *b*), in the Reynolds number ranges 100–180 and 220–300, i.e. outside the range of appearance of fundamental frequency modulations. These studies established clearly the grid spacing, time step and distance of the outlet boundary requirements for the accurate evaluation of the vortex shedding phenomenon with a comparable accuracy to the recent physical experiments, concerning the parallel shedding conditions, using the two-dimensional approach.

However, these numerical studies are two-dimensional simulations of the flow around a circular cylinder, hence none of the three-dimensional phenomena related to the birth of turbulence and observed in experimental studies are taken into account. The lack of significant three-dimensional numerical simulations during the early '90s was due to limitations imposed by the capabilities of existing supercomputers, in respect to the high complexity of the present category of wake flows around bodies of non-Cartesian geometry. The correct simulation of such flows needs a very large computational domain, owing to their non-confined character, and to the need of very fine grids in the vicinity of the solid wall. For all these reasons, reliable three-dimensional numerical simulations of this category of flows have only very recently appeared, due to the increased capacities and evolution of supercomputing technology.

Karniadakis & Triantafyllou (1992) have computed the three-dimensional flow around a circular cylinder in the Reynolds number range 200–500, by using the

spectral-element method by Patera (1984). They suggested a scenario for the route to chaos of the flow transition, through period-doubling mechanisms. Our work in the investigation of three-dimensional transition mechanisms in the flow around a circular cylinder has developed during the last four years in the context of the Doctoral thesis of Persillon (1995) and we have reported the first direct numerical simulation of the fundamental frequency modulation in the Reynolds number range 100 to 300, as a striking purely three-dimensional effect (Braza 1994; Persillon & Braza 1995; Persillon *et al.* 1995 *a*, *b*; Persillon, Braza & Jin 1995 *c*). During the same period, other numerical studies were also devoted to the three-dimensional transition of the present flow. Thompson, Hourigan & Sheridan have shown the formation of modes A and B in the Reynolds numbers regime (180–190), first, found experimentally by Williamson. Zhang *et al*. (1995) report the existence of a frequency discontinuity in the *Re* range (185–190). Henderson & Barkley (1996), Barkley & Henderson (1996) also report the appearance of this local discontinuity and perform a detailed linear Floquet stability analysis of it.

The recent three-dimensional numerical simulations of this flow give a more and more detailed insight to the present transition process. However, it should be mentioned that, while the majority of them only simulate the formation of one localized discontinuity, our studies in the period 1994–1995 clearly show the formation of a frequency decrease region and the existence of two discontinuities in the Strouhal–Reynolds number relation in the *Re* range 180–300. The analysis and the physical reasons for the appearance of this discontinuity region are part of the main objectives of the present paper.

Moreover, according to the recent three-dimensional numerical studies mentioned, the main instability properties are triggered by imposing a set of perturbations on the (already) fluctuating flow field. It is noticeable that in the present study, the instability properties discussed are provided spontaneously by only the solution of the three-dimensional system of the Navier–Stokes equations. Another important feature which will be discussed in the paper is that in most of the three-dimensional simulations referenced the vortex shedding pattern loses its alternating character within one diameter downstream, while, in the physical experiments, for example the collected flow visualizations reported by Van Dyke (1982), the alternating vortex pattern in the range 100–300 must persist over a long and significant distance downstream. This will be clearly shown in the § 6.2 of the present paper.

More insight into the present complex phenomenon of the transition to turbulence in the cylinder's wake can be obtained by evaluating the critical Reynolds numbers marking the successive changes of the flow as the Reynolds number increases. Concerning the numerical determination of the critical Reynolds number for the appearance of the first bifurcation, in a very interesting study Jackson (1987) develops an efficient method of evaluation of the critical Reynolds number for the appearance of the alternating vortex street regime in two dimensions. This study, using a finite-element method, investigated the passage from steady to periodic flow, which is marked by a supercritical Hopf bifurcation, whose critical Reynolds number is evaluated by the solution of an appropriate set of the steady-state Navier–Stokes equations. This study evaluated the critical Reynolds number of the first bifurcation as 46.184 and the Strouhal number as 0.13804, by performing a very detailed grid-dependence study.

Furthermore, Dusek, Le Gal & Fraunié (1994) perform a detailed analysis of the flow system in the vicinity of this critical Reynolds number and examine the validity of the Landau model near the threshold, by using the two-dimensional Navier–

Stokes equations. This study suggests an original way to distinguish three separate time scales, for the periodic motion, the amplification and the deformation of the mode.

Concerning the theoretical and numerical investigation of the critical Reynolds number for the first discontinuity, there have been a few attempts to determine its value, mostly by using the linear approach. For the Reynolds number range before the first discontinuity, a global three-dimensional stability analysis of this flow was performed, by using a low-dimensional Galerkin method by Noack & Eckelmann (1994). According to that study, the flow below $Re = 54$ was found to be stable to all perturbations. The authors describe the onset of periodicity as a supercritical Hopf bifurcation, also modelled by the Landau equations, and report that while two-dimensional perturbations rapidly damp, three-dimensional perturbations with long spanwise wavelengths neither grow nor decay. They report that the periodic solution becomes unstable at $Re = 170$ and that this instability is also a supercritical Hopf bifurcation in the spanwise direction the result being a three-dimensional periodic flow. They also attempt a discussion of the transition scenario for Reynolds numbers higher than their second critical value of 170 as a period-doubling scenario. Their study reports that it cannot predict the low-frequency modulations obtained experimentally by Williamson (1988*b*), Eisenlohr & Eckelmann (1989) and in the theoretical study of König, Noack & Eckelmann (1993). They attributed this discrepancy to end-condition phenomena. However, it is known that parallel shedding conditions were ensured by the experimental investigations.

Barkley & Henderson (1996) determine the critical Reynolds number of the first discontinuity as 188.5, by using the linearized Floquet stability analysis, and describe the process as a subcritical bifurcation, due to the amplification of a secondary instability.

According to all these studies referring to the flow beyond the first bifurcation, it appears that a second important transition feature is the occurrence of the discontinuity drop, which is a consequence of a secondary instability. The linear approach, mostly adopted in these studies, is a precious tool to investigate rapidly the influence of infinitesimal disturbances on the critical Reynolds number. However, there are, to our knowledge, no numerical studies attempting to evaluate the critical Reynolds number of the appearance of the first discontinuity on the basis of a fully nonlinear methodology.

It is well known that in the vicinity of bifurcation points, fluctuations of finite-amplitude play a decisive role in determining the 'branch' that the system will follow and they influence the states following the bifurcations, Prigogine (1982), in the context of a dissipative system as is the case in the present flow system. For these reasons, it is essential to assess the evolution of the present fluctuating flow by adopting the complete nonlinear approach, which has the possibility of dealing with the impact of non-infinitesimal fluctuating motion.

Another part of our present study is to determine the critical Reynolds number for the appearance of the first discontinuity by using the complete system of the Navier–Stokes equations, despite the considerable efforts in CPU time that this approach requires.

Another important aspect of the present transition feature is the temporal and spatial evolution of the fundamental frequency in the near wake. Although there exist physical experiments dealing with these aspects for trapezoidal bodies, Goujon-Durand, Jenffer & Wesfreid (1994), and a few two-dimensional numerical simulations for triangular section configurations, Zielinska & Wesfreid (1995), there does not exist

to our knowledge a complete three-dimensional approach to these instability aspects and for the wake of a circular cylinder. This constitutes another main objective of our study.

According to this introductory discussion and on the basis of our recent work on the three-dimensional transition in the flow of a cylinder, the objectives of the present paper are summarized as follows.

(i) Provide a physical analysis of the main three-dimensional mechanisms related to the laminar–turbulent transition of the flow around a circular cylinder in the low Reynolds number range (100–300) and dissociate clearly the two-dimensional from the three dimensional phenomena.

(ii) Analyse and relate the appearance of the fundamental frequency modulations and of streamwise vorticity in the flow as Reynolds number increases.

(iii) Study the spatial variation of the mean flow properties and of the Reynolds stresses in the near wake, according to both the two- and three-dimensional approaches and relate them to the flow structure in the discontinuities region.

(iv) Study the time and space evolution of the fundamental mode in the near wake under the three-dimensional approach and establish the laws of variation of the maximum amplitude and of its location as a function of Reynolds number.

(v) Establish the critical Reynolds number of the first discontinuity on the basis of the complete three-dimensional Navier–Stokes system.

These objectives are achieved by the development of a numerical methodology (code ICARE), as described in §§ 2 and 3 for solving the full Navier–Stokes equations in three dimensions and by using the already existing two-dimensional version of the same algorithm. This provides a proper basis of comparison to dissociate the purely three-dimensional from the two-dimensional mechanisms, by performing a detailed three-dimensional and two-dimensional analysis. The physical analysis of the transition to turbulence phenomena in the present Reynolds number regime is carried out by means of a strong analogy with the experimental studies of Williamson in the same Reynolds number range. It is noticeable that the numerical approach offers the possibility to investigate separately the two- and three-dimensional mechanisms, which co-exist and interact unavoidably in the physical experiment.

According to the objectives, the present study is detailed in the following sections. The governing equations of an incompressible viscous fluid are presented in § 2. The outlines of the numerical procedure are presented in § 3. The boundary conditions and computational domain are discussed in § 4. In § 5 the validation tests and the choice of the numerical parameters are provided. The results are detailed in § 6, including eight subsections. In § 6.1, the onset of the vortex shedding is examined under the three-dimensional and two-dimensional approach, as Reynolds number increases. In § 6.2, by means of flow contour plots, the different classes of structures are investigated. Especially, the appearance of streamwise vortex loops, as Reynolds number increases is analysed and their impact on the fundamental frequency modulations is examined. The unsteady quasi-periodic dynamic properties of the flow are analysed in § 6.3. In § 6.4, a detailed quantification of the mean flow properties and of the Reynolds stresses is performed in the near region, in order to evaluate the birth of turbulence and its properties (increase and decay of the early beginnings of turbulent motion), by means of the present three-dimensional simulation. Especially, the mean profiles of the fluctuating and total kinetic energy are evaluated and related to the physical analysis of the discontinuity region of the Strouhal–Reynolds number relationship, presented in § 6.5. The properties of the present unsteady flow in the frequency domain are discussed in § 6.6 and a detailed study of the amplification of the Bénard–

Kármán instability in the near wake is provided in § 6.7, according to the two- and three-dimensional approaches.

Finally, in § 6.8, by using the three–dimensional system of Navier-Stokes equations, the critical Reynolds number for the appearance of the first discontinuity is evaluated.

2. Theoretical formulation

The governing equations for an incompressible viscous fluid flow past a circular cylinder are the continuity and the Navier-Stokes equations. The equations are written in a general curvilinear coordinates system normalized by the cylinder's diameter D and the uniform stream velocity U_∞:

$$u = \frac{\tilde{u}}{U_\infty}, \quad v = \frac{\tilde{v}}{U_\infty}, \quad w = \frac{\tilde{w}}{U_\infty}, \quad x = \frac{\tilde{x}}{D}, \quad y = \frac{\tilde{y}}{D}, \quad z = \frac{\tilde{z}}{D},$$

$$t = \frac{\tilde{t}}{T_0}, \quad P = \frac{\tilde{P}}{P_0},$$

where

$$T_0 = \frac{D}{U_\infty}, \quad P_0 = \tfrac{1}{2}\rho_0 U_\infty^2.$$

According to these dimensionless variables, the continuity equation and the time-dependent Navier–Stokes equations for an incompressible fluid in Cartesian coordinates are written in conservative form as

$$\nabla \cdot \boldsymbol{V} = 0, \tag{2.1}$$

$$\frac{\partial u}{\partial t} + \nabla \cdot (u\boldsymbol{V}) - \frac{1}{Re}\nabla \cdot (\nabla u) = -\frac{\partial P}{\partial x}, \tag{2.2}$$

$$\frac{\partial v}{\partial t} + \nabla \cdot (v\boldsymbol{V}) - \frac{1}{Re}\nabla \cdot (\nabla v) = -\frac{\partial P}{\partial y}, \tag{2.3}$$

$$\frac{\partial w}{\partial t} + \nabla \cdot (w\boldsymbol{V}) - \frac{1}{Re}\nabla \cdot (\nabla w) = -\frac{\partial P}{\partial z}, \tag{2.4}$$

where $\boldsymbol{V}$ is the velocity vector and Re the Reynolds number defined by

$$Re = \frac{U_\infty D \rho_0}{\mu}.$$

These governing equations are written in general curvilinear coordinates in the (x, y)-plane while the z-component (in the spanwise direction) is in Cartesian coordinates, as presented in § 3.2.1.

3. Numerical formulation

The numerical method is based on the three-dimensional full Navier–Stokes equations for an incompressible fluid. The pressure–velocity formulation is used as well as a predictor–corrector pressure scheme of the kind reported by Amsden & Harlow (1970), extended to the case of an implicit formulation by Braza (1981), Braza *et al*. (1986). The temporal discretization is done by adopting the Douglas fractional scheme in an Alternating Direction Implicit formulation. The method is second-order accurate in time and space. Centred differences are used for the space discretization. The staggered grids by Harlow & Welch (1965) are employed for the velocity

and pressure variables. The Navier–Stokes equations are transformed in respect to a non-orthogonal, general curvilinear coordinates system in the (x, y)-plane, while a Cartesian coordinate z is used for the spanwise direction. This ensures that the present solver can take into account any complex body configuration of constant z-section. An H-type grid is used because this kind of grid offers the possibility of introducing more physical boundary conditions on the external boundaries and it avoids branch-cut lines. While this grid requires an increased number of subdomains for the discretization it offers the advantage of studying body configurations in wind tunnels, or under a free surface. An original aspect of the present methodology is the extension of the Douglas alternating direction fractional step scheme, initially conceived for a pure diffusion equation, to the complete set of Navier–Stokes equations. The choice of this scheme, instead of the Peaceman & Rachford (1955) Alternating Direction Implicit one that was chosen in a previous two-dimensional study, Braza *et al*. (1986), is made due to the high stability properties offered by the Douglas (1962) scheme for the three-dimensional problem. Another useful element of the present numerical method is the extension in three-dimensional of non-reflecting-type boundary conditions, based on the work by Jin & Braza (1993) in two dimensions. These conditions are briefly described in § 4. These two characteristics of the present numerical algorithm may be useful for the numerical simulation of a wide category of three-dimensional flows around bodies, for example those of Jin & Braza (1994), Braza, Ha Minh & Chassaing (1994), Noguès (1995), for any (x, y, z) complex body configuration.

3.1. *Principles of the numerical method*

As the values of the velocity and pressure are known at the time step n, the momentum equations are solved at an $(n+1)$time step by using an approximate pressure field $P^* = P^n$. Therefore, these equations are solved for a corresponding velocity field $\boldsymbol{V}^*$. The vector form of the exact momentum equation at the time step $(n+1)$ is

$$\frac{\boldsymbol{V}^{n+1} - \boldsymbol{V}^n}{\Delta t} + \nabla \cdot (\boldsymbol{V}^n \boldsymbol{V}^{n+1}) = -\nabla P^{n+1} + \frac{1}{Re} \nabla \cdot (\nabla \boldsymbol{V}^{n+1}), \tag{3.1}$$

whereas the momentum equation for the approximate velocity field $\boldsymbol{V}^*$ is

$$\frac{\boldsymbol{V}^* - \boldsymbol{V}^n}{\Delta t} + \nabla \cdot (\boldsymbol{V}^n \boldsymbol{V}^*) = -\nabla P^n + \frac{1}{Re} \nabla \cdot (\nabla \boldsymbol{V}^*). \tag{3.2}$$

The velocity field $\boldsymbol{V}^*$ carries the exact vorticity but does not necessarily satisfy the mass conservation equation, as is the case for the true velocity $\boldsymbol{V}^{n+1}$ at the step time $(n+1)$. As both fields $\boldsymbol{V}^*$ and $\boldsymbol{V}^{n+1}$ carry the same vorticity, they can be related by an auxiliary potential function Φ, such as

$$\boldsymbol{V}^{n+1} - \boldsymbol{V}^* = -\nabla \Phi. \tag{3.3}$$

As $\nabla \cdot \boldsymbol{V}^{n+1} = 0$, the potential Φ can be calculated by taking the divergence of (3.3). A Poisson equation for Φ is then obtained:

$$\nabla \cdot \boldsymbol{V}^* = \Delta \Phi. \tag{3.4}$$

The true velocity field $\boldsymbol{V}^{n+1}$ can now be evaluated from (3.3). The corresponding pressure is deduced by combining the exact momentum equation (3.1), the approximate one (3.2) and equation (3.3). When the momentum equation is approximated

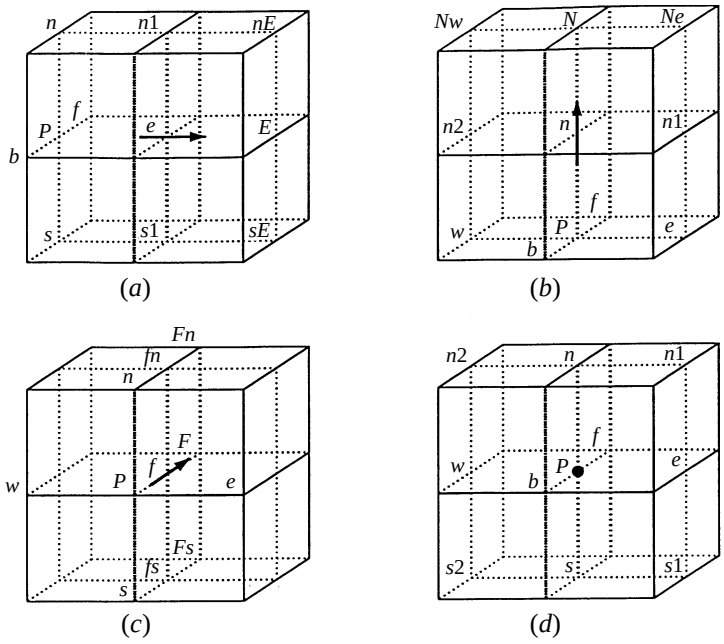

FIGURE 1. Integration cells: (*a*) *u*-component, (*b*) *v*-component, (*c*) *w*-component, (*d*) pressure.

by a fully explicit scheme, the pressure equation is reduced to

$$P^{n+1} = P^n + \frac{\Phi}{\Delta t}. \tag{3.5}$$

In this case of a semi-implicit scheme, the exact form for the pressure gradient is derived by subtracting equations (3.1) and (3.2) and by replacing $(\boldsymbol{V}^{n+} - \boldsymbol{V}^*)$ by $(-\nabla\Phi)$, according to equation (3.3).

The relation finally obtained is

$$\nabla P^{n+1} = \nabla\left(P^n + \frac{\Phi}{\Delta t}\right) + \nabla\cdot(\boldsymbol{V}^n\cdot\nabla\Phi) - \nu\nabla^2(\nabla\Phi). \tag{3.6}$$

Owing to the use of staggered grids for velocity and pressure, the calculation of pressure is only needed for interior mesh points. Whenever they are needed, the pressure values on boundaries are deduced directly from the momentum and continuity equations written at the boundary.

3.2. *Finite-volume approximation*

The governing equations are integrated over the corresponding control volumes. Each equation is obtained by integration on an elementary cell defined from the node associated with each unknown function (figure 1). The pressure correction is calculated on the nodes (•) whereas the velocity components are evaluated in the middle of two consecutive points used for the pressure calculation. In order to make the discretization easily, we have used the hypothesis that each function has a uniform distribution on the element on which it is considered. The principles of the numerical algorithm ICARE are based on Braza (1991 *a*, *b*).

3.2.1. *Momentum equations*

The momentum equations are integrated over the corresponding control volumes for u-, v- and w-components. The Gauss divergence theorem is used in order to transform the integrals of the divergence terms. The u-component equation is integrated as follows:
acceleration term

$$\iiint_{\Omega_u} \frac{\partial u}{\partial t}|J|\mathrm{d}\xi\mathrm{d}\eta\mathrm{d}z = |J_e|\left(\frac{\partial u}{\partial t}\right)_e \iiint_{\Omega_u} \mathrm{d}\xi\mathrm{d}\eta\mathrm{d}z = |J_e|\left(\frac{\partial u}{\partial t}\right)_e \Delta z \tag{3.7}$$

as $\Delta\eta = \Delta\xi = 1$;
advection terms

$$\left.\begin{aligned} \iint_{\Gamma_1} G_1 u\mathrm{d}\eta\mathrm{d}z &= (u_E G_{1E} - u_P G_{1P})\Delta z, \\ \iint_{\Gamma_2} G_2 u\mathrm{d}\xi\mathrm{d}z &= (u_{n1} G_{1n1} - u_{s1} G_{1s1})\Delta z, \\ \iint_{\Gamma_3} wuJ\mathrm{d}\xi\mathrm{d}\eta &= w_F u_F J_F - w_B u_B J_B = (w_F u_F - w_B u_B)J_P \end{aligned}\right\} \tag{3.8}$$

as there is a Cartesian mesh in the z-direction and so $J_B = J_F = J_P$;
viscous terms

$$\left.\begin{aligned} v\iint_{\Gamma_1} \frac{\alpha u_\xi - \beta u_\eta}{J}\mathrm{d}\eta\mathrm{d}z &= v\left(\frac{\alpha_E}{J_E}u_{\xi E} - \frac{\alpha_P}{J_P}u_{\xi P} - \frac{\beta_E}{J_E}u_{\eta E} + \frac{\beta_P}{J_P}u_{\eta P}\right)\Delta z, \\ v\iint_{\Gamma_2} \frac{\gamma u_\eta - \beta u_\xi}{J}\mathrm{d}\xi\mathrm{d}z &= v\left(\frac{\gamma_{n1}}{J_{n1}}u_{\eta n1} - \frac{\gamma_{s1}}{J_{s1}}u_{\eta s1} - \frac{\beta_{n1}}{J_{n1}}u_{\xi n1} + \frac{\beta_{s1}}{J_{s1}}u_{\xi s1}\right)\Delta z, \\ v\iint_{\Gamma_3} \frac{\partial u}{\partial z}J\mathrm{d}\xi\mathrm{d}\eta &= v\left[\left(\frac{\partial u}{\partial z}\right)_F - \left(\frac{\partial u}{\partial z}\right)_B\right]J_P; \end{aligned}\right\} \tag{3.9}$$

pressure terms

$$\left.\begin{aligned} \iint_{\Gamma_1} P y_\eta \mathrm{d}\eta\mathrm{d}z &= \left(y_{\eta E}P_E - y_{\eta P}P_P\right)\Delta z, \\ \iint_{\Gamma_2} P y_\xi \mathrm{d}\xi\mathrm{d}z &= \left(y_{\xi n1}P_{n1} - y_{\xi s1}P_{s1}\right)\Delta z. \end{aligned}\right\} \tag{3.10}$$

By introducing these expressions in the discretized u-momentum equation and by dividing by Δz, we can obtain the space discretisation for the u-component equation:

$$\begin{aligned} |J_e|\left(\frac{\partial u}{\partial t}\right)_e &+ u_E G_{1E} - u_P G_{1P} + u_{n1} G_{1n1} - u_{s1} G_{1s1} + (w_F u_F - w_B u_B)\frac{J_P}{\Delta z} \\ &= v\left(\frac{\alpha_E}{J_E}u_{\xi E} - \frac{\alpha_P}{J_P}u_{\xi P} - \frac{\beta_E}{J_E}u_{\eta E} + \frac{\beta_P}{J_P}u_{\eta P}\right) \\ &\quad + v\left(\frac{\gamma_{n1}}{J_{n1}}u_{\eta n1} - \frac{\gamma_{s1}}{J_{s1}}u_{\eta s1} - \frac{\beta_{n1}}{J_{n1}}u_{\xi n1} + \frac{\beta_{s1}}{J_{s1}}u_{\xi s1}\right) \\ &\quad + v\left[\left(\frac{\partial u}{\partial z}\right)_F - \left(\frac{\partial u}{\partial z}\right)_B\right]\frac{J_P}{\Delta z} \\ &\quad - \left(y_{\eta E}P_E - y_{\eta P}P_P\right) + \left(y_{\xi n1}P_{n1} - y_{\xi s1}P_{s1}\right). \end{aligned} \tag{3.11}$$

Similar transformations are made on the v-component, w-component and pressure-correction equations. Each equation is integrated over its particular elementary cell.

3.3. *Numerical scheme*

The Douglas (1962) alternating direction implicit (ADI) method is used for the time approximations of the equation. This method has the advantages of being both second-order temporal and space accurate and more stable in three-dimensional than other alternating direction schemes. Furthermore, the ADI method leads to tridiagonal systems, which can be efficiently solved by a Choleski algorithm. With this method, the u-momentum equation, integrated over the corresponding control volume, is written for three fractional steps as follows:

first step, which gives the u-field at the time step (i),

$$\begin{aligned}
-2\frac{u^{(i)}}{\Delta t}|J|\Delta z - \iint_{\Gamma_1} u^{(i)} G_1^n \mathrm{d}\eta\mathrm{d}z + \nu \iint_{\Gamma_1} \frac{\alpha}{J} u_\xi^{(i)} \mathrm{d}\eta\mathrm{d}z - \nu \iint_{\Gamma_2} \frac{\beta}{J} u_\xi^{(i)} \mathrm{d}\xi\mathrm{d}z \\
= -2\frac{u^n}{\Delta t}|J|\Delta z + \iint_{\Gamma_1} u^n G_1^n \mathrm{d}\eta\mathrm{d}z - \nu \iint_{\Gamma_1} \frac{\alpha}{J} u_\xi^n \mathrm{d}\eta\mathrm{d}z + 2\nu \iint_{\Gamma_1} \frac{\beta}{J} u_\eta^n \mathrm{d}\eta\mathrm{d}z \\
+ 2\iint_{\Gamma_2} G_2^n u^n \mathrm{d}\xi\mathrm{d}z - 2\nu \iint_{\Gamma_2} \frac{\gamma}{J} u_\eta^n \mathrm{d}\xi\mathrm{d}z + 2\nu \iint_{\Gamma_2} \frac{\beta}{J} u_\xi^n \mathrm{d}\xi\mathrm{d}z \\
+ 2\iint_{\Gamma_3} w^n u^n J \mathrm{d}\xi\mathrm{d}\eta - 2\nu \iint_{\Gamma_3} \frac{\partial u^n}{\partial z} \mathrm{d}\xi\mathrm{d}\eta - 2\iiint_{\Omega} S_u |J| \mathrm{d}\xi\mathrm{d}\eta\mathrm{d}z ; \qquad (3.12)
\end{aligned}$$

second step, which gives the u-field at the time step (ii),

$$\begin{aligned}
-2\frac{u^{(ii)}}{\Delta t}|J|\Delta z - \nu \iint_{\Gamma_2} u^{(ii)} G_2^n \mathrm{d}\xi\mathrm{d}z - \nu \iint_{\Gamma_1} \frac{\beta}{J} u^{(ii)} \mathrm{d}\eta\mathrm{d}z + \nu \iint_{\Gamma_2} \frac{\gamma}{J} u_\eta^{(ii)} \mathrm{d}\xi\mathrm{d}z \\
= -2\frac{u^n}{\Delta t}|J|\Delta z - \nu \iint_{\Gamma_1} \frac{\beta}{J} u^n \mathrm{d}\eta\mathrm{d}z - \nu \iint_{\Gamma_2} u^n G_2^n \mathrm{d}\xi\mathrm{d}z + \nu \iint_{\Gamma_2} \frac{\gamma}{J} u_\eta^n \mathrm{d}\xi\mathrm{d}z ; \qquad (3.13)
\end{aligned}$$

third step, which gives the u-field at the time step $(n+1)$,

$$\begin{aligned}
2\frac{u^{n+1}}{\Delta t}|J|\Delta z + \iint_{\Gamma_3} u^{n+1} w^n J \mathrm{d}\xi\mathrm{d}\eta - \nu \iint_{\Gamma_3} \frac{\partial u^{n+1}}{\partial z} J \mathrm{d}\xi\mathrm{d}\eta \\
= 2\frac{u^n}{\Delta t}|J|\Delta z + \iint_{\Gamma_3} u^n w^n J \mathrm{d}\xi\mathrm{d}\eta - \nu \iint_{\Gamma_3} \frac{\partial u^n}{\partial z} J \mathrm{d}\xi\mathrm{d}\eta . \qquad (3.14)
\end{aligned}$$

These equations are written for all the nodes of the unknown u.

4. Boundary conditions

In the physical domain the flow is not confined. Nevertheless, fictitious external boundaries are necessary far from the cylinder. The solution of the above system will be obtained on a three-dimensional domain defined on figure 2. The choice of the boundary conditions is an important problem in order to not confine the calculation domain of the present exterior flow. In non-dimensional units, the cylinder diameter is $D = 2$. In the spanwise z-direction, the cylinder is theoretically supposed to be infinite. However, the computational domain has a finite spanwise value, at the edges

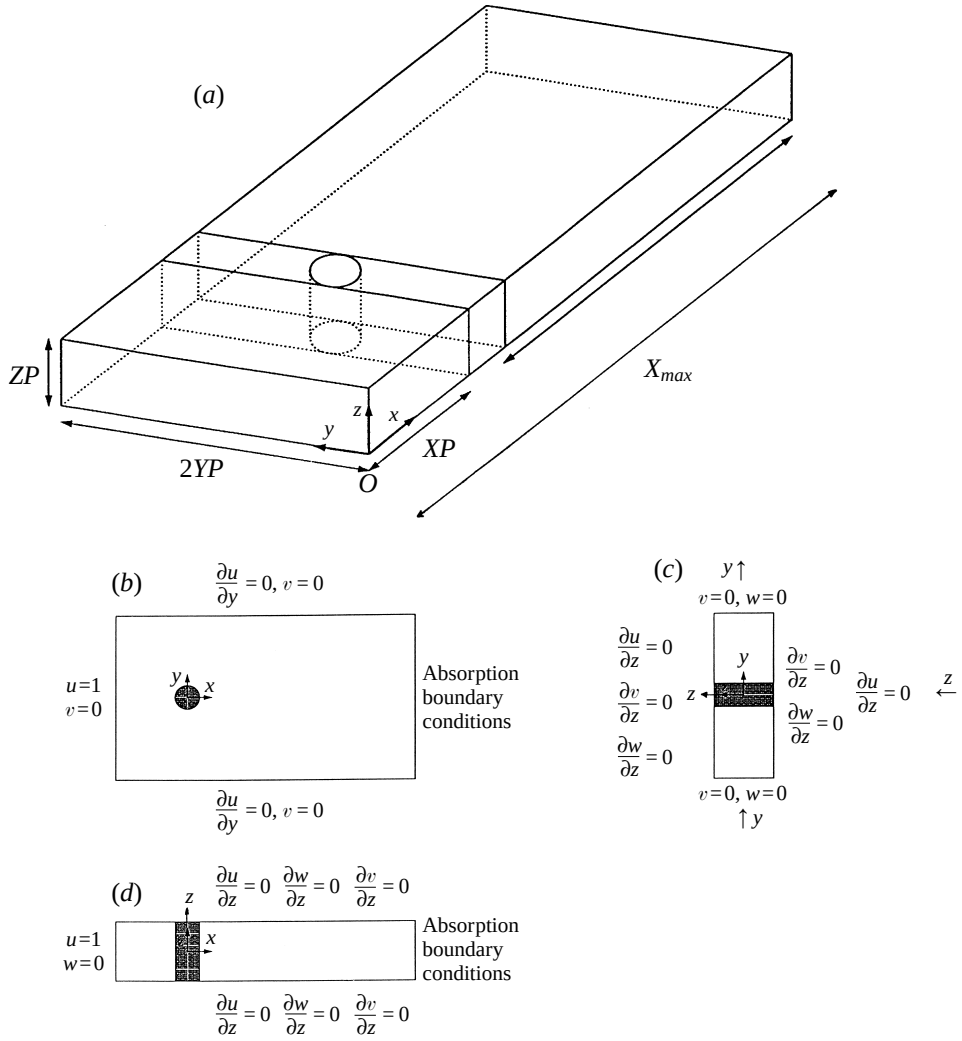

FIGURE 2. (*a*) Computational domain. (*b–d*) Boundary conditions for velocity components: (*b*) z =const., (*c*) x =const., (*d*) j =const.

of which the boundary conditions have to represent as far as possible, the infinite flow situation, in order to not confine artificially the simulated flow.

4.1. *Velocity*

On the cylinder's surface, the boundary conditions are those of impermeability and non-slip: $\boldsymbol{V} = 0$.

On the upstream section, at the distance X_1 from the cylinder, a uniform velocity profile $u = 1$ is imposed.

Absorption boundary conditions, derived from non-reflecting properties of the wave equation, are used at the far-field outlet boundary of the computational domain. These kind of conditions, developed in detail by Jin & Braza (1993) for two-dimensional non-confined flows with coherent structures and extended in the present study to three dimensions, allow the vortices to leave the domain naturally and minimize reflective

or feed-back effects. These conditions are as follows:

$$\frac{\partial F}{\partial t} + u\frac{\partial F}{\partial x} - \nu\left(\frac{\partial^2 F}{\partial y^2} + \frac{\partial^2 F}{\partial z^2}\right) = 0, \tag{4.1}$$

where F represents the velocity components u, v and w.

In the spanwise direction, in order to simulate an infinite cylinder, a Neumann-type boundary condition has been adopted for the velocity field:

$$\frac{\partial u}{\partial z} = 0, \quad \frac{\partial v}{\partial z} = 0, \quad \frac{\partial w}{\partial z} = 0. \tag{4.2}$$

This condition expresses the fact that the velocity component variation is negligible within the last dz grid spacing, at the ends of the domain. As the dz value is usually chosen small enough, in respect to the accuracy and convergence of the numerical scheme requirements, the present boundary conditions are suitable even for moderate spanwise dimensions. Within a small dz distance, the experimental profiles of the velocity components are reasonably expected to be very close to each other whereas the same experimental profiles do not in general show 'periodic' properties for sections measured at the two ends of the span, or more generally, for any two sections along the span. For this reason, the authors believe that the use of 'periodic' boundary conditions for the present category of flows is not in accordance with the physical reality, although the use of such conditions allows a numerically obtained spanwise visualization to be 'repeated' and hence display a larger span, as is often used in three-dimensional visualizations of the present category of flows.

The present study has been possible by using a moderate value of the spanwise length, as discussed in § 5.

Finally, in the y-direction, in order to not confine the flow, a Neumann-type boundary condition has been adopted for the u-component and a Dirichlet-type boundary condition has been taken for v-component and w-component:

$$\frac{\partial u}{\partial y} = 0, \quad v = 0, \quad w = 0. \tag{4.3}$$

These conditions are consistent with the domain size and do not confine the flow, as is shown in the results. They are based on the hypothesis that these boundaries are streamlines.

4.2. *Pressure correction* Φ

The pressure correction boundary conditions are deduced from velocity boundary conditions. Indeed, as it has been assumed that the boundary conditions of the fictious velocity $\boldsymbol{V}^*$ are the same as of the real velocity $\boldsymbol{V}$, the pressure correction boundary conditions are deduced from equation (3.3), written in respect to each boundary condition. In this way, at the inlet of the domain we obtain

$$\frac{\partial \Phi}{\partial x} = 0. \tag{4.4}$$

The outlet conditions downstream are given by combining equations (4.1) and (3.3):

$$\frac{u^n \Delta t}{2}\left(\frac{\partial^2 \Phi}{\partial x^2}\right) + \left(\frac{\partial \Phi}{\partial x}\right) = 0. \tag{4.5}$$

In the spanwise direction, we obtain:

$$\frac{\partial^2 \Phi}{\partial z^2} = 0. \tag{4.6}$$

Finally, in the y-direction, by using (4.3) and (3.3), we have

$$\frac{\partial \Phi}{\partial y} = 0. \tag{4.7}$$

The initial conditions are taken as $u = 1$, $v = 0$, $w = 0$, $P = 0.5$, for the fields at the inner points of the domain (i.e. except at the frontiers).

5. Simulation tests – influence of the numerical parameters

Before undertaking the three-dimensional numerical simulations, extensive tests were carried out in order to analyse the influence of the computational domain, of the grid spacing and of time step. The H-type grid in general curvilinear coordinates has been generated by the numerical algorithm MERCURE provided by Braza (1991*a*, *b*), using a system of elliptic equations according to the method of Thomson, Thames & Mastin (1974). An example of this grid in the median section of the domain is given on figures 3(*a*) and 3(*b*). The same grid is repeated in all dz sections. The domain of figure 3 is used to compute the two-dimensional flow at Reynolds number 100. By performing a computation for a long physical time, we obtain the vortex shedding regime, figure 4(*a*). In the vicinity of $t = 80$, the temporal evolution of the lift coefficient reaches a plateau and the symmetric vortex pattern reaches an established state before being destabilized towards the vortex shedding regime.

In order to choose an optimum-time step value, computations have been performed with $\Delta t = 0.01$ and $\Delta t = 0.02$. These time-step values have been chosen because they are of the order of magnitude of successful values examined in previous works (Jin & Braza 1993; Braza *et al.* 1986, among others). Figure 4(*c*) shows the time-dependent evolution of the recirculating length according to these time-step values. The recirculating length is evaluated during the symmetric vortex pattern. The recirculating lengths obtained are practically the same for both time-step values. Hence, the independence of the solution on the time step is ensured.

The study of the influence of the computational domain has been done first on the two-dimensional code. The size of the two-dimensional computational domain can be described by three specific dimensions: the length XP, which specifies the location of the inflow boundary, X_{max} which represents the total horizontal length of the computational domain, and YP which is the half-width of the domain (vertical direction). We examine the dependence of the results on the computational domain size, in order to use an optimum domain for the whole study. The influence of the domain on the main flow characteristics (Strouhal number and drag coefficient) are summarized on table 1. The ensemble of the YP values chosen (see figure 2), is proven sufficient in order to not confine the flow in respect to blockage effects. Indeed, for two close values of XP (domains D_4 and D_5), the values of YP (11.2 and 12.0) provide global parameters in very good agreement with the physical experiment. Indeed, the experimental Strouhal value is 0.164 (see also figure 11) and the experimental drag coefficient value is 1.26 (see figure 10). The corresponding numerical values for the domains D_3 and D_4 are 0.164, 1.26 and 1.25 respectively. It is noticeable that these computations do not produce a higher value of the Strouhal number, which would occur if there were blockage effect.

(*a*)

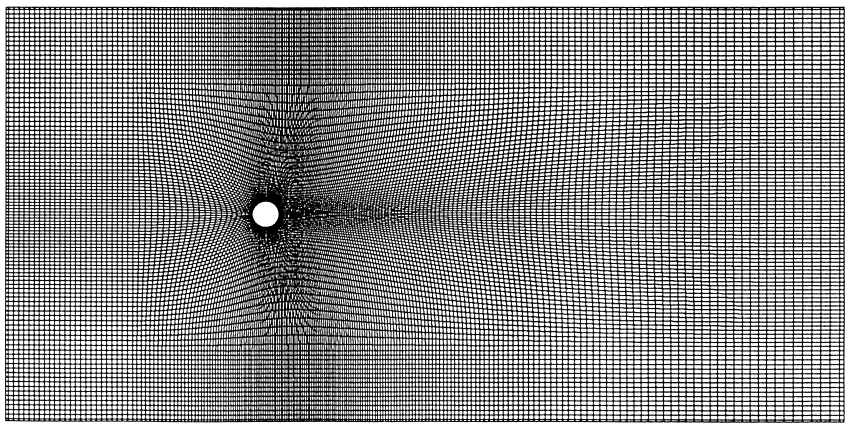

(*b*)

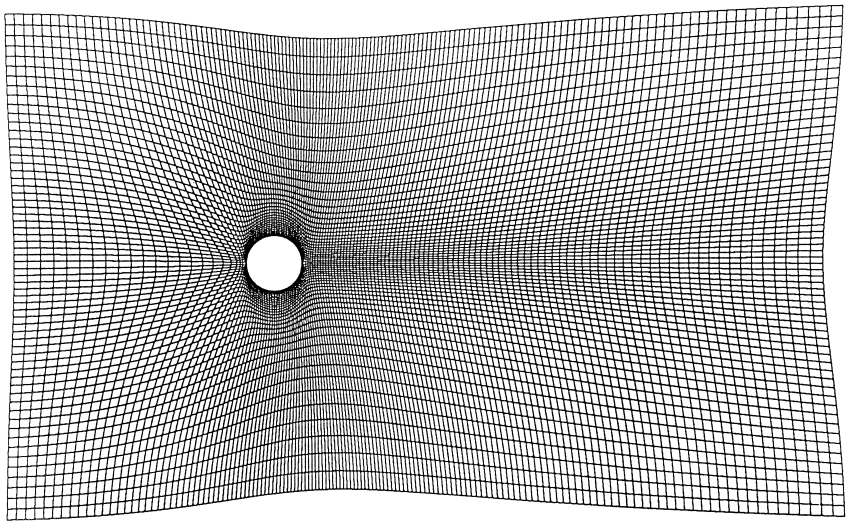

FIGURE 3. (*a*) Configuration of the H-grid around the cylinder in the (x, y)-plane. Dimensions of the grid: $213 \times 102 \times 32$. (*b*) Magnification of the grid around the cylinder.

Domain	$\Delta x_{cyl.}$	$NX \times NY$	XP	YP	St	C_D
D_1	$\pi/41$	235x124	7.81	13.31	0.176	1.32
D_2	$\pi/41$	235x134	7.60	19.42	0.175	1.33
D_3	$\pi/41$	270x124	14.98	17.33	0.171	1.26
D_4	$\pi/41$	260x90	18.56	11.22	0.164	1.26
D_5	$\pi/33$	213x86	18.34	12.00	0.164	1.25
D_6	$\pi/33$	213x102	19.69	16.46	0.164	1.25

TABLE 1. Characteristics of the different computational domains. NX, NY: number of points in the x- and y-direction respectively; XP: upstream length; X_{max}: total horizontal length; $2YP$: vertical width of the domain; for symbols see also figure 2; St: Strouhal number, C_D: drag coefficient

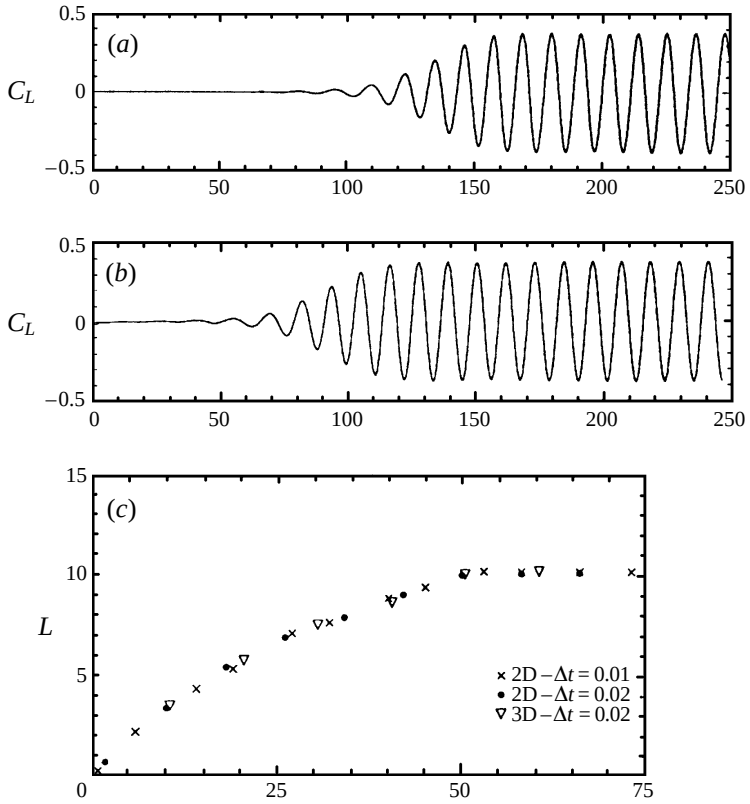

FIGURE 4. Time-dependent evolution of lift coefficient without perturbation, (*a*) two-dimensional case and (*b*) three-dimensional case, $Re = 300$. (*c*) Recirculation length, $Re = 100$.

The variation of the length YP does not seem to have much influence on the Strouhal value. The comparison of D_1 and D_2 shows a small decrease of St when YP increases. This slight difference would not justify a further increase of YP, in order to save CPU time. On the other hand, the increase of the upstream distance XP seems to have a greater influence on the Strouhal number value. In fact, the inflow length XP must be large enough to ensure a good agreement with the experimental value.

The difference between D_1 and D_3 is essentially due to the junction of a Cartesian mesh region near the borders in the x-direction, while the difference between D_1 and D_2 is due to the same effect in the y-direction. The results corresponding to the different domain sizes are critically assessed according to a 'reference' Strouhal number value given by Williamson's experimental studies, $St = 0.164$, which are found to be within the range of 1% of accuracy.

The value of the downstream distance $(X_{max} - XP)$ seems to influence the global parameters much more. In fact, values less than about 34 produce an increase of the Strouhal number and of the drag coefficient. Hence, it appears that the domains D_4 to D_6 are acceptable for the present simulation method.

In order to have a larger domain without increasing the number of nodes, we have generated D_5 which has approximately the same size as D_4 with larger cells near the wall. This new mesh generates the same Strouhal number as D_4. Then, to ensure that there are no boundary condition problems, we have added a Cartesian mesh to the borders of both directions, domain D_6. This is the finally chosen domain for the whole

	Two dimensions	Three dimensions
Recirculation length	10.2	10.2
Separation angle	110.2	110.8
Drag coefficient	1.2	1.15

TABLE 2. Mean dynamic characteristics of the symmetric flow, $Re = 100$.

study. Through the three last tests we can also see the effect of the grid independence on the numerical results. As the two grid refinements provide essentially the same results, we retain the coarser grid for the final computations, for the sake of CPU time economy in respect to the three-dimensional computations. As shown on table 3, § 6, this grid refinement provides a very good agreement with the experimental values for all the Reynolds number range (100–300) considered in the present study. Hence, the present grid is retained for the whole study.

Concerning the three-dimensional domain, it is noticeable that the present simulation needs considerable CPU time. An initial test with a small spanwise size (0.525 diameters) was carried out for $Re = 100$ and provided practically the same results concerning the vortex shedding phenomenon as the results for a spanwise length of 2.25 diameters, figure 5 (*b*). For this reason we have adopted the moderate spanwise dimension of 2.25 diameters and the Δz grid spacing of 0.15. The finally chosen computational domain is therefore the domain D_6 along all the span. The typical CPU times per time step is 25 s on the Cray C98. Approximately 40 hours are needed for a complete computation of one Reynolds number value. The whole study has been carried out using the spanwise length $s = 2.25D$.

During the symmetric phase of the flow, up to time value 80, the three-dimensional computations provide the recirculation length, separation angle and drag coefficient shown on table 2. These results are compared with other experimental and numerical studies in figure 5 (*a–c*). The good agreement obtained confirms the validity of the present methodology. The quasi-periodic phase of the flow provide a Strouhal number and drag coefficient (tables 2, 3 and figure 10), which also compare very well with the experimental and numerical results.

In addition, a higher spanwise dimension case was also carried out, $s = 3.72D$. This also provides a Strouhal number value in very good agreement with the experiments and allows a more detailed insight for the development of the three-dimensional motion, as it is discussed in § 6.2. These validation tests for the three-dimensional flow, in conjunction with the first part of the results presented in the next section, ensure the accurate prediction of the three-dimensional flow around the cylinder.

6. Results

During the initialization of the flow, two symmetrical vortices appear behind the cylinder on each side of the wake. These structures are progressively elongated downstream, first rapidly and afterwards more slowly, to reach finally a steady state. This phenomenon, described in many studies, Dennis & Chang (1970), can be seen in the time evolution of the reattachment length (figure 5 *c*). The present computations provide a length of 10.2 for $Re = 100$ in both two- and three-dimensional cases. In the two-dimensional case, the steady pattern is reached for $t = 60$ and lasts to $t = 90$. In the three-dimensional case, the duration of this pattern is shorter (figure 5 *a*, *b*). During

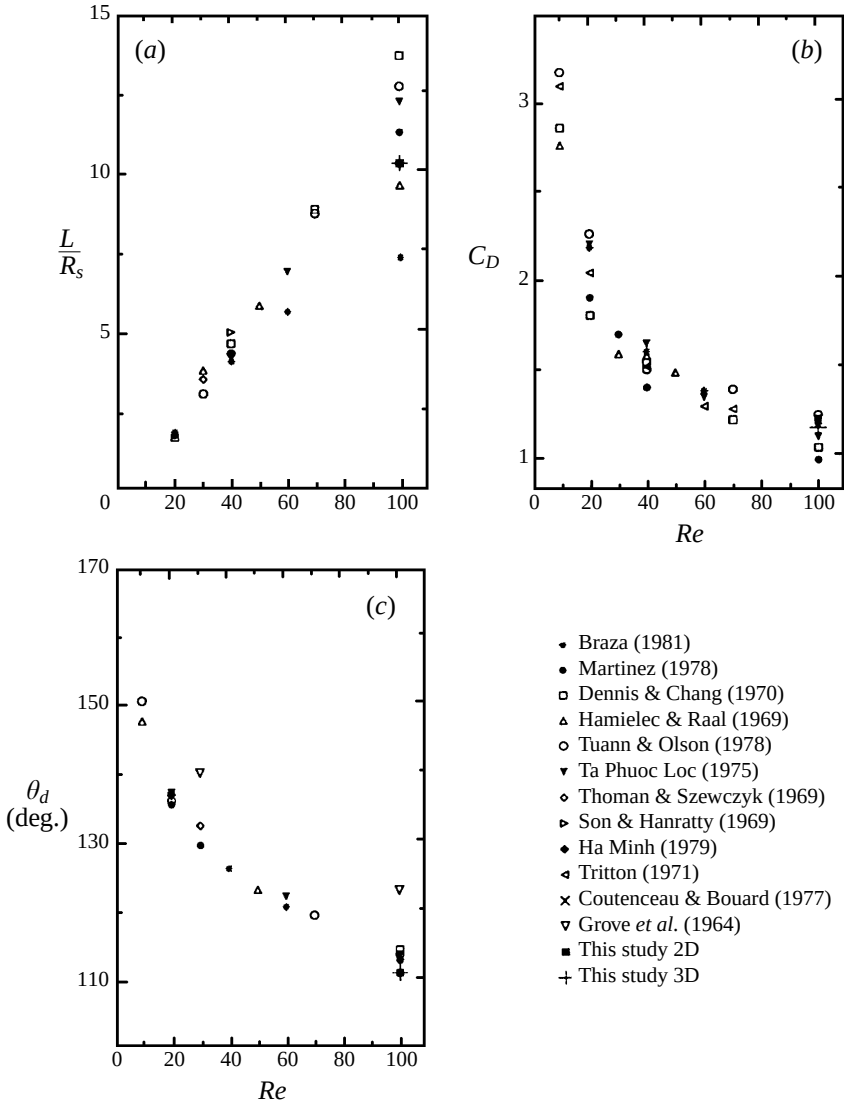

FIGURE 5. Global parameters of the symmetric flow: (*a*) recirculation length, (*b*) drag coefficient, (*c*) separation angle, $Re = 100$.

the symmetric phase of the flow, the mean recirculation lengths, drag coefficient and separation angle are evaluated using the three-dimensional approach and are found in very good agreement with other numerical and experimental studies (figure 5*a–c*). The recirculation region is destabilized faster in the three-dimensional case under the effect of the numerical and round-off errors distribution, which act as perturbations and trigger the alternating vortex pattern.

It is noticeable that the von Kármán instability is generated naturally by the present simulation without the need of imposing external perturbations, after a long physical time during which the flow remains steady. The destabilization of the flow towards a symmetry-breaking state is obtained under the action of small truncation errors and also of computer's round-off errors. The truncation errors especially are not

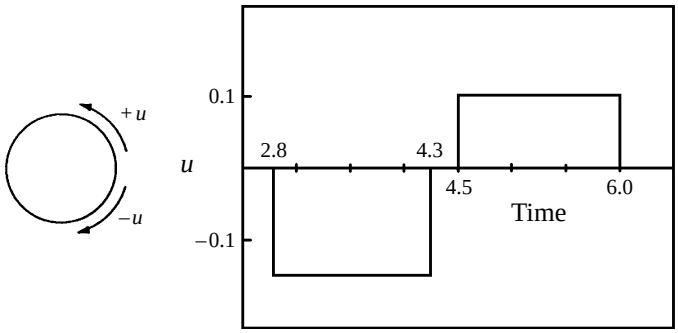

FIGURE 6. The numerical perturbation: variation of the wall tangential velocity as a function of time.

symmetrically distributed, because the numerical scheme operators are not symmetric. Indeed, the ADI method for instance performs a sweep for the solution of the first direction step (x-direction) from the left to the right and in this way there is a non-symmetric distribution of the truncation errors. Furthermore, during the third ADI step, the sweep is performed from $z = Z_{min}$ to $z = Z_{max}$ and again the distribution of small truncation errors is not symmetric. These non-symmetric small perturbations act to trigger the preferred instability mode by the flow system, which is the von Kármán mode.

Under these effects, wake oscillations appear and destabilization of the flow occurs after $t = 60$ approximately, leading to the alternating vortex pattern. The established state of this pattern occurs after $t = 170$ (i.e. after 8500 time steps) in the two-dimensional case and after $t = 130$ in the three-dimensional case.

As is discussed in § 6.6 (spectral analysis), the same fundamental frequency value is obtained at any space point investigated. The present system behaves as a global oscillator and the nature of the dominant instability is an absolute one, as expected.

Since the purpose of this study is to analyse three-dimensional transition features for the flow around the cylinder, it is important to reduce the transient phase and to reach the established flow as fast as possible. The ideal situation would be to introduce in the numerical procedure identical perturbations to those that occur unavoidably in any described experiment, precisely described and quantified. As this task is very difficult to achieve, and for all the mentioned reasons related to the need to shorten the transient phase, well-studied technique is adopted in this study, as used in the work by Braza *et al*. (1986) for the same numerical method in two-dimensions. This technique consists of rotating the cylinder for a short time, as shown on figure 6. In the work by Braza *et al*., a detailed discussion was provided on this technique, originally employed by Martinez (1978) in a vorticity–stream-function numerical scheme. In these studies, it was demonstrated that two different perturbations lead to the same physically correct established state, with a very good agreement of the dynamic parameters to the physical experiment. This technique of imposing a very short-time perturbation at the very beginning of the flow is not related to the often used techniques of imposing small-scale perturbations permanently to trigger preferred modes on the established flow. In the present study, the perturbation used acts only to shorten the initial transient phase for the sake of economy in the CPU time. It is demonstrated that the established phase is the same without imposing this perturbation. The achievement of shortening the transient phase, according to the present two- and three-dimensional simulation is shown on figure 7 for the drag

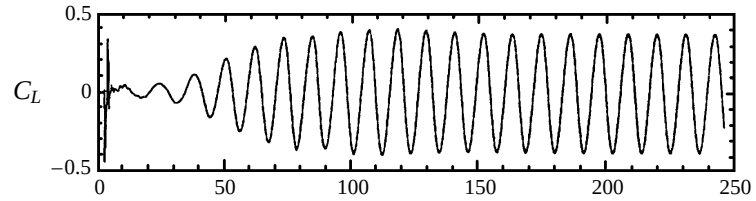

FIGURE 7. Lift coefficient of the three-dimensional flow with initial phase short-time perturbation, $Re = 100$.

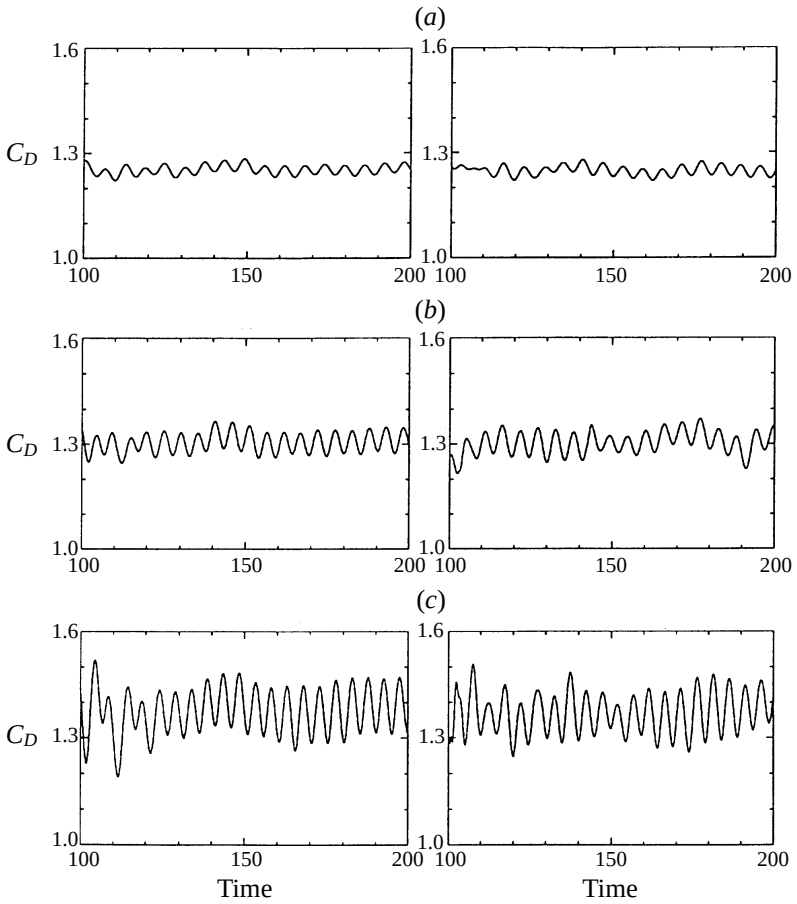

FIGURE 8. Time-dependent evolution of drag coefficient: two-dimensional case (left), three-dimensional case (right). (*a*) $Re = 100$, (*b*) $Re = 200$, (*c*) $Re = 300$.

and lift time-dependent coefficients. Comparing to figures 4(*a*) and 4(*b*), where the same parameters are shown for the computations without perturbation, it can be seen that the transient phase is considerably shortened. Furthermore, the long transient phase in the case without perturbation, as well as the regularity of the frequency and amplitude fluctuations of the lift coefficient, in very good agreement of the results with the experiment, show that the present numerical method provides a non-noisy correct physical behaviour.

Figures 8 and 9 show the time-dependent evolution of the drag and lift coeffi-

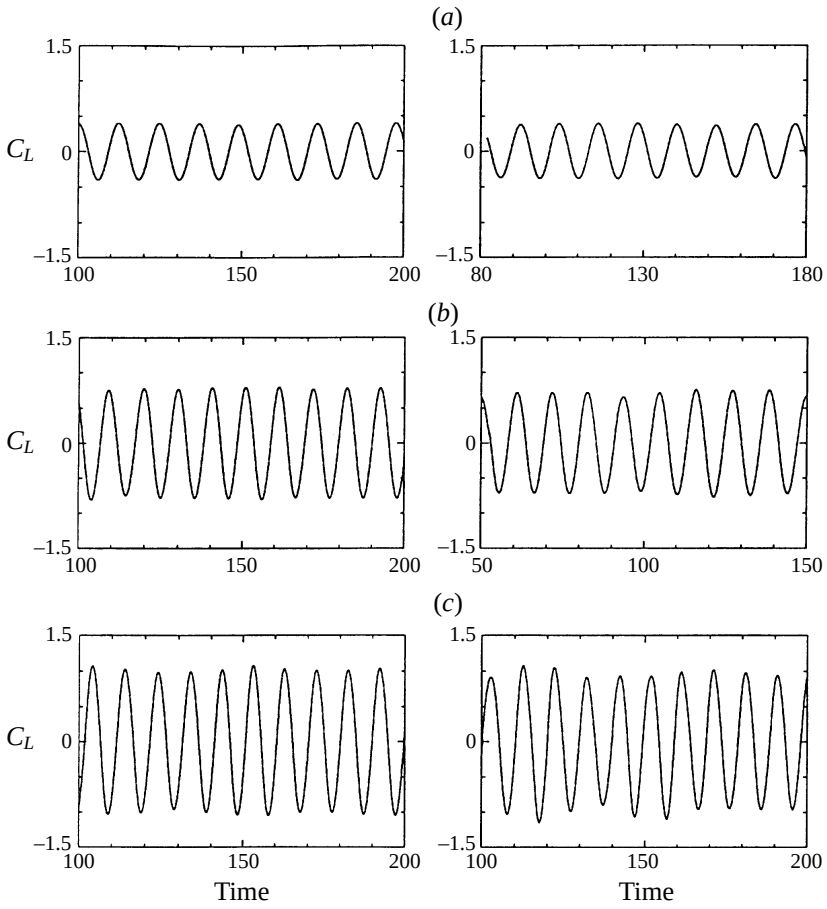

FIGURE 9. Time-dependent evolution of lift coefficient: two-dimensional case (left), three-dimensional case (right). (*a*) $Re = 100$, (*b*) $Re = 200$, (*c*) $Re = 300$.

cients respectively, as a function of Reynolds number, for the established phase. The frequency of the drag coefficient oscillations is twice as fast as the oscillations of the lift coefficient. This result, as expected, is due to the contribution of the upper and lower alternating vortices to the drag. The amplitudes of the oscillations for the drag and lift coefficients increase as Reynolds number increases. However, the rate of increase is reduced in the three-dimensional case. The mean drag coefficient also decreases, comparing the two-dimensional and three-dimensional case for the same Reynolds number. It is well known that a general tendency of the two-dimensional computations is to overpredict the drag coefficient, as Reynolds number increases. This inconvenience is resolved in the present case of three-dimensional computations. While for Reynolds number 100, there are no considerable variations between the two- and the three-dimensional computations, this is not the case for Reynolds numbers 200 and 300. These aspects are discussed in the next section.

On table 3, the mean global parameters of the established flow are provided for the two- and three-dimensional simulations. A very good agreement is obtained with the physical experiment (figure 10).

	Re	St	θ_d	$\bar{C}_D$	$C_{L\ rms}$
2-D case	100	0.165	113.5	1.253	0.078
	150	0.181	110.7	1.268	0.169
	200	0.198	109.5	1.321	0.301
	250	0.204	108.2	1.359	0.418
	300	0.209	109.4	1.405	0.526
3-D case	100	0.164	113.3	1.240	0.071
	190	0.179	109.7	1.298	0.151
	200	0.181	107.9	1.306	0.254
	220	0.184	105.4	1.313	0.311
	250	0.186	105.7	1.343	0.400
	300	0.206	106.5	1.366	0.477

TABLE 3. Global parameters for the quasi-periodic flow.

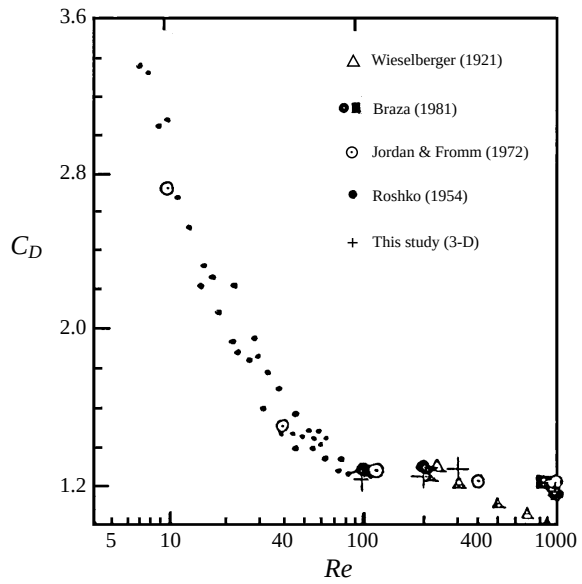

FIGURE 10. Mean drag coefficient versus Reynolds number.

6.1. *Effect of three-dimensionality on global parameters*

Table 3 shows the Strouhal number, separation angle, mean drag coefficients and the r.m.s. value of the lift coefficient for both two- and three-dimensional cases. In the two-dimensional simulation the mean drag and r.m.s. lift coefficients are higher than in the three-dimensional case. This behaviour, already observed at $Re = 100$, becomes more pronounced as Reynolds number increases. This tendency is confirmed by other numerical and experimental studies. Beaudan & Moin (1994) have compared two- and three-dimensional simulations at $Re = 3900$ and have obtained a decrease of r.m.s. lift and of the mean drag coefficient in the three-dimensional case. Experimental works reported at the Göttingen Symposium 'Bluff Body Wakes, Dynamics and Instabilities' (Eckelmann *et al.* 1992) mentioned the same behaviour. Szepessy & Bearman (1992) show that the experimental $C_{L\ \mathrm{r.m.s}}$ are lower than the corresponding two-dimensional numerical ones as Reynolds number increases. The separation angle is practically the

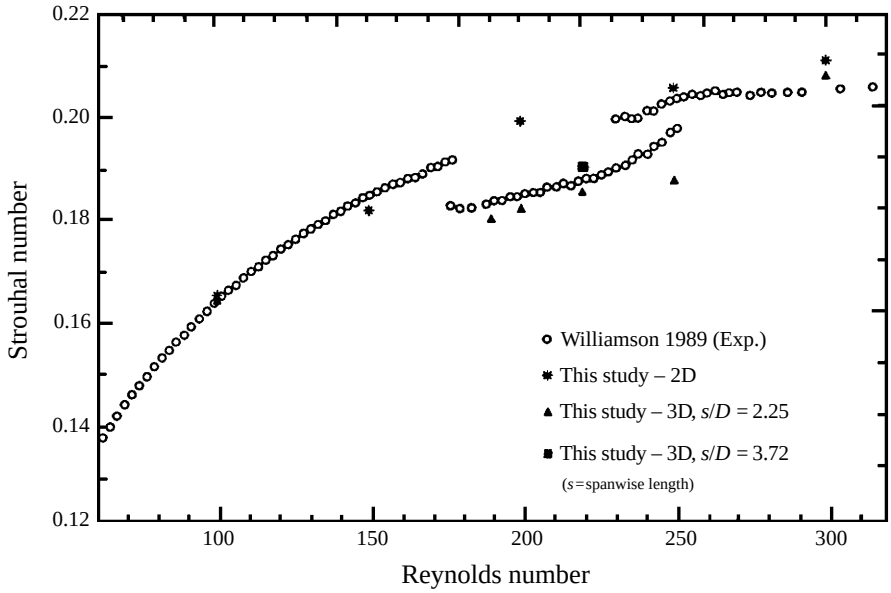

FIGURE 11. Strouhal number versus Reynolds number.

same in two- and three-dimensional cases for $Re = 100$ because the three-dimensional effects are not very important at this Reynolds number value. As Reynolds number increases, the separation angle is smaller in the three- than in the two-dimensional case. Because the three-dimensional smaller-scale effects become more prominent and destabilize the flow. An experimental study by Trichet (1975) provides a mean separation angle equal to 104° at $Re = 200$.

There is a striking difference in the Strouhal number between two- and three-dimensional cases. In fact, for each Reynolds number, the three-dimensional Strouhal number is lower than the two-dimensional one. Especially around $Re = 200$, its variation forms a deficit region which constitutes a discontinuity region in the overall St, Re relation (figure 11). This difference in the Strouhal number values (almost 10% for $Re = 200$) is in good agreement with the physical experiments of Williamson (1988 *a*, *b*) who has shown the existence of two discontinuities in the St, Re relation in the Reynolds number range from 180 to 260. Hence, the present three-dimensional simulations carried out in the Reynolds number range 100–250 describe this discontinuity region well. For $Re = 100$ and $Re = 300$ (outside the discontinuity range), the difference between two- and three-dimensional cases is weak (1% and 1.5% for $Re = 100$ and $Re = 300$ respectively). These values are very close to the experimental results suggested by Williamson (1988), within the accuracy of 1%. They extend the experimental curve of the parallel shedding, obeying the relation

$$St = \frac{A}{Re} + B + CRe$$

where $A = -3.3265$, $B = 0.1816$ and $C = 1.6\ 10^{-4}$ (Williamson 1988*a*).

This good agreement with the physical experiments confirms the correct behaviour of the numerical code developed with suitable numerical parameters. The effect of the existence of a frequency modulation region is a confirmed characteristic of the present three-dimensional simulations for a set of Reynolds number values, as can be

seen in figure 11, despite the considerable amount of CPU time that all this set has needed.

Beyond Reynolds number 220, the existence of a second frequency step is found towards the upper plateau of the St, Re curve, that the present three-dimensional computations reach at $Re = 300$. These simulations also show a decrease of the fundamental frequency at $Re = 250$, which tends to follow the experimentally obtained branch of the curve with dislocations (figure 34 *a*), established by Prasad & Williamson (1997). At this stage, the present numerical simulation is not able to show a vortex dislocation pattern, using the rather small spanwise length of $2.25D$. However, a truncated effect of a tendency to form a vortex dislocation may exist in the flow field, as nothing has been imposed to trigger or to inhibit this pattern. The prediction of vortex dislocations is a main objective of our studies in progress, by using higher spanwise lengths.

Another important point to note is that the difference between the two- and the three-dimensional simulation shows the strictly three-dimensional character of the two discontinuities and of their intermediate region. Indeed, by performing two-dimensional computations, the St, Re relation is continuous and forms an extension of the lower Reynolds number range curve. It also forms a higher plateau than the three-dimensional case and the experimental data, beyond $Re = 250$. From the shape of the computationally obtained St, Re curve, it is noticeable that the present study is able to predict spontaneously the formation of a discontinuity region, delimited by two steps. The majority of the recent three-dimensional simulations do not predict the appearance of these two discontinuities. Karniadakis & Triantafyllou (1992) have used a spectral-element method for Reynolds numbers from 100 to 500 and they have not mentioned any discontinuity region. Their Strouhal number values are higher than experimental values. In 1995, Zhang *et al*. also performed a three-dimensional simulation using an explicit Navier–Stokes solver, for Reynolds numbers in the range 180–300. In their study the Strouhal number values obtained diminished only in the vicinity of $Re = 180$ and they do not report formation of a discontinuity area with a second step. Although that study reports development of streamwise vortex structures, the visualizations of that flow in the (x, y) median plane do not show the alternating eddies pattern which is a fundamental feature of this transition process as is clearly shown in numerous experimental visualizations, reported among others, by Van Dyke (1982). Their visualizations show only one row of non-alternating eddies beyond a very short distance in the near wake. Other numerical simulations on this topic also do not show clearly the persistance of the alternating vortex pattern over a significant distance, although they predict a frequency drop related to the first discontinuity (Thompson *et al*. 1994; Mittal & Balachander 1995; Henderson & Barkley 1996). None of these studies predicts the whole shape of the discontinuity region in the Reynolds number range 180–300. The present paper makes clear the appearance of the two discontinuities with a good agreement with the physical experiment by using a moderate spanwise length (2.25 diameters).

6.2. *Contour plots of flow quantities*

The instantaneous field quantities are presented on figures 12–20. In order to compare properly the instantaneous contour plots, the same extrema values have been fixed for one dynamic quantity for all the related figures. In this way, the same colour maps have been obtained. The different section planes are shown on figure 12.

Figure 13 shows the isopressure contours in the median z-plane, for $Re = 190$. These isobars indicate the maximum pressure values in the vicinity of the front

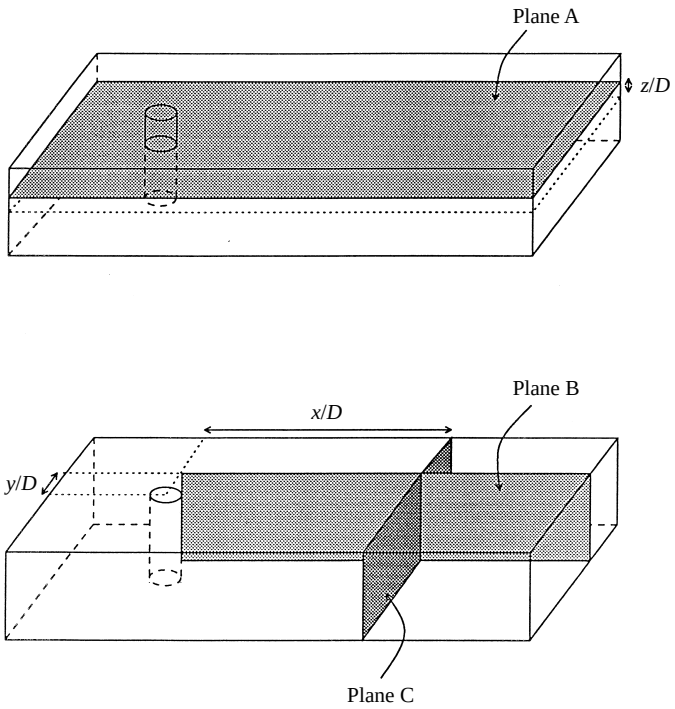

FIGURE 12. Configuration of the visualization planes.

stagnation point (green region). They also illustrate clearly the alternating vortex street. The kernels of the alternating vortices correspond to minimum values of the pressure coefficient.

Figure 14 presents the vorticity component ω_z. The whole domain is shown. It can be seen that the alternating vortex pattern persists over the whole downstream distance and that the vortices travel downstream through the end of the domain without any constraint. Figure 15 (*a*) shows the comparison of two- and three-dimensional cases for ω_z for $Re = 100$: the flow pattern obtained is essentially the same for both computations. At this Reynolds number, the onset of three-dimensional motion does not have much effect on the coherent structures, which remain two-dimensional.

Figures 15 (*b*) and 15 (*c*) show the comparison of two- and three-dimensional cases of ω_z for $Re = 190$ and 300 respectively. The decrease of the number of vortex structures related to the decrease of the Strouhal number can be observed in the three-dimensional case. It is also noticeable that the shear layers far from the cylinder start to show traces of smaller-scale vortex structures, which become more pronounced in the case of three-dimensional computation. On figure 16, the evolution of the ω_z component is shown as the Reynolds number increases (three-dimensional case). Beyond $Re = 200$, it is observed that smaller-scale vortices are formed along the upper and lower shear layer beyond $x/D = 3$ approximately. These are precursors of Kelvin–Helmholtz vortices, which are known to be more pronounced at higher values of Reynolds number. Three-dimensional computations comparing the vorticity fields with the present grid and with a coarser one ($150 \times 80 \times 32$), both show the existence of these small structures, which become more visible in the case of the present, finer grid. Their shedding frequency is apparently close to the main vortex shedding one

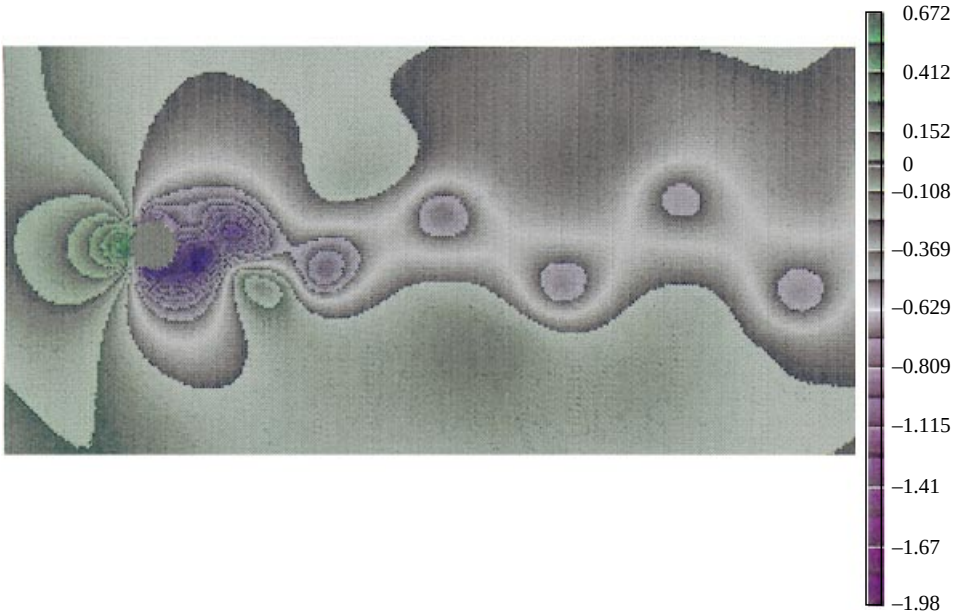

FIGURE 13. Isopressure coefficient (C_p) contours, three-dimensional case, $Re = 190$; C_p max/min= 0.672/ − 1.93 with a step of 0.2602, 10 steps.

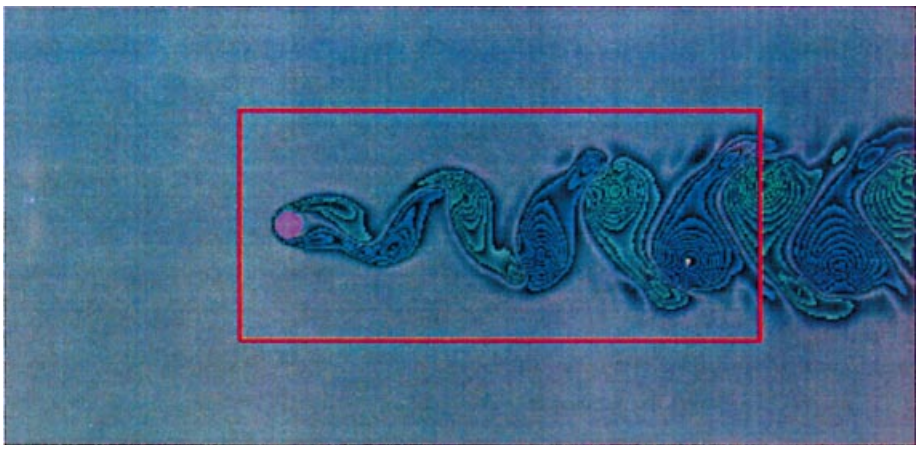

FIGURE 14. Instantaneous vorticity field, component ω_z (plane A). Display of the whole domain, $Re = 100$, three-dimensional case.

at this low Reynolds number range. Therefore, it seems that the law

$$\frac{f_{shear\ layer}}{f_s} \sim Re^{1/2}$$

suggested by the experiments of Bloor (1964), or the more recent law by Prasad & Williamson (1996) scaling as $Re^{0.67}$ can be extrapolated towards the low Reynolds number range. The vorticity contour plots at this range offer the possibility of detecting the appearance of the shear layer frequency in the case where it is close to the Strouhal one. In fact, because of this, it is difficult to distinguish the two processes by experimental signal processing techniques below Reynolds number 1300. However,

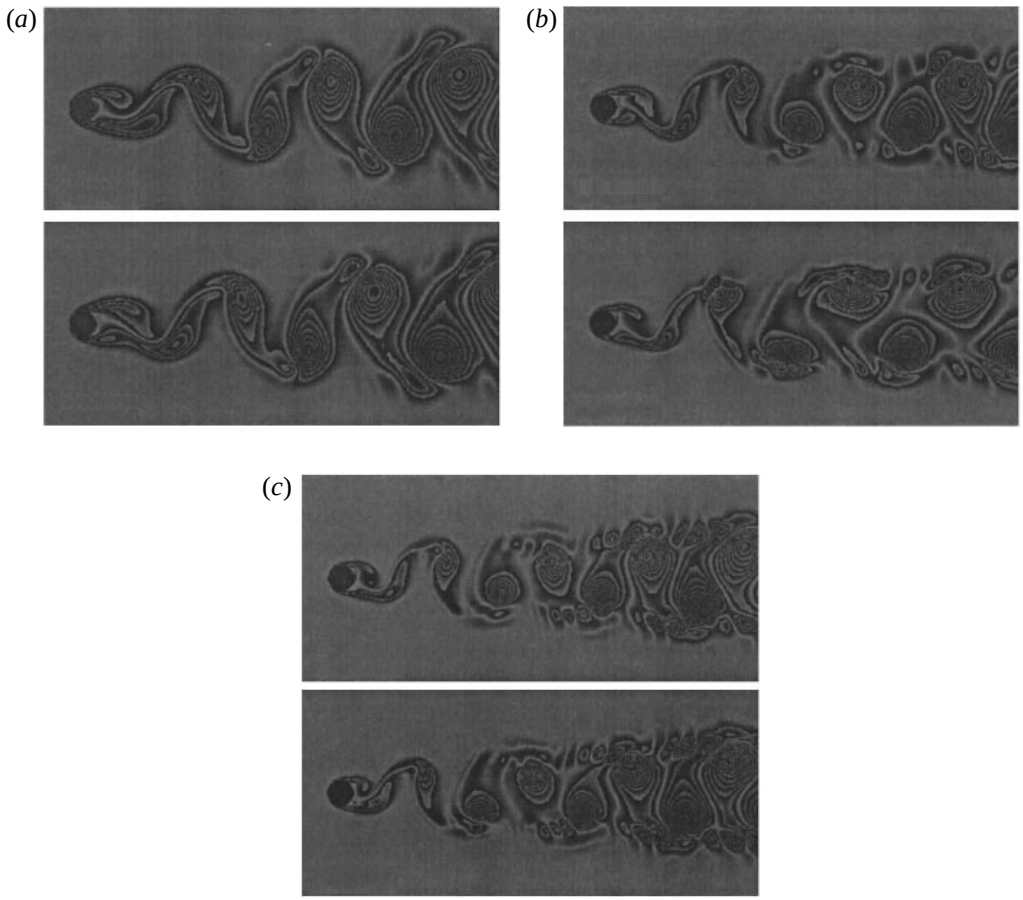

FIGURE 15. Instantaneous vorticity field, component ω_z (plane A). Display of a zoom of the domain, top: two-dimensional case, bottom: three-dimensional case; ω_z, max/min= 0.1/ −0.1 with a step of 0.02, 10 steps. (*a*) $Re = 100$, (*b*) $Re = 190$, (*c*) $Re = 300$.

the shear layer vortices obtained have a rather weak intensity, lower or equal to 0.4 in dimensionless value, compared to the wall vorticity intensity, which is of order of 20 in this Reynolds number range, as it is reported for instance in the work by Braza *et al*. (1986), among others. Therefore, these vortices do not seem to play a significant role in the transition process at the present Reynolds number range. Their impact on the shear-layer transition is important beyond Reynolds number values of 2000, as is reported by experimental studies (Bloor 1964; Wei & Smith 1986; Unal & Rockwell 1988; Prasad & Williamson 1996) and by two-dimensional numerical simulations, (Braza *et al*. 1990). In our work in progress, the influence of three-dimensionality on the shear-layer transition in the moderate Reynolds number range is being studied.

Figures 17 and 18 show the iso-contours of the vorticity component ω_x, for constant planes y/D (horizontal) and x/D (normal to the rear axis). As Re increases, it appears that ω_x is more and more fragmented. The length scale along z, between two kernels of the streamwise vortices can be assessed on figures 18 (*c*) and 18 (*d*). It is found to be $1.87D$ and $0.6D$ for Re 190 and 300 respectively. These values characterize the wavelength of the streamwise vortex structures along the span, as Reynolds number increases. Comparing to the corresponding length scales for the alternating vortices in

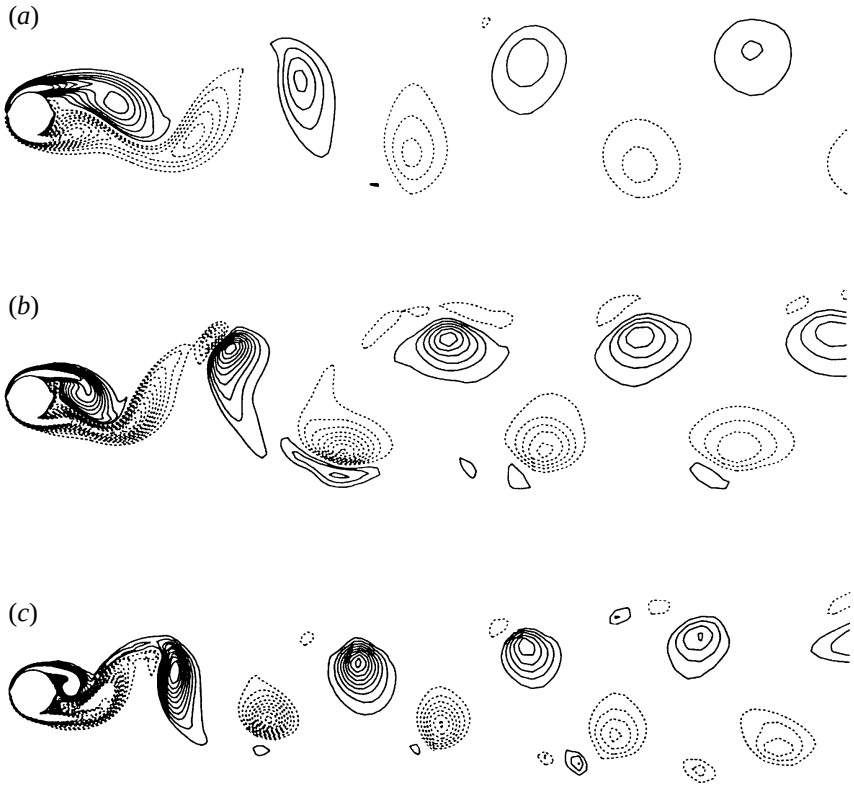

FIGURE 16. Comparative view of the vorticity field ω_z, for Reynolds numbers 100 (*a*), 200 (*b*), 300 (*c*). Iso-contour values $(-2.2, -0.4)$ and $(0.4, +2.2)$ with a step of 0.2.

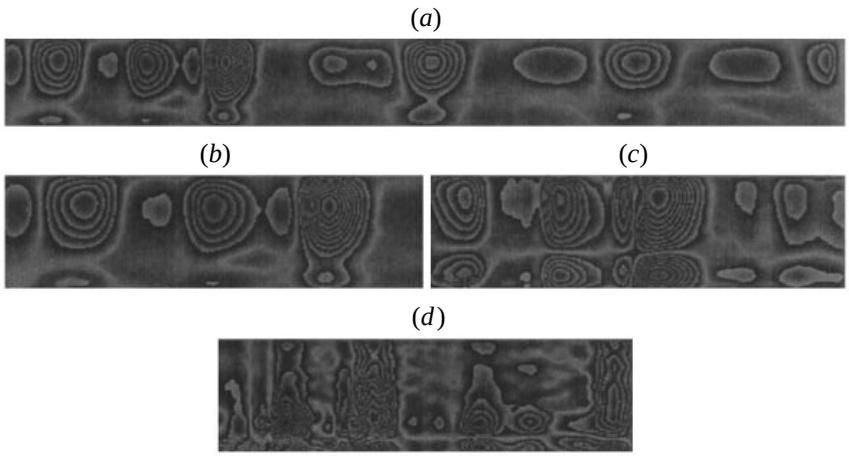

FIGURE 17. Streamwise vorticity field, ω_x, (plane B), $y/D = 0.5$. (*a*) Display of the whole domain, $Re = 100$, (*b*) zoom, $Re = 100$, (*c*) $Re = 190$, (*d*) $Re = 300$.

the (x, y)-plane, it is found that these scales are smaller than the alternating vortices length scales. This vorticity component is also shown for different planes normal to this component (i.e. x/D constant). The section of the vortex structures appears clearly. As *Re* increases, their number increases and their size diminishes. The passage

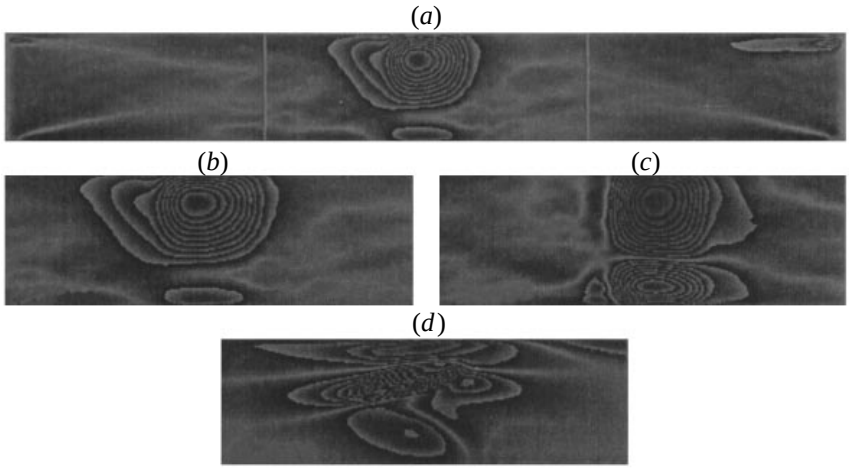

FIGURE 18. Streamwise vorticity field, ω_x (plane C): (*a*) Display of the whole domain, $Re = 100$, (*b*) zoom, $Re = 100, x/D = 2.22$, (*c*) $Re = 190, x/D = 3.05$, (*d*) $Re = 300, x/D = 5.05$.

from $Re = 100$ to $Re = 190$ is marked by the appearance of two counter-clockwise vortices. The passage from $Re = 190$ to $Re = 300$ shows the creation of a third vortex structure.

The birth of streamwise vorticity,

$$\omega_x = \frac{\partial v}{\partial z} - \frac{\partial w}{\partial y}$$

is due to the progressive development of the w-component as Reynolds number increases, owing to the action of small perturbations existing in the physical reality and also in any numerical code (see also the discussion in the first part of § 6). Under these conditions, ω_x is progressively created and it coexists with the main alternating parallel vortex rows. Owing to the action of small longitudinal perturbations, the mode selected by the present system, provided by the present DNS, is the organization of the streamwise vorticity pattern on counterclockwise vortices, in accordance to the linear stability theory of basic elliptic flows. Indeed, theoretical studies of Bayly, Orszag & Herbert (1988) show that a weak distortion of the parallel state is unstable to three-dimensional disturbances. Waleffe (1990) shows that the stability of an elliptical flow to small inviscid three-dimensional perturbations provides longitudinal counter-clockwise vortex filaments with selected wavelengths. In the present DNS study the originally two-dimensional alternating vortices correspond to the situation of an elliptical flow, where each vortex may be schematically represented as a rotational motion superimposed on a stretching, as in the elliptical stability analysis. This schematic configuration is also reported by Williamson (1996*b*), through our numerical results among other (figures 22 and 24 of that work).

The birth of streamwise vortex structures as a result of cross-stream perturbations has been previously reported in other experimental and numerical studies by Lasheras & Meiburg (1990), for the flow past a splitter plate. According to their study, the streamwise vortex filaments interact with the main vortex rows which become undulated and provide a flow pattern called mode 1. Undulation of the alternating vortices is also obtained by the present DNS, under the action of the streamwise vorticity. In order to see more clearly the three-dimensional spanwise structure,

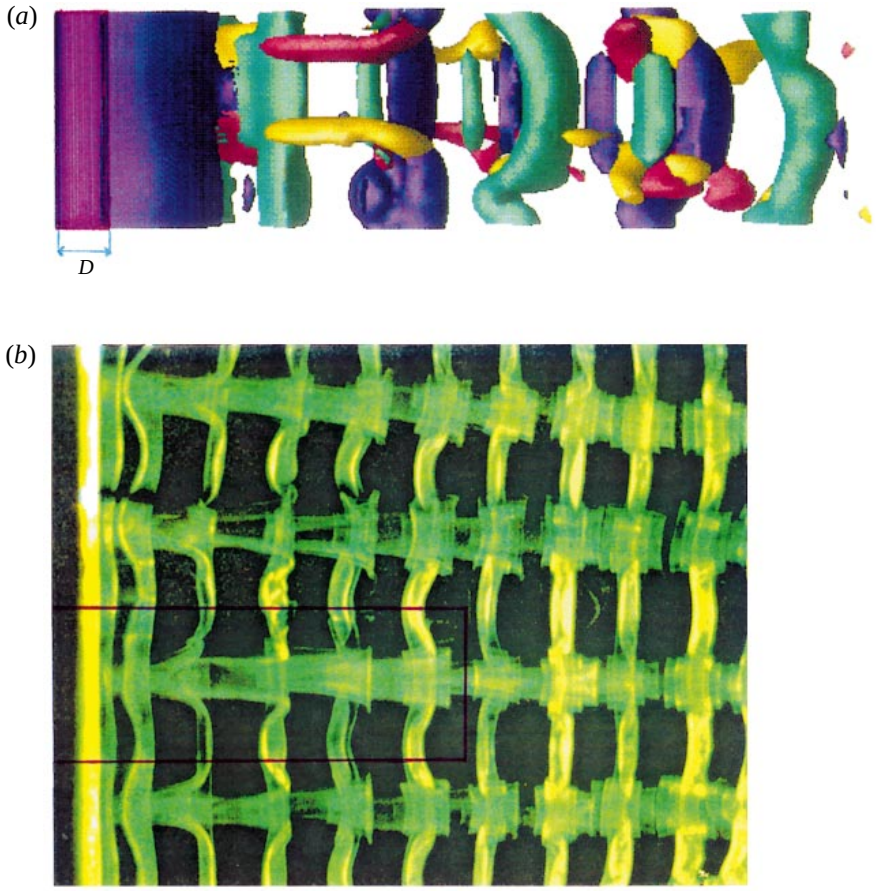

FIGURE 19. (*a*) Spanwise undulation of the main vortex rows and streamwise vortices, present study, $Re = 220$; iso-contours at values +0.25 of ω_z (green and violet) and ω_x (yellow and red) vorticity components. (*b*) Spanwise experimental flow visualization, kindly provided by C. H. K. Williamson (1992). The frame shows correspondence to the computational region explored.

figure 19 shows the iso-contours of the vorticity components ω_z and ω_x at $Re = 220$, a Reynolds number corresponding to a pronounced part of the discontinuity region (figure 11). A distortion of the main vortex filaments is obtained along the span, with the presence of streamwise vortex structures. This pattern is qualitatively comparable with the phenomenon discovered by Lasheras & Meiburg (1990) for the flow past a splitter plate (mode 1 undulation) and with experimental visualizations by Williamson (1992) for the flow past a circular cylinder (mode A).

In order to examine the evolution of the overall vortex patterns as Reynolds number increases within the range 200–300 two additional direct Navier–Stokes simulations are performed, for Reynolds number values 270 and 300, over long physical time values, using the spanwise length ($s/D = 3.72$). At Reynolds number 270, figure 20 (a, b) shows the instantaneous vorticity field where an increased number of streamwise vortices is seen. For a better visibility of these smaller-scale structures, the pattern is repeated twice along the span, on figure 20 (c). The size of these filaments is found to be approximately $l/D = 0.3$, smaller than obtained for Reynolds number 220 ($l/D = 0.5$). The spanwise periodic appearance of these structures (i.e. the distance

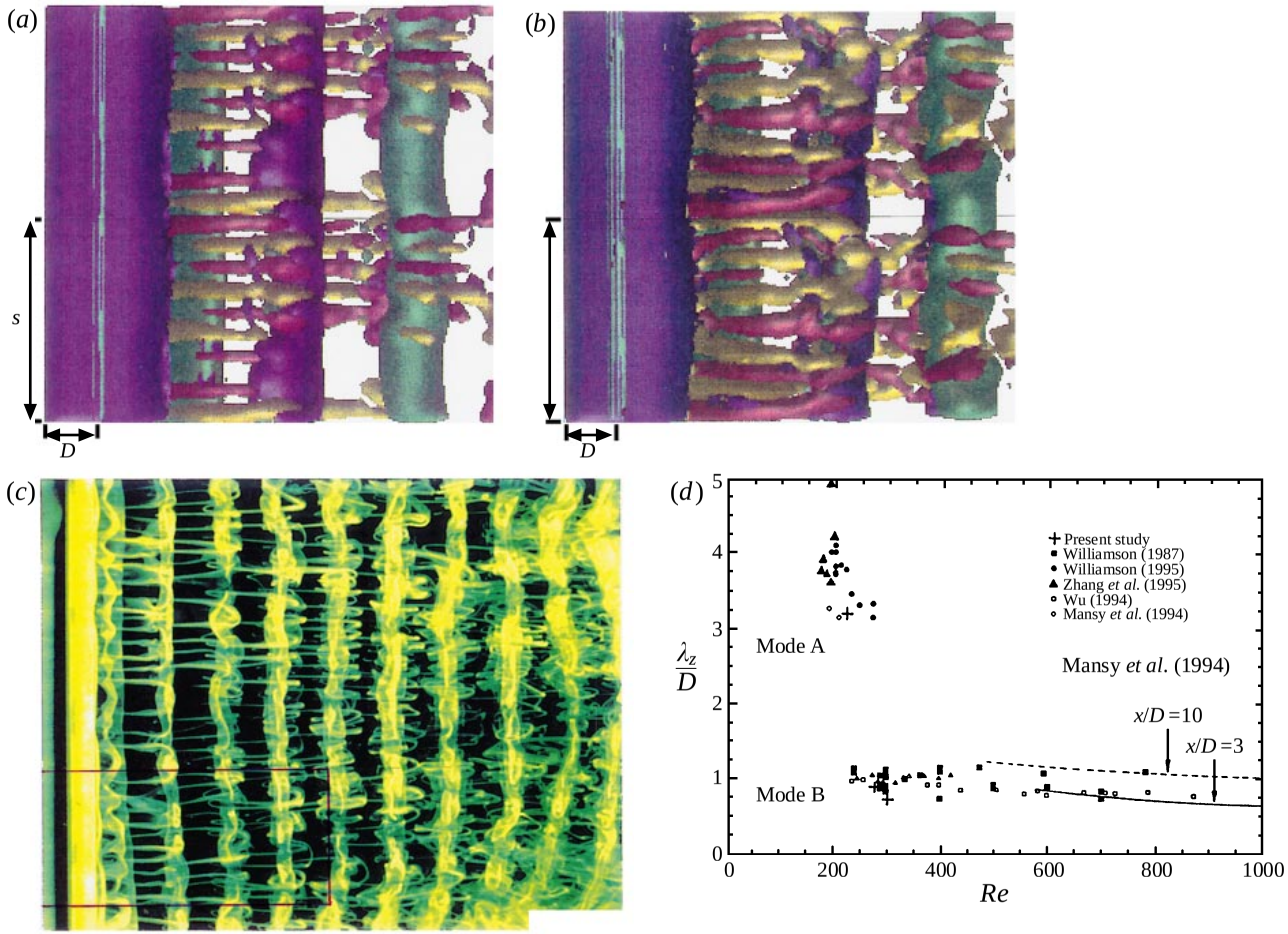

FIGURE 20. Modification of the spanwise vortex structures as Reynolds number increases; passage to mode B; (*a*) $Re = 270$; iso-contours at values ± 0.25 of ω_z (green and violet) and ± 0.25 of ω_x (yellow and mauve). (*b*) Same but for $Re = 300$. (*c*) Spanwise experimental flow visualization, kindly provided by C. H. K. Williamson (1992, 1996). The frame shows correspondence to the computational region explored. (*d*) Normalized spanwise wavelength of the streamwise vortices as a function of Reynolds number.

Re	220	270	300
size/D	0.5	0.3	0.3
λ/D	3.2	0.8	0.7

TABLE 4. Characteristics lengths of the streamwise vortices as a function of Reynolds number

between two yellow streamwise vortices), is governed by a wavelength of order $\lambda = 0.8D$, shorter than at Reynolds number 220 ($\lambda = 3.2D$), estimated as twice the distance between two counter-rotating streamwise filaments. Under the action of this streamwise vorticity, the undulation of the main, alternating eddies is also found to display a higher spanwise frequency wavy pattern. These features are found to be amplified in the case of Reynolds number 300 (figure 20), where the number of streamwise vortex filaments has increased. Their average size is of order 0.3 and the wavelength of their spanwise occurrence (i.e. the average distance between two filaments turning in the same direction) is 0.7 (see also table 4). In comparison with the experimental visualizations by Williamson (1992, 1996*a*, *b*), figure 20(*c*) this new pattern corresponds to mode B, which experimentally is characterized by a wavelength λ of order (0.75–1.2)D, in the Reynolds number range 250–400 (Williamson 1996*a*, *b*; Wu *et al*. 1994). The comparison with these experimental data is shown on figure 20(*c*, *d*), where a good agreement is obtained. Therefore, the present numerical simulation shows a considerable decrease in the distance between the streamwise structures of the same kind as Reynolds number increases from 220 to 270. This characterizes the passage from mode A to mode B flow pattern. We believe that fundamentally, this feature is the same pattern, which becomes shorter and shorter as the externally supplied energy to the system increases. However, this change (from the wavelength value 3.2 at $Re = 220$ towards 0.8 at $Re = 270$) is an abrupt one, compared to the more mild change towards the value 0.7, from $Re = 270$ to $Re = 300$. For this reason, modes A and B are indeed distinct and are characteristic forms of the transition to turbulence in the present Reynolds number range. These phenomena, occurring spontaneously in the present DNS as Reynolds number increases, are inherent features of the flow transition and are predictable by the full Navier–Stokes system.

In order to confirm these features and to study in more detail the effect of the spanwise vorticity on the undulation of the main vortex filaments, a more detailed parametric study is needed, based on a variety of spanwise lengths, including higher span values. This is being carried out in our work in progress.

The above successive changes of the flow configuration have an impact on the energy distribution and are linked to the appearance of the two discontinuities already mentioned, in the Strouhal–Reynolds number relation, as discussed in § 6.5.

6.3. *Evolution of the dynamic properties in the time domain*

The time-dependent evolution of the u- and v-velocity components are presented on figures 21–23, where the two- and three-dimensional simulations are superimposed for each Reynolds number. The spatial point of investigation is $x/D = 0.97$, $y/D = 0$ and $z = 0$, as well as a point placed in the upper mixing layer at $y/D = 0.5$. The frequency of the oscillations of u- and v-components is the same for each Reynolds number, but different between the two- and the three-dimensional simulations, for the Reynolds number value 200, in agreement with the frequency modulation obtained in

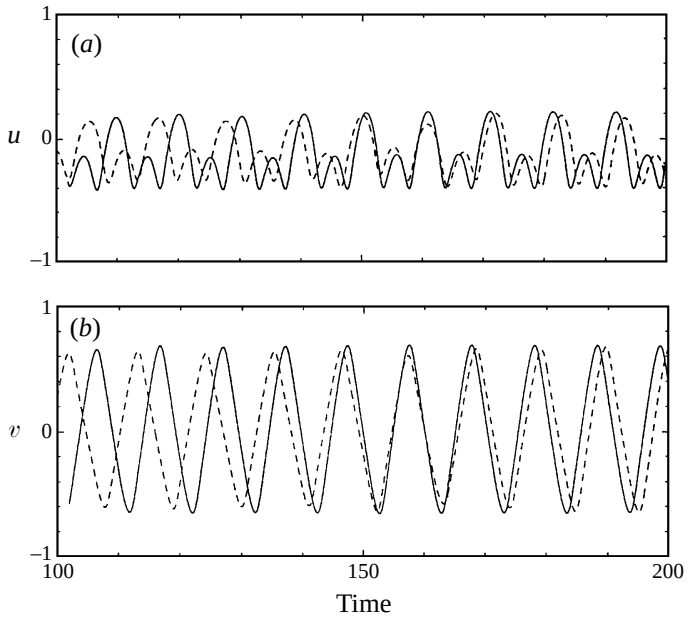

FIGURE 21. Time-dependent evolution of (*a*) *u*-component and (*b*) *v*-component. $Re = 200, x/D = 0.97, y/D = 0$: ——, two-dimensional; - - -, three-dimensional case.

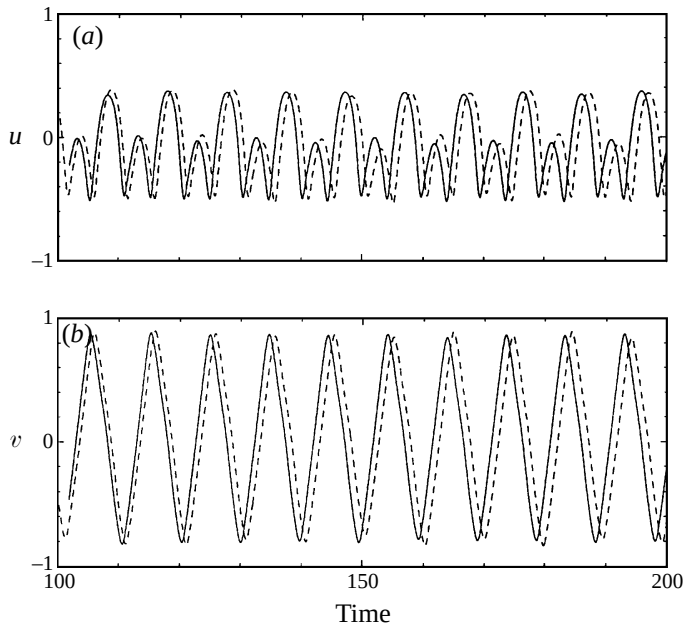

FIGURE 22. Same as figure 21 but for $Re = 300$.

the discontinuity region. These figures show the quasi-periodic character of the present flow. The establishment of this characteristic is more rapid for the *v*-component than for the *u*-component, because the periodic character of this component is masked by the overall convection effect. The amplitudes of the oscillations decrease as the sampling point moves downstream (figures 21 to 23). For a constant value of x/D

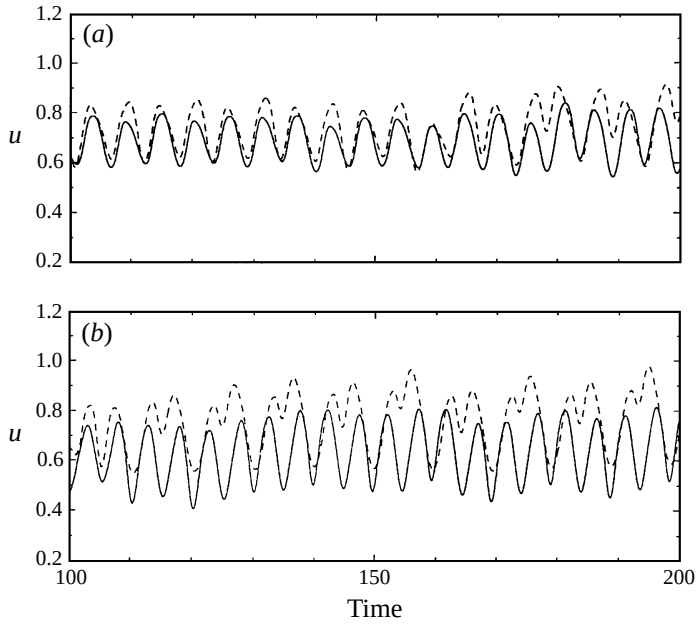

FIGURE 23. Time-dependent evolution of u-component, three-dimensional case, $x/D = 14.7$ and (a) $Re = 200$, (b) $Re = 300$: ———, rear axis, $y/D = 0$; - - -, upper shear layer, $y/D = 0.5$.

the amplitudes of the oscillations increase in the region of the shear layer, compared to the rear axis. However, the amplitudes of each component for the two- and three-dimensional simulation are comparable.

Figure 24 shows the time-dependent evolution of the separation angle, for both two- and three-dimensional simulations, for Reynolds numbers 100, 200 and 300. A general characteristic is that the amplitude of the oscillations increases as Reynolds number increases, as was the case for the drag and lift coefficients. The mean values of the separation angles are 113.5, 109.5 and 109.4 in two dimensions for the three Reynolds numbers respectively and 113.3, 107.9 and 106.5 in three dimensions. The mean values of the separation angles of the two-dimensional simulation are comparable to the ones reported in the two-dimensional numerical simulation by Braza *et al*. (1986) for Reynolds numbers 100 and 200, by using a numerical method based on O-type grids and an external radius of 114.55. For the Reynolds numbers 200 and 300, for which the three-dimensional effects are more prominent it is found that the amplitudes of the oscillations of this angle become higher than in the two-dimensional case. This feature also indicates the effect of the establishment of a chaotic motion under the action of the three-dimensionality, and this effect is superimposed nonlinearly on the predominant periodic behaviour.

Figure 25 shows the time-dependent evolution of the pressure coefficient at the rear stagnation point ($\theta = 180$) for Reynolds numbers 100, 200 and 300 for the two- and three-dimensional simulations. The reference point for the evaluation of the pressure coefficient is taken in the vicinity of the upstream upper corner of the computational domain. The amplitude of the oscillations of these signals increases as Reynolds number increases. The oscillations of C_p clearly show the simultaneous impact of the two separation points and of the two rows of alternating vortices. Owing to the formation of more and more finer-scale classes of vortices in the (x, y)-plane and

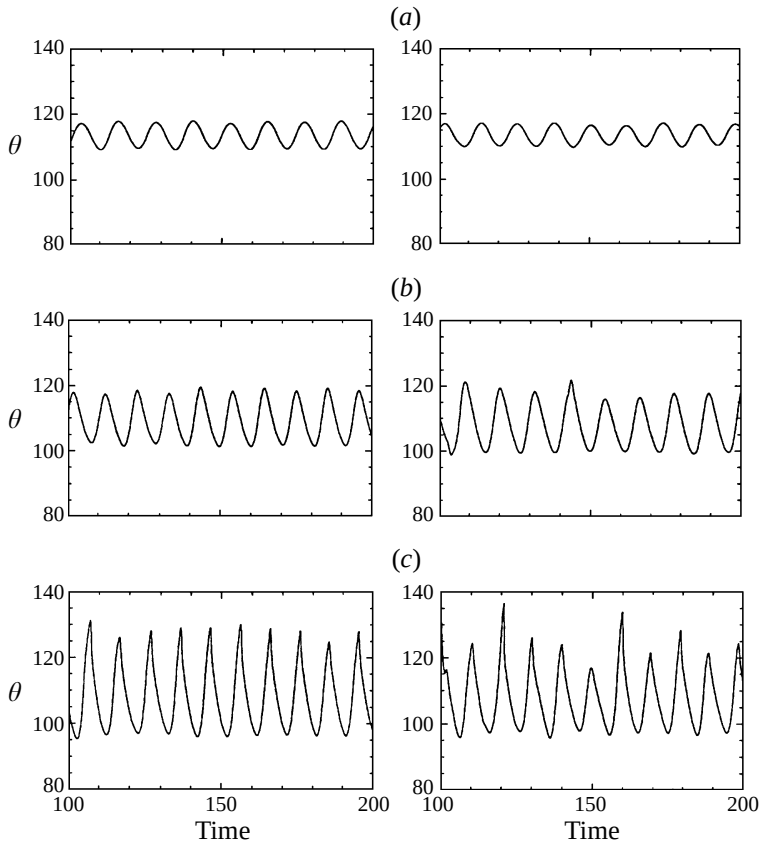

FIGURE 24. Time-dependent evolution of the separation angle, two-dimensional case (left), three-dimensional case (right): (*a*) $Re = 100$, (*b*) $Re = 200$, (*c*) $Re = 200$.

also in the streamwise and spanwise directions, harmonics become more pronounced within each period of the fundamental, as Reynolds number increases. Especially because of the location of the base pressure point on the rear symmetry axis, this phenomenon is more amplified than at other points in the field, because it is subject equally to the simultaneous effect of the upper and lower regions, with respect to the rear axis. Although this phenomenon is weak at $Re = 100$, it becomes more significant for $Re = 200$ and 300. This behaviour is confirmed by the pressure spectra shown in § 6.6. Indeed, the signature of $2f_s$ is clearly obtained and is amplified as Reynolds number increases.

The mean base-pressure coefficient values are shown on figure 26 (*a*) and in table 5. They are compared to the experimental results by Williamson & Roshko (1990) and to other computational results (figure 26 *b*). In the present study, it is shown that there exists a difference between the two- and three-dimensional cases, for $Re = 200$ and 300. However, the smaller span ($s = 2.25D$) provides C_p values higher than the experimental ones (in absolute value), for the Reynolds numbers 200 and 300, for which the three-dimensional effects are more significant. This seems also to be a general characteristic of other computational studies shown on this figure. Concerning the present study, it is noticeable that the higher spanwise length case ($s = 3.72D$)

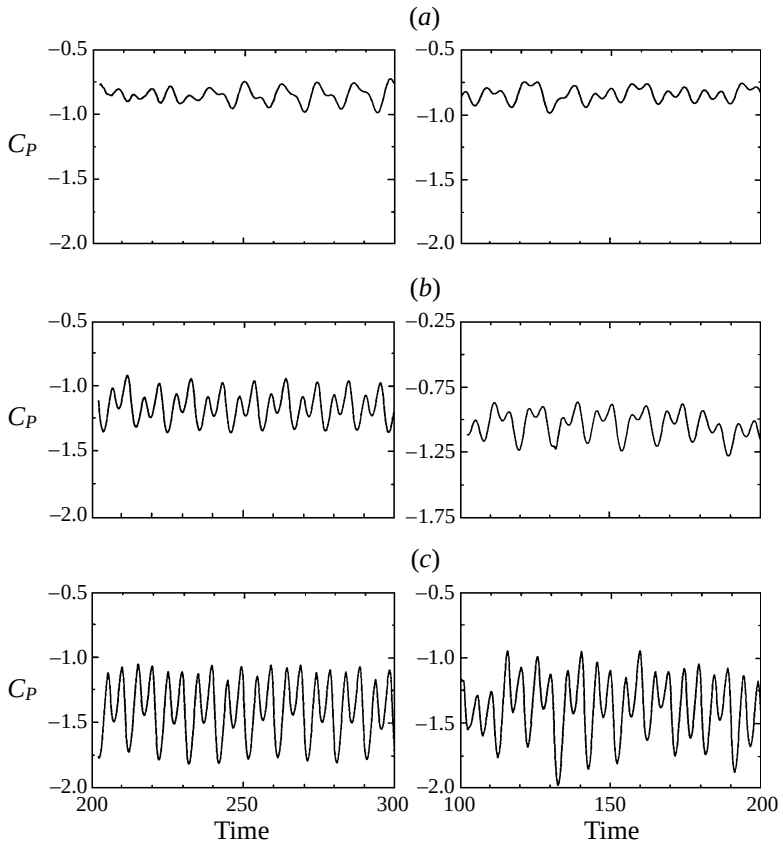

FIGURE 25. Time-dependent evolution of the pressure coefficient at the rear symmetry point ($\theta = 180°$), two-dimensional case (left), three-dimensional case (right): (*a*) $Re = 100$, (*b*) $Re = 200$, (*c*) $Re = 200$.

Re	C_{P_b}(2D)	C_{P_b}(3D)
100	−0.848	−0.830
200	−1.160	−1.054
220	–	−0.960
300	−1.412	−1.378

TABLE 5. Mean base pressure coefficient versus Reynolds number.

provides $C_p = -0.96$, which is quite close to the experiments, compared to other studies computations.

6.4. *Mean velocities and fluctuation correlations in the near wake*

In this subsection the properties of the onset of fluctuating motion in the flow field are given, by evaluating the temporal mean quantities for the velocity components and for their correlations in the region of the near wake from the present three-dimensional direct Navier–Stokes simulation. These quantities quantify the development of the fluctuating motion, which is due to the quasi-periodic dynamic characteristics of the main vortices and which also contains the precursors of the birth of smaller-scale

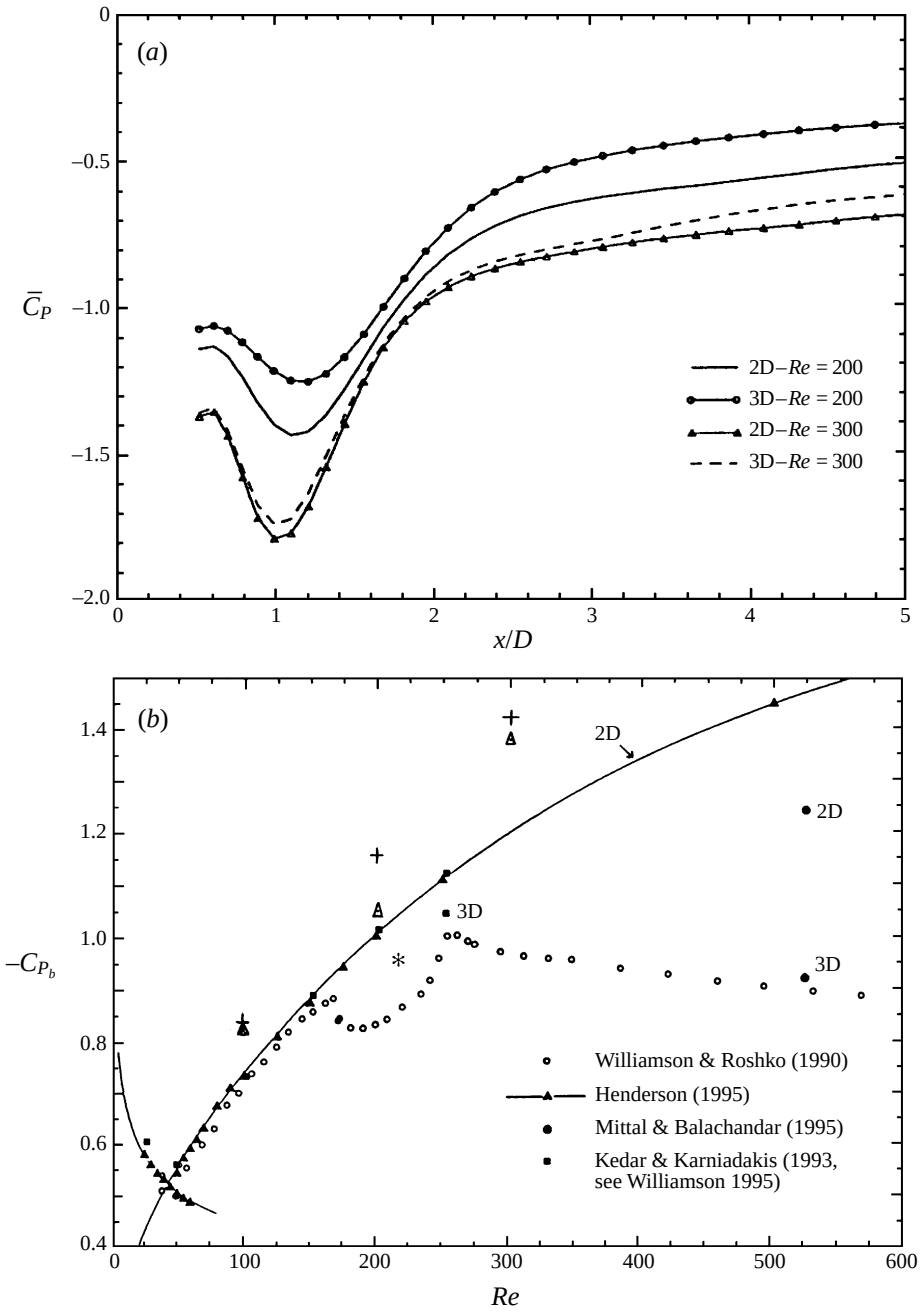

FIGURE 26. (*a*) Mean pressure coefficient along the rear axis as a function of Reynolds number. (*b*) Mean base-pressure coefficient versus Reynolds number. This study: +, two-dimensional; △, three-dimensional $s/D = 2.2$; *, three-dimensional $s/D = 3.72$.

turbulent motion, according to the discussions in § 6.2. The evaluation of the mean velocity components and of the Reynolds stresses is vital information concerning the impact of the different vortex structures in the transfer mechanisms, especially in a region where the similarity considerations are not valid. The strong intensity of the

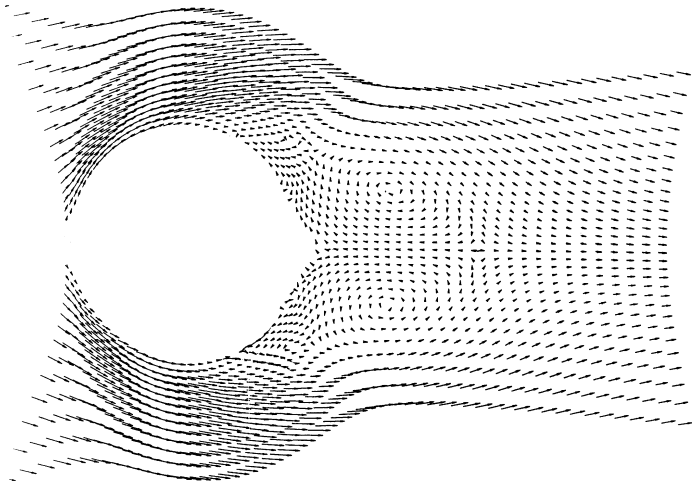

FIGURE 27. Mean velocity field, $Re = 200$, two-dimensional case.

coherent structures developed in the near wake deeply modify the dynamics in this region, compared to the far region beyond $x/D = 70$ approximately, where there is an equilibrium among the different structures under the diffusion and dissipation mechanisms and where the energy spectrum is governed by the laws of statistical equilibrium, in the sense of Kolmogorov theory. Therefore, it is important to quantify the increase and decay of the different properties of the fluctuating motion in the near region, by taking into account the impact of the coherent structures in this flow area, a possibility which is precisely offered by the present simulation. Furthermore, this detailed evaluation of the mean quantities and of the velocity correlations in such a highly separated region may be a laborious task to carry out experimentally, needing advanced measurement techniques.

In order to do this study, we have performed a post-treatment of the time-dependent velocity signals in the established phase, taken from the three-dimensional simulation at Reynolds numbers 200 and 300, which consists in the evaluation of the temporal mean quantities and of the stress correlations, according to the Reynolds (1894) decomposition. These statistics are taken in the mean plane $(x, y, s/2)$, s being the spanwise length, on signals containing a decade of periods of the fundamental frequency. The present analysis produces basically the influence of the von Kármán instability (which is mainly governed by two-dimensional mechanisms), in the mean plane of the near wake, on the mean flow quantities and velocity correlations, under the effect of the birth of three-dimensional motion. However, in order to produce the same kind of statistics along the spanwise direction, a much larger spanwise length than 3.72 would be needed. In the following, the symbols correspond to the mean values of the functions. The overbar symbol has been omitted, for the sake of simplicity. The figures of this section concern the three-dimensional case unless it is differently specified.

6.4.1. *Boundary layer and separation region*

A detailed analysis of the three-dimensional boundary layer structure is performed on the spanwise section $(z/D = s/2)$.

The mean velocity vector field shows a symmetric pattern with two attached vortices and two smaller secondary attached vortices in the vicinity of the separation points.

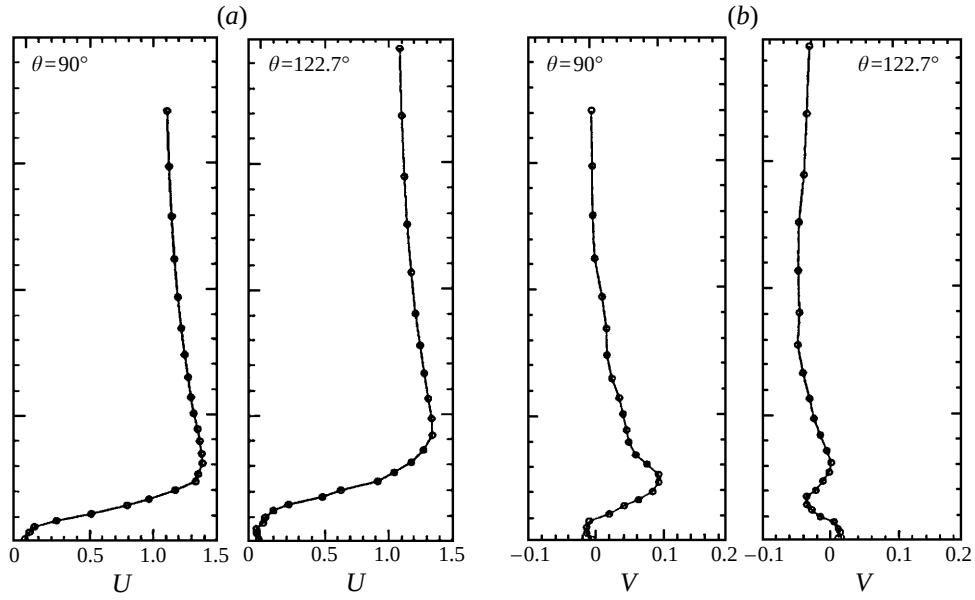

FIGURE 28. (*a*) Mean U-velocity profiles at different radial positions, (*b*) mean V-velocity profiles at different radial positions; $Re = 300$.

The overall pattern is the result of the time-averaged vortex street pattern (figure 27). The recirculation length can be determined from this figure, as a characteristic dynamical parameter of the near wake, as well as the vertical distance between the centres of the two mean attached vortices. These distances are found to be $1.25D$ and $0.48D$ respectively, for $Re = 200$.

Figure 28 (*a*) shows mean U-velocity profiles at the radial positions $\theta = 90°$ and $\theta = 122.7°$, chosen upstream and in the separation region at $Re = 300$. The boundary layer effect upstream of separation is clearly obtained. The flow reversal at the last three sections corresponds to the three-dimensional separated region, whose effect is more pronounced at the last radial position.

Figure 28 (*b*) shows mean V-velocity profiles in the boundary layer at $\theta = 90°$ and $\theta = 122.7°$. The effect of the three-dimensional recirculating zone is also clearly shown. The present velocity profiles show inflection points which are responsible for the amplification of the unstable character in the transition process, in the presence of the three-dimensionality. Figure 26 (*a*) shows the mean pressure coefficient along the rear axis for different Reynolds number values. The suction effect, due to the near-wake recirculation area, is clearly obtained and becomes more pronounced as Re increases.

6.4.2. *Mean velocity profiles*

Figures 29 (*a*) and 29 (*b*) show the spatial evolution of U_{mean} along the rear axis for Reynolds numbers 200 and 300. The reattachment length is determined as the second point of vanishing U_{mean}, from negative to positive values. It is found that $x/D = 1.80$ for $Re = 200$ and $x/D = 1.59$ for $Re = 300$. Figure 29 (*c*) shows the longitudinal mean velocity at different x/D sections. The velocity deficit due to the wake effect is clearly obtained. The variation of the deficit velocity along the rear axis, $| U_{mean} - U_o |$,

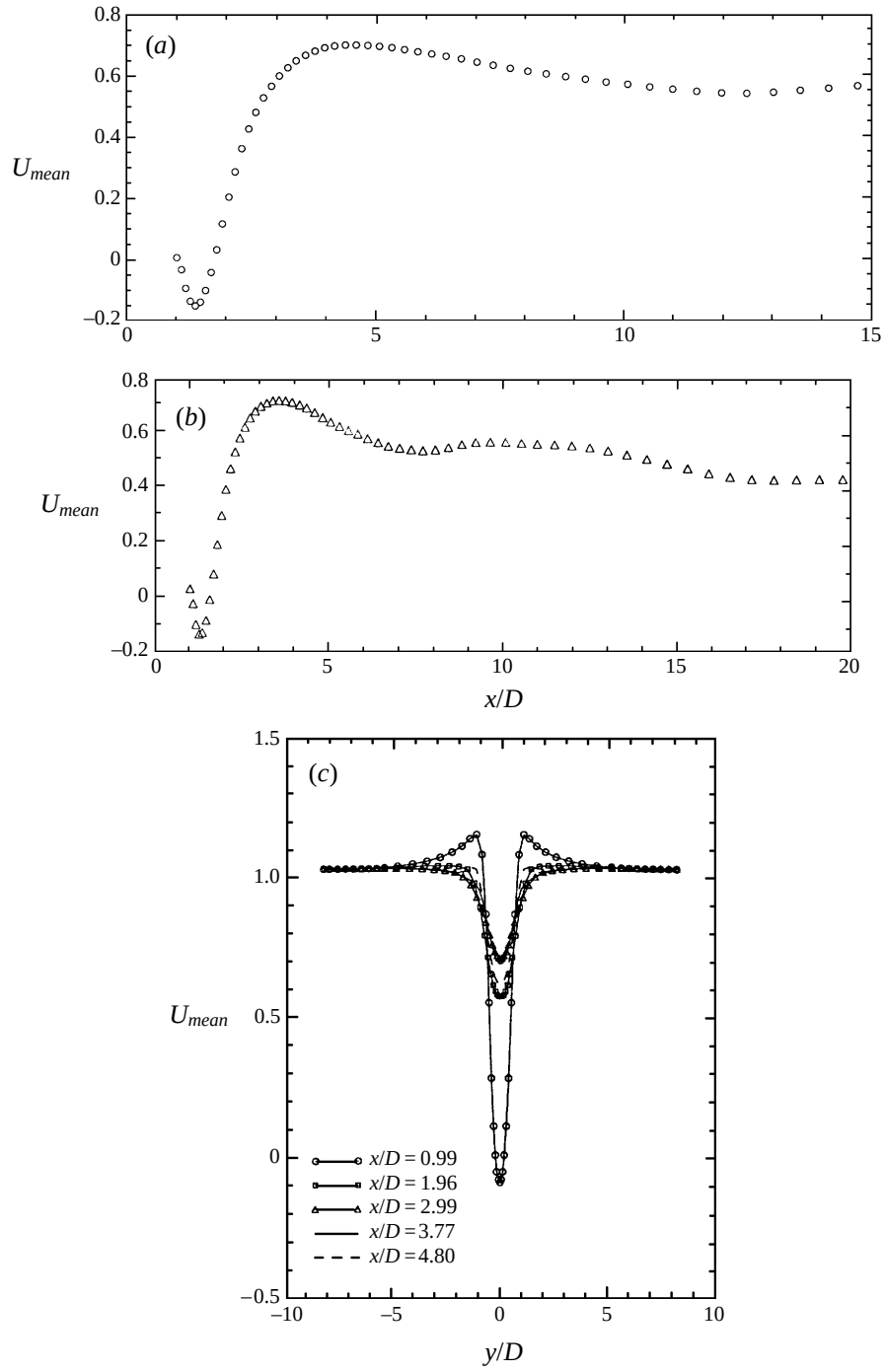

FIGURE 29. U_{mean} velocity along the rear axis, (*a*) $Re = 200$, (*b*) $Re = 300$. (*c*) U_{mean} velocity profiles along fixed x/D sections, $Re = 300$.

where U_o is the upstream velocity, can be calculated in the far wake, according to the assumption of similarity and to the classical theories of Boussinesq, Prandtl and Taylor (reported by Hinze 1975) and it varies as

$$\frac{U_{max\,def}}{U_o} = A\,\left(\frac{x+R}{D}\right)^{-0.5},$$

where R is the cylinder's radius. According to this, the maximum deficit at the far region scales as $x^{-0.5}$. Therefore, the mean velocity U_{mean}/U_o along the rear axis scales as

$$1 - A\,\left(\frac{x+R}{D}\right)^{-0.5}.$$

In the present study, the variation of the longitudinal mean velocity in the very near wake, where similarity laws cannot be applied, displays a totally different behaviour. It follows first a decreasing path with the minimum value at $x/D = 1.3$ for $Re = 200$, an increasing path with a maximum at $x/D = 4.1$ and finally a slightly oscillatory path towards a general decreasing trend.

The transverse mean velocity profiles are shown in figure 30 (*a–c*) along the rear axis and for several x stations. The antisymmetric configuration (figure 34 *c*) illustrates clearly the effects of the mean recirculation region. The maximum absolute values are found to decrease more rapidly in the $Re = 300$ case because of the reduction of the mean recirculation length. Moreover, the highest maximum value is more pronounced in the $Re = 300$ case due to a higher vorticity strength at this Reynolds number value.

Along the rear axis, the vertical mean velocity (figures 30 *a* and 30 *b*) shows a progressively decaying behaviour downstream. The spatially 'oscillatory' pattern is due to the travelling of the alternating eddies, in accordance with the contour plots shown in § 6.2.

6.4.3. *Reynolds stresses*

The longitudinal Reynolds stress is shown at several x/D stations as a function of y/D (figure 31 *a*). A two-lobe structure is observed in all cases. This shows the travelling of the organized alternating vortices through the corresponding sections. The distance between the two peaks corresponds to the distance between the kernels of the two rows of alternating vortices as it is shown in § 6.2. The peaks are directly linked with the amplitude of the oscillations of the u-component in the time domain.

Figure 31 (*b*) shows the stress v^2 at different downstream sections. The maximum values are on the rear axis in accordance with physical experiments of Townsend (1956), Uberoi & Freymuth (1969) and Boisson (1982). In fact, the maximum amplitudes of the v^2 Reynolds stress component appear on the rear axis, because there this component is submitted to the equally weighted influence of the two alternating vortex streets, and this also explains why $v_{\mathrm{r.m.s}\ max}$ is located on this axis.

The shear stress profiles are shown for several x stations in the wake, figure 31 (*c*). They present a generally antisymmetric character, where the two extrema are due to the passage of the central areas of organized alternating vortices, figures 16, 19 and 20. The peak amplitudes of the shear stress indicate the position where the signals of the two components are in phase. The vanishing shear stress indicates the regions where the u- and v-signals are out of phase by 180°. At $x/D = 0.99$, we can observe two more peaks near the rear axis. This pattern disappears for sections beyond the recirculation region. These smaller peaks are due to an increase of the u-fluctuation within the recirculation area, whereas this fluctuation becomes very small further

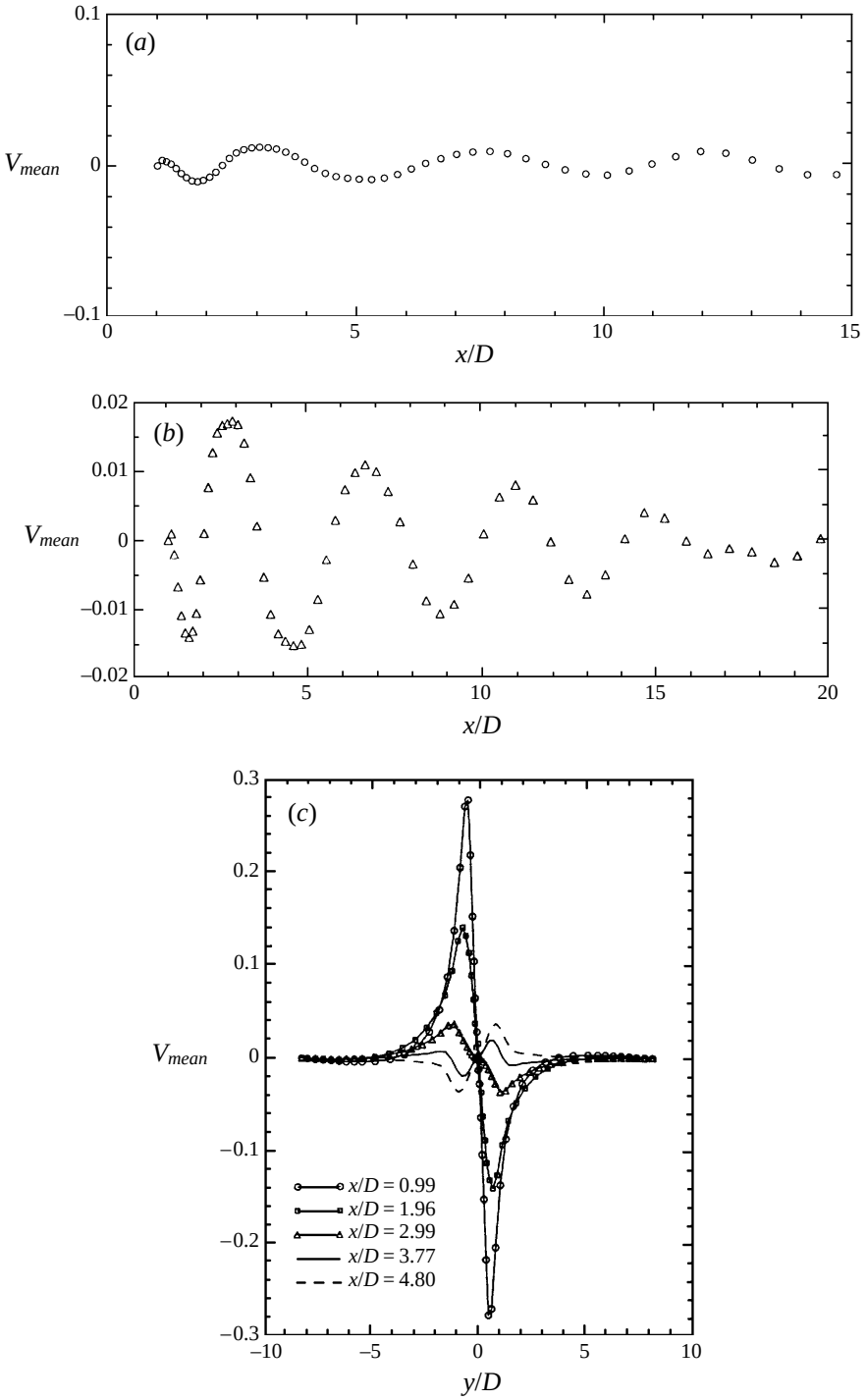

FIGURE 30. V_{mean} velocity along the rear axis, (*a*) $Re = 200$, (*b*) $Re = 300$. (*c*) V_{mean} velocity profiles along fixed x/D sections, $Re = 300$.

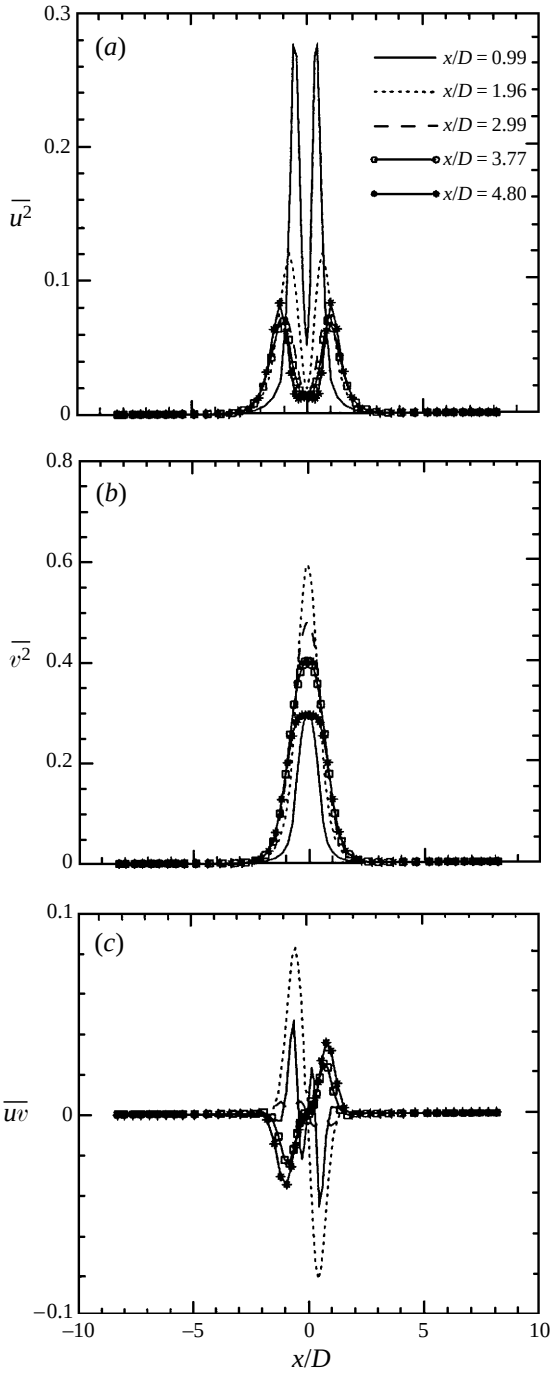

FIGURE 31. (*a*) $\overline{u^2}$ Reynolds stress, (*b*) $\overline{v^2}$ Reynolds stress, (*c*) $\overline{uv}$ Reynolds stress; $Re = 300$.

downstream. In fact, the *u*-fluctuation has a higher level in the region of negative mean values, owing to a strong interaction between the vortices and to a weaker impact of the convection effect in this near-wall area.

According to the similarity assumption valid in the far wake, the variation of the

X/D	$\overline{u^2}$	$\overline{v^2}$	$\overline{uv}$
0.99	0.28	0.31	0.005
1.96	0.12	0.59	0.085
2.99	0.08	0.49	0.006
3.77	0.078	0.42	0.025
4.80	0.09	0.30	0.036

TABLE 6. Maximum $\overline{u^2}$, $\overline{v^2}$, $\overline{uv}$ stresses, $Re = 300$.

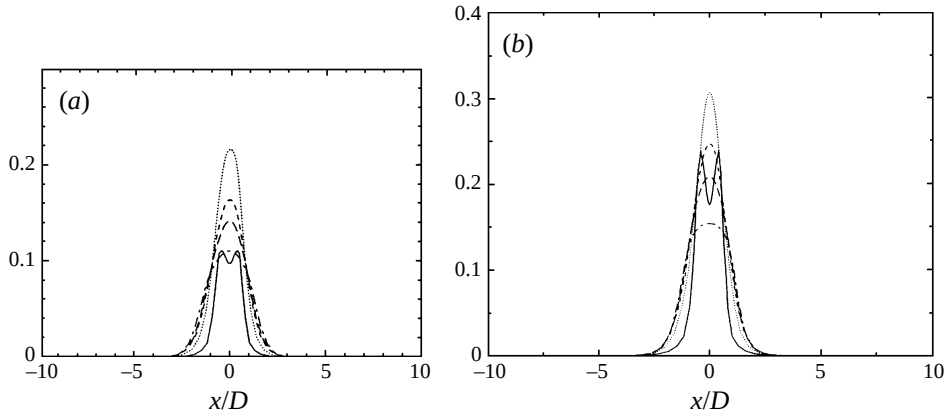

FIGURE 32. Mean kinetic energy, k, of the fluctuating part, x/D sections, (a) $Re = 200$, (b) $Re = 300$.

shear stress in the far wake and at large values of Reynolds number, Hinze (1975), scales as

$$(y/x + R)(U_{def}/U_o),$$

U_{def} being the deficit velocity as a function of x and y. In this way, for a constant y-value, taken in this case as that corresponding to the maximum shear stress, uv scales as x^{-1}. In the present study, the maximum values of the longitudinal, vertical and shear stresses in the near wake, are presented on table 6. A non-monotonic variation is obtained in all cases.

6.4.4. *Fluctuating and total kinetic energy*

The mean value of the fluctuating kinetic energy, k (figure 32 a, b), is obtained by obtaining the temporal mean of

$$\frac{u^2 + v^2 + w^2}{2}$$

where $u = U - U_{mean}$ The mean total kinetic energy, E (figure 33 a–d), is obtained by obtaining the temporal mean of the function

$$\frac{U^2 + V^2 + W^2}{2},$$

where U is the time-dependent velocity signal. The variations of the maximum values of k are not monotonic in the near wake. The highest peak is found to occur at section $x/D = 1.96$ for $Re = 200$ and the lowest at $x/D = 0.99$. This behaviour is more pronounced at $Re = 300$. The mean value of the total kinetic energy is

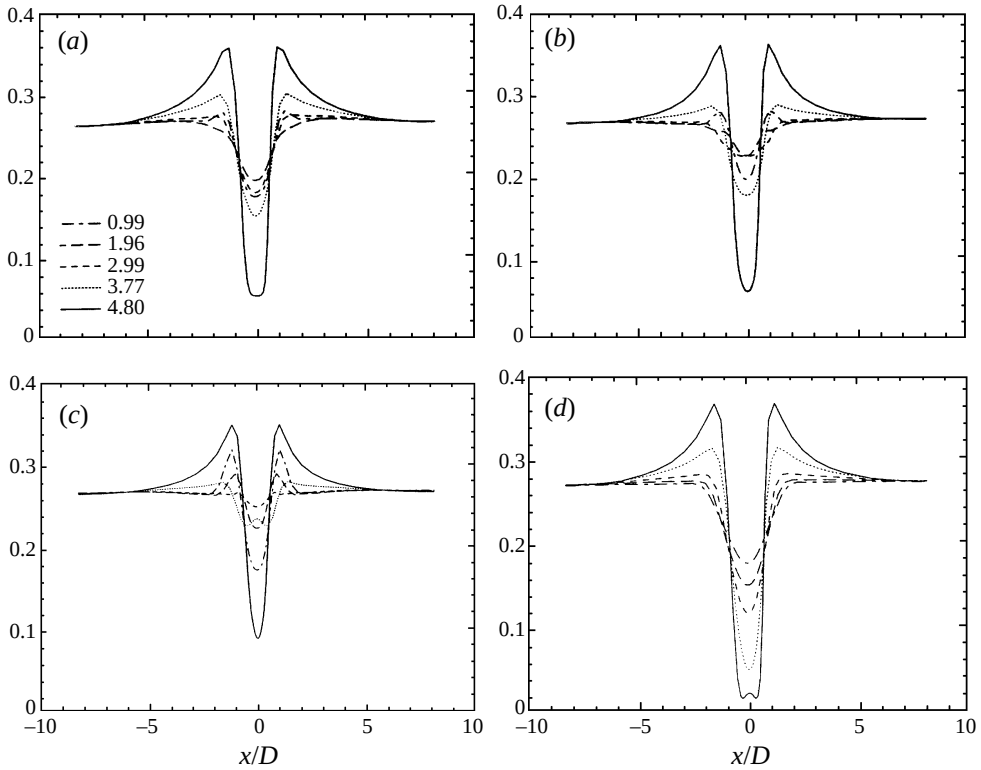

FIGURE 33. Mean total kinetic energy, E, x/D sections: (*a*) $Re = 200$, three-dimensional case; (*b*) $Re = 200$, two-dimensional case; (*c*) $Re = 300$, three-dimensional case; (*d*) mean total kinetic energy, $Re = 100$.

quantified for the same sections. A characteristic value is the energy peak at the rear axis. It is found that a higher energy level than this characteristic value appears in all sections for $Re = 300$ compared to $Re = 200$. Furthermore, at $Re = 200$, the mean total energy is found to have a maximum value of 0.06 near the rear axis in the two-dimensional case, whereas its maximum value is 0.051 in the three-dimensional case. This decrease of the total energy is in accordance with the phenomenon of reduction of the fundamental frequency at this Reynolds number value, because of the amount of energy attributed to sustaining the smaller-scale developed motion, as discussed in the next subsection, concerning a physical analysis of phenomena appearing in the discontinuity region.

Recapitulating the outlines of the study presented in this section, the mean and fluctuation correlations in the near wake is quantified and related to the eddy structure signature in the present Reynolds number range corresponding to an important transition state. This is achieved by using the complete three-dimensional simulation and by performing a post-treatment of the unsteady evolution of the different flow properties in the near wake.

6.5. *Physical mechanisms in the discontinuity region of the St, Re relationship*

In this subsection, the appearance of the discontinuity region is related to the streamwise vortex structures obtained and to the quantification of the energy levels in the near wake, for the Reynolds number range 100–300. The discussion is a complemen-

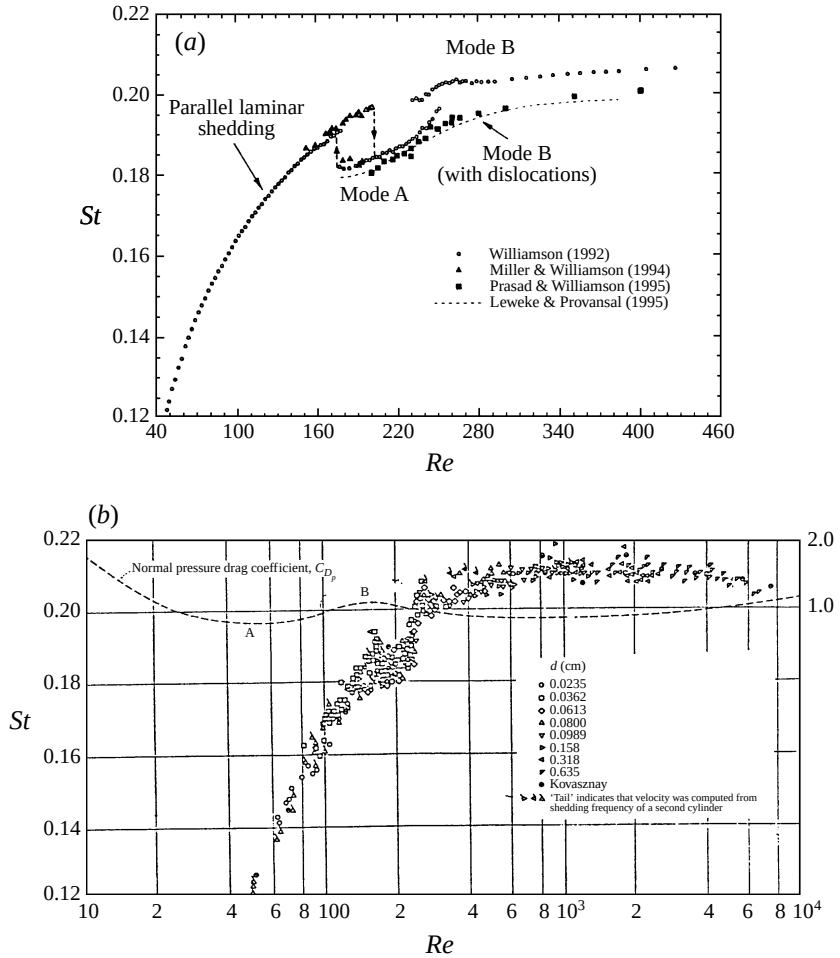

FIGURE 34. (*a*) Strouhal–Reynolds number relationship according to recent experimental studies, figure taken from Williamson (1996*a*). (*b*) Strouhal–Reynolds relationship over the high Reynolds number range, Roshko (1954).

tary way to see the reasons for the appearance of this phenomenon, in addition to stability analyses and model equation approaches attempted by other studies. The physical origins of the frequency modulation between the two discontinuities may be due to a number of reasons, which still need to be analysed. The physical experiments by Prasad & Williamson (1997) and by Leweke & Provansal (1995) attribute a substantial frequency drop, especially beyond $Re = 220$, to the appearance of vortex dislocations (figure 34 *a*), firstly discovered by Williamson (1992). Although the prediction of vortex dislocations is not the object of the present study, note that the predicted frequency value at $Re = 250$ is closer to the path of the curve including the dislocation. An ongoing study of ours has as a main objective the analysis of this phenomenon. Concerning the general shape of the curve with the discontinuities, the experimental studies also report the passage from mode A to mode B, both related to the formation of streamwise vorticity. In the Section on the numerical visualizations of the present paper, it has been seen how the streamwise vorticity develops progressively, from Reynolds number 100 to Reynolds number 300. A drastic change occurs

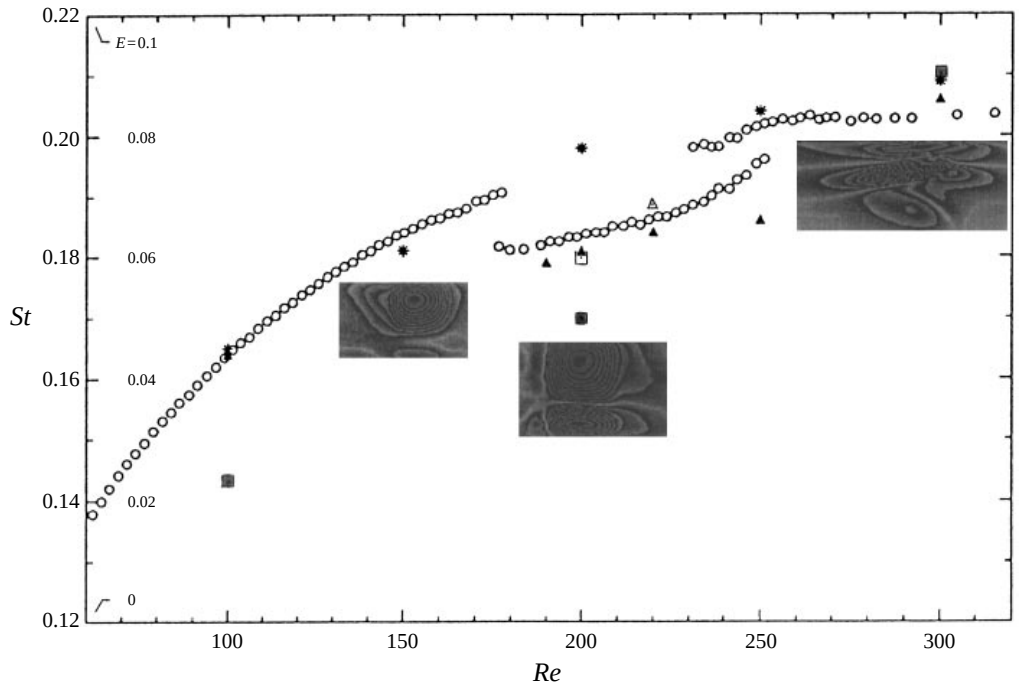

FIGURE 35. Strouhal–Reynolds number relationship according to the present numerical simulation; link with the streamwise vortex pattern and with the total energy level. ○, Experimental results, Williamson (1989); * , this study two dimensions; ▲, this study, three dimensions, $s/D = 2.25$; △, three dimensions, $s/D = 3.72$; ■, characteristic total energy distribution in the near wake, three dimensions; □, two dimensions

in the streamwise vorticity pattern in the intervals 100 to 200 and 200 to 300, characterized by the formation of streamwise vortex loops. On the other hand, a Strouhal number frequency is directly related to a representative characteristic velocity U_S and to its corresponding energy, scaling as U_S^2. This energy amount is directly related to the organized eddy motion, shed with the frequency f_S. It is therefore essential to relate the frequency modulations obtained to the corresponding energy amounts, as they are quantified in the previous subsection.

We consider the evolution of Strouhal number versus Reynolds number variation in the Reynolds number range 100 to 300 as obtained by the present simulation in figure 35, where we have superimposed the different vortex patterns according to the flow contour plots of § 6.2. The Strouhal number shows a generally increasing behaviour with a progressively delayed rate towards $Re = 300$, including the discontinuity region. Beyond this value, it is observed that the Strouhal number does not vary much as a function of Reynolds number. Its variation reaches a threshold, Roshko (1954), figure 42 (*b*).

For Reynolds number values lower than 180, there is no other substantial structure in the flow field apart from the main alternating vortices. During this phase of the curve, the externally supplied energy is transmitted to the von Kármán vortices.

Beyond $Re = 180$, finer-scale chaotic motion is developed which can be illustrated by the generation of the shear layer vortices and of longitudinal and transverse vorticity (figures 17 and 18). As we have seen in the § 6.2, on figure 18 (*a*), the isovorticity contours show the formation of two counter-rotating longitudinal vortices.

Downstream (figure 18 *b*), two other counter-rotating vortices are formed turning oppositely compared to figure 18 (*a*). This phenomenon 'pumps' part of energy from that externally supplied. Indeed, the peak of the total energy level (figure 33) is 0.051 for $Re = 200$, whereas this level is 0.06 according to the two-dimensional approach, where these vortex structures are inhibited. Hence, the energy attributed to the main vortices decreases and the rate of increase of the Strouhal number is reduced, causing the discontinuity to appear. The related amount of energy decrease is quantified in the previous subsection and it is in accordance with the present discussion. Nevertheless, the discontinuity is limited because of the threshold observed on the curve. In fact, this saturation phenomenon is caused by the balance of the energy exchange between the vortex shedding motion and the generation of fine-scale turbulent motion. Indeed, at $Re = 300$, the total energy peak value (§ 6.4) is 0.09, a higher value than the corresponding value at $Re = 200$.

Beyond $Re = 300$, the increase of external energy does not lead to a consequent increase of the Strouhal number, because the increase of energy is thought to sustain the more and more pronounced fine-scale turbulent motion. Indeed, figure 18 (*d*) shows a new fragmentation of the longitudinal vortices. These new structures are smaller and for this reason less inertial. Therefore, we can suppose that they have a shorter life than the structures of the second part of the curve. As no other frequencies incommensurable to the Strouhal number are generated (see the discussion in § 6.6), we can suppose that the frequency of appearance of the longitudinal vortex structures is comparable to the Strouhal number. Thus, during a phase of observation corresponding to one period of the fundamental vortex shedding, the energy consumed by this configuration is lower than the amount of energy used by the previous configuration. For this reason, the von Kármán vortex pattern gains some energy (the characteristic level reaches the value 0.09 at $Re = 300$) and hence the Strouhal number increases and leads to the second discontinuity of the curve. Therefore, the formation of the discontinuity region is marked by a discontinuity in the variation of the total energy distribution (figure 35). This feature has not been shown before the present study.

Therefore, the formation of the discontinuity region illustrates a transition state in order to establish a new equilibrium between the organized motion and the fine-scale turbulence in the physical process as its energy increases. These mechanisms are directly related to the nonlinear and dissipative character of the process.

6.6. *Spectral analysis*

In this subsection we analyse the impact of the quasi-periodic evolution of the coherent structures in the frequency domain, by means of a spectral analysis, carried out on the basis of the time-domain signals presented in § 6.3. The spectral analysis will also compare the two- and three-dimensional simulations. The spectra are obtained by the fast Fourier transform method (FFT). The sampling rate of the signals is equal to $1/\Delta t$, where Δt is the time step of the numerical simulation. In the present case, the sampling rate is 50. This implies that the maximum frequency obtained by FFT is half of the sampling rate, i.e. 25. However, only the range of low and moderate frequencies is explored in this study, as most related to the wake instabilities. For this reason, a sub-domain of the spectrum is presented. The time step used provides a sampling rate much higher than the frequency range of interest, hence the Nyquist criterion is largely satisfied in the present study, preventing aliasing effects. The spectral resolution is equal to half of the sampling rate divided by the number of spectral points, in our case 2048. Hence the spectral resolution is 0.0122. It is recalled that all these

magnitudes are expressed in dimensionless variables, i.e. $\Delta t = \Delta t_{dim}/(R/U_0)$ with Δt_{dim} the dimensional time in seconds and R the cylinder's radius. For this reason, in order to read from the spectra the frequency values normalized as the Strouhal number (i.e. in terms of the diameter), the frequencies have to be multiplied by two.

The spectra of u- and v-components are provided in the vicinity of the wall on the rear symmetry axis for the Reynolds numbers 200 and 300 (figures 36–38). The Strouhal number corresponding to the von Kármán instability is clearly obtained by the present simulation. As this is an absolute instability of the present wake flow (Huerre & Monkewitz 1990), the trace of the fundamental frequency exists in any point in the near wake. As Reynolds number increases, the amplification of odd harmonics ($3St$, $5St$ and $7St$) appears more and more pronounced on the v-component. Concerning the u-component spectra, the most striking characteristic is the appearance of the peak at $2f_s$ and its harmonics as the only predominant frequencies. This behaviour is due to the simultaneous effect of the two vortex rows (upper and lower) on the rear axis and it agrees with the theoretical study of Kovasznay (1949) who reports that the relative phase of second and first harmonics varies with the downstream distance: the first harmonic is asymmetric with respect to the x-axis and the second harmonic is symmetric. After Kovasznay, the velocity fluctuation distribution can be represented at any instant by the relation

$$u = u_1 \cos 2\pi(\zeta_1 + f_s t) + u_2 \cos 4\pi(\zeta_2 + 2f_s t),$$

where f_s is the Strouhal frequency, u_1 an odd function of y and u_2 an even function. ζ_1 and ζ_2 are almost linear functions of x. Our study is in agreement with the above considerations because we obtain that, for $y/D = 0$, the harmonic $2f_2$ is a mostly predominant frequency, observed on u-spectra on the rear axis of the cylinder (figures 36(c, d) for $Re = 200$ and figures 36(g, h) for $Re = 300$).

The comparison of two- and three-dimensional cases for $Re = 200$ shows an increase of the spectral level in the three-dimensional calculation. This phenomenon appears clearly on the v-component spectra and it illustrates an increase of the chaotic behaviour of the flow, under the non-inhibition of the three-dimensionality. This effect can also be seen for $Re = 300$ although it is weaker at this Reynolds number value. Hence, the flow is more perturbed in the three-dimensional case and this is due to the progressive development of finer-scale three-dimensional motion, as Reynolds number increases.

The loss of periodicity and of the coherent character far downstream occurs earlier in the three-dimensional case. For instance, on the u-component, no more frequency peaks can be seen at $x/D = 10.46$ in the three-dimensional case whereas at $x/D = 14.74$ in the two-dimensional case, peaks can still be seen.

The spectra of the velocity signals along the shear layers show clearly the enhancement of the first-harmonic frequency ($2f_s$), where f_s is the Strouhal number, as well as of higher-order harmonics. This effect is more pronounced as Re increase (figure 39). The presence of these harmonics is related to the interaction of the shear-layer smaller-scale vortices with the fundamental ones. The upper shear layer for instance is submitted to the forcing action of the oscillation of the separation point, in respect to f_s. As the shear layer farther downstream is self-excited by a frequency very close to the Strouhal number, an interaction occurs between it and the forcing frequency. According to the linear stability theory (Ho & Huerre 1984; Freymuth 1966), the harmonics are also amplified frequencies expected through this interaction.

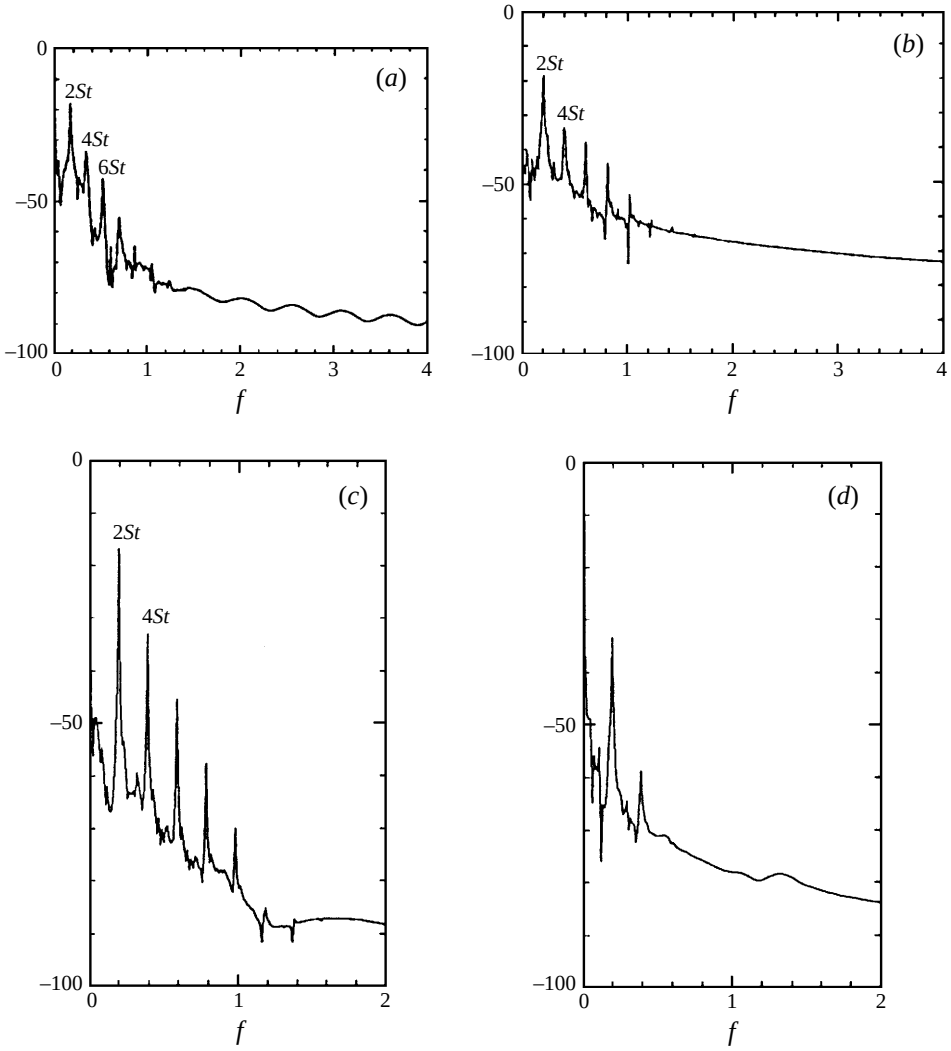

FIGURE 36(*a–d*). For caption see facing page.

Owing to the finer-scale motion developed in the shear layer and in the (x, z)- and (y, z)-planes as Reynolds number increases and owing to the elliptic character of the present flow, the amplification of the first harmonic is also present on the base pressure coefficient spectra (figures 38 *a* and 38 *b*), and it becomes more prominent for the higher Reynolds number values, as also discussed in § 6.3.

6.7. *Spatial evolution of the instability mechanism in the near wake*

In this subsection, based on a previous study of ours (Persillon *et al*. 1995 *b*; Persillon & Braza 1995), we perform a detailed analysis of the spatial evolution of the fundamental mode in the near wake, by means of the present direct numerical simulation using the complete Navier–Stokes equations system. It is recalled from the introduction that the existing experimental, theoretical and numerical studies in this topic have not yet investigated this process in the wake of a circular cylinder.

The amplification of the von Kármán mode in the near wake will be examined,

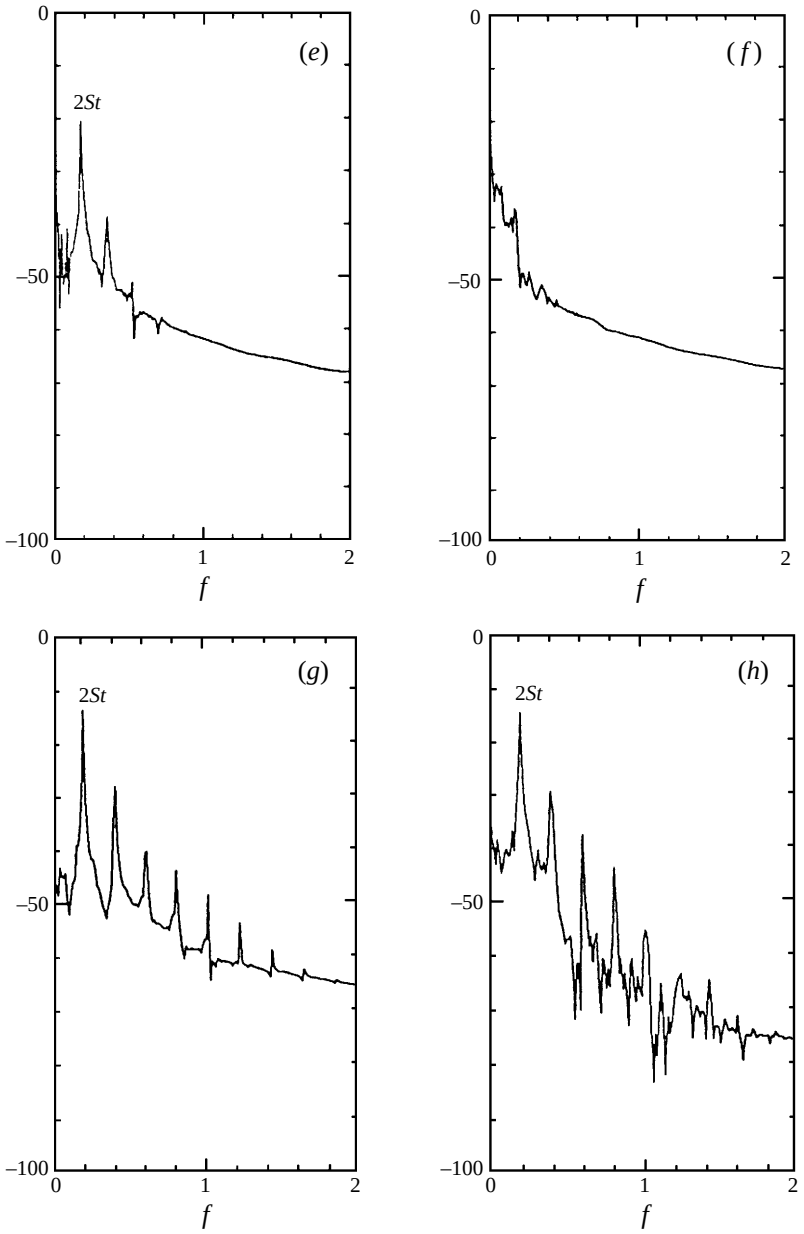

FIGURE 36. u-component spectra: (a) $x/D = 1.80, y/D = 0, Re = 200$, three-dimensional case; (b) as (a) but for $Re = 300$; (c) $x/D = 0.97, y/D = 0, Re = 200$, two-dimensional case; (d) as (c) but for $x/D = 14.78$; (e) $x/D = 0.97, y/D = 0, Re = 200$, three-dimensional case; (f) as (e) but at $x/D = 10.46$; (g) $x/D = 0.97, y/D = 0, Re = 300$, two-dimensional case; (h) as (g) but three-dimensional case.

under the three-dimensional effect and the strongly nonlinear character of the physical process, in order to provide the precise cartography of this instability mechanism in the Reynolds number range covering the *two* discontinuity regions.

This study is carried out by evaluating the spectrum of the u- and v-components at each grid point along two horizontal lines in the near wake: the rear symmetry

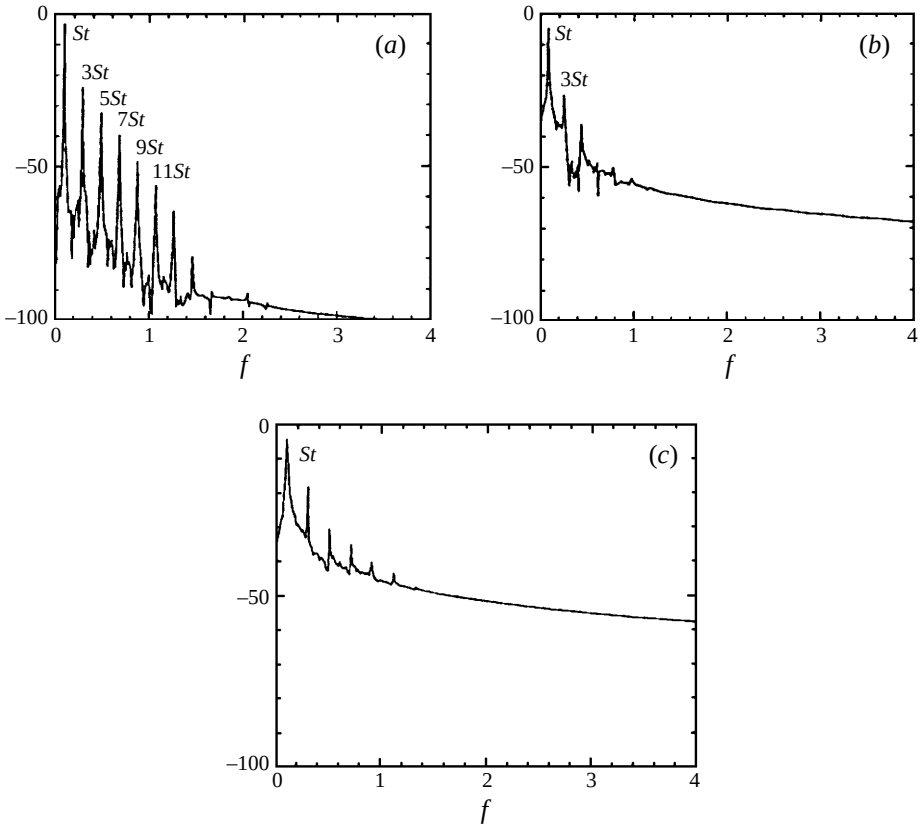

FIGURE 37. v-component spectra: (a, b) $x/D = 1.80, y/D = 0, Re = 200$, three-dimensional case; (c) as (a, b) but for $Re = 300$

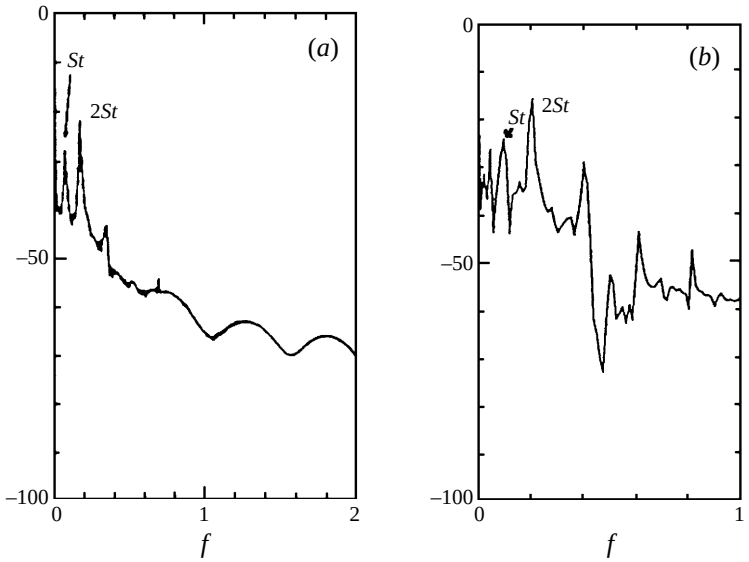

FIGURE 38. Spectra of the base-pressure coefficient: (a) $Re = 200$ and (b) $Re = 300$; three-dimensional case.

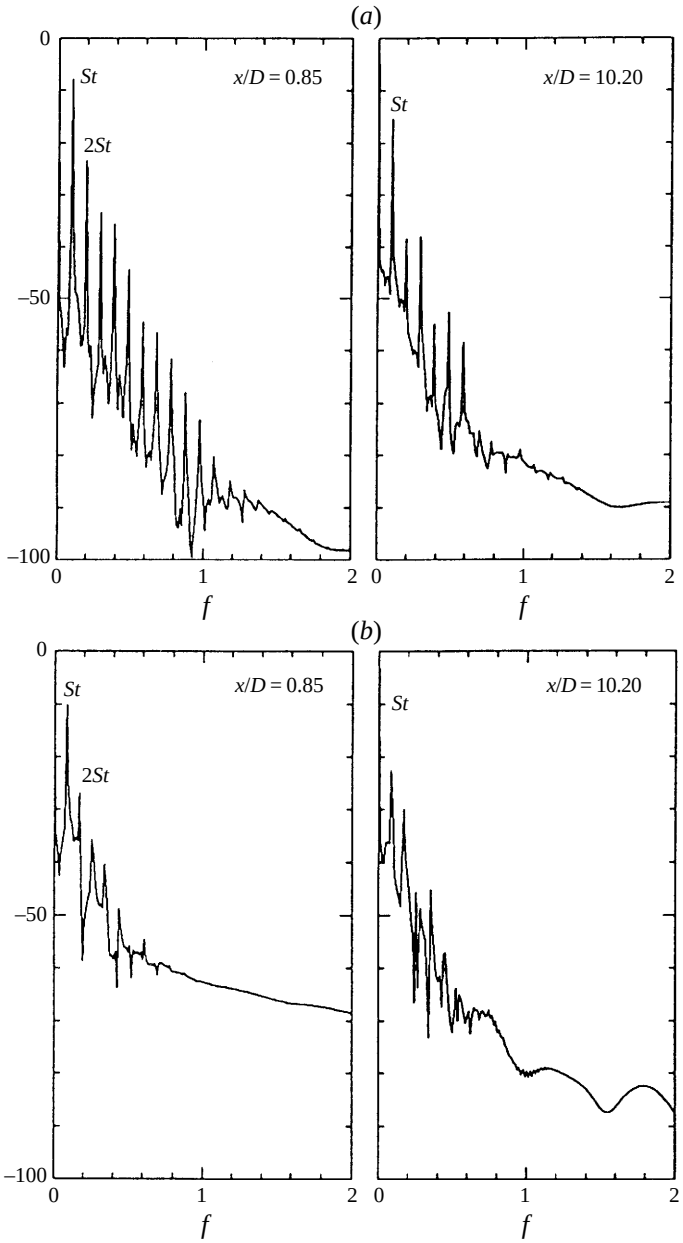

FIGURE 39. *u*-component spectra in the upper shear layer, $y/D = 0.5, x/D = 0.85, 10.20, Re = 200$: (*a*) two-dimensional case, (*b*) three-dimensional case.

axis and an horizontal line along the upper shear layer at $y/D = 0.5$. Each spectrum provides a maximum amplitude for the fundamental frequency which is plotted versus x/D.

A general characteristic obtained is that in each case the amplitude increases faster in the very near wake, it reaches a maximum and then decreases slowly (figure 40 *a*). Such a behaviour has already been point out by Mathis (1983), Mathis, Provansal & Boyer (1984) among others, based on an experimental approach.

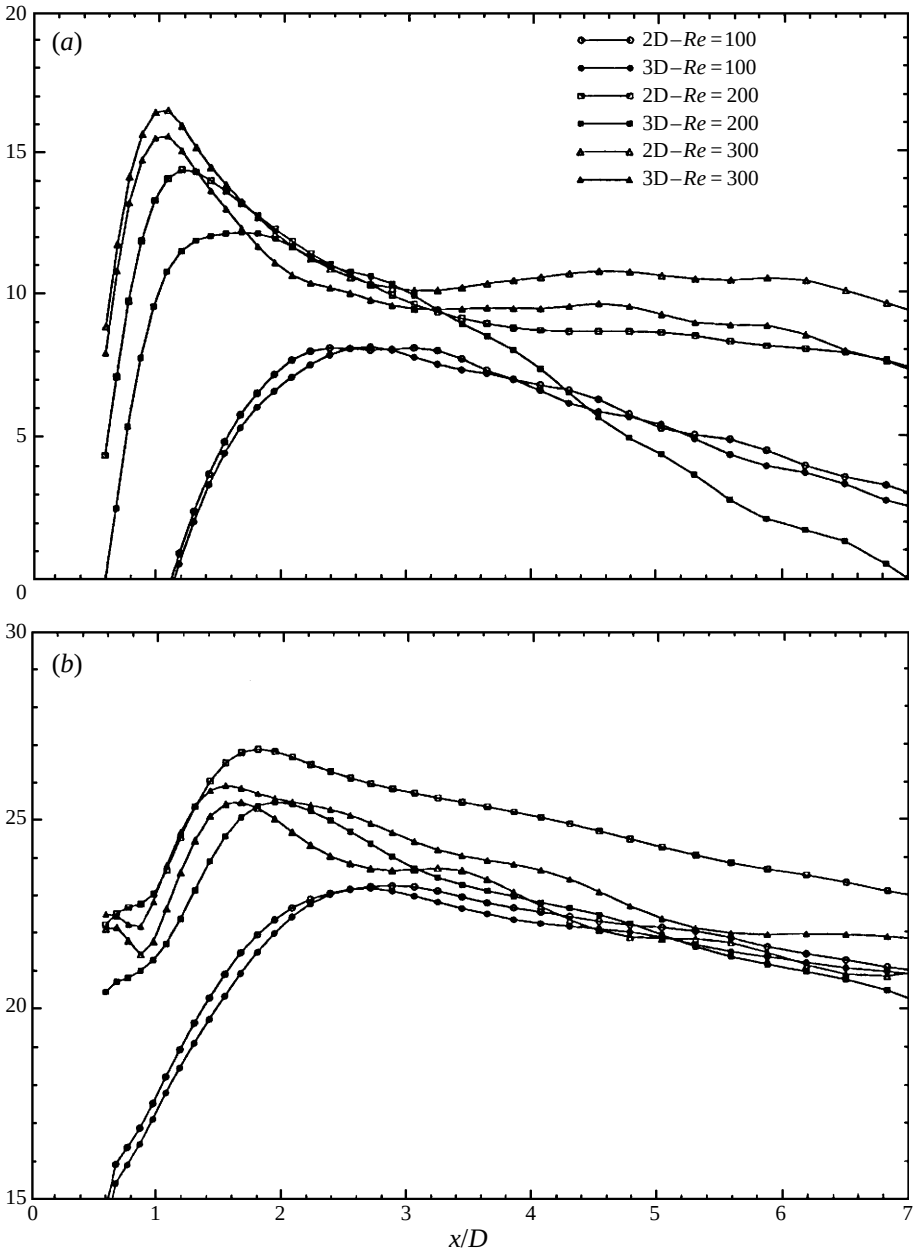

FIGURE 40. Spectral amplitude along the rear axis of (*a*) *u*-component, (*b*) *v*-component.

The position of the maximum amplitude of the *u*-component is different from that of the *v*-component. The fundamental frequency value is the same for all the components and all the positions (for a constant Reynolds number), except for the *u*-component on the rear axis which oscillates at $2f_s$ as it has been mentioned before. The maximum amplitude (A_{max}) of $2f_s$ is smaller than that of the fundamental mode.

Let us examine first the variations of the maximum amplitudes of the fundamental along the rear axis, without normalizing the values by the absolutely maximum

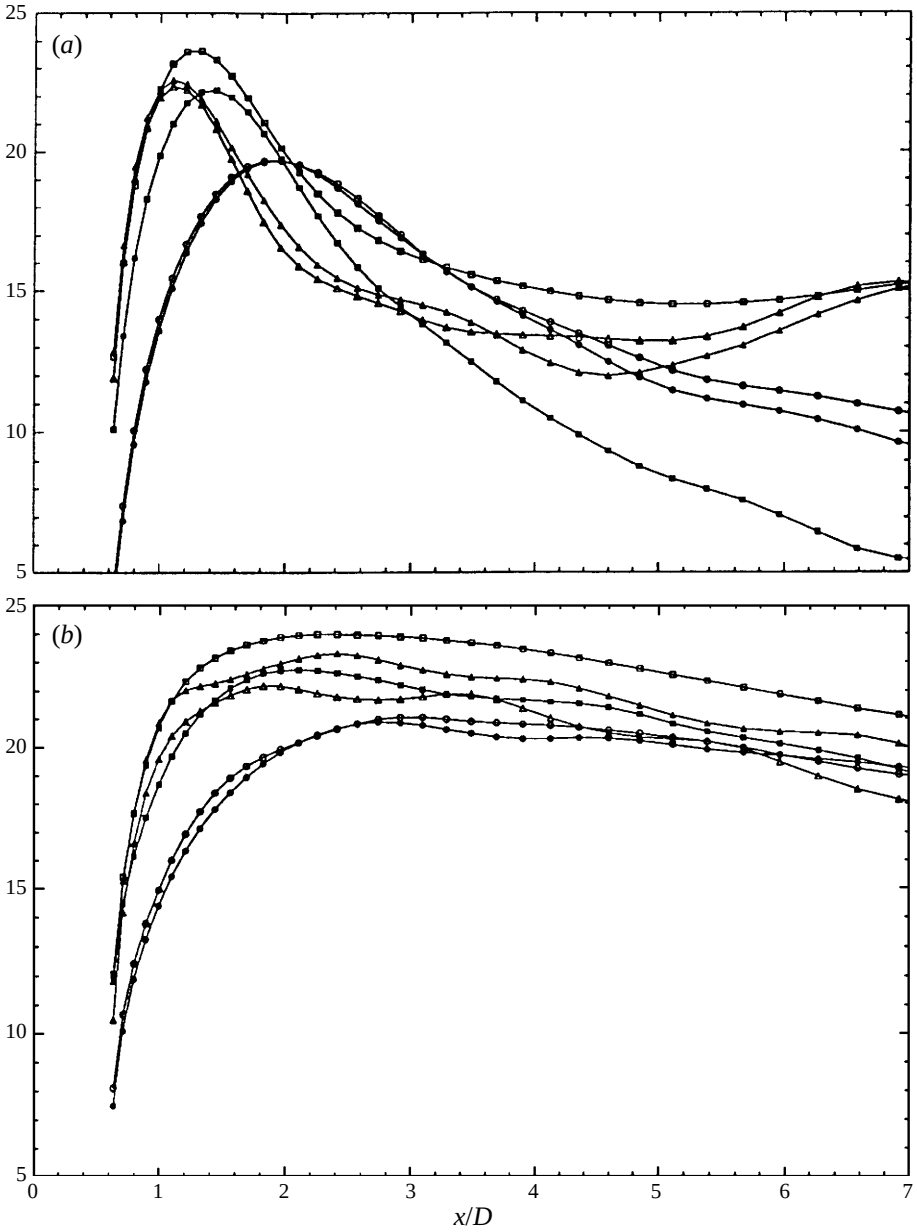

FIGURE 41. Spectral amplitude along the upper shear layer $y/D = 0.5$ of (*a*) *u*-component, (*b*) *v*-component. Symbols as figure 40.

value (figures 40*a* and 40*b*) from $Re = 100$ to $Re = 300$, i.e. within the discontinuities region. The *u*-component maximum amplitudes for the three-dimensional case are the lowest at $Re = 100$ and they increase monotonically at $Re = 200$ and $Re = 300$. The location of the maximum is found to be closer to the wall as Re increases. Considering the same variations for *v*-component, which is the most affected by the periodic motion and which is free from the 'masking' convection effect, we detect an almost non-monotonic variation within the discontinuity region. In-

deed, at $Re = 200$ (three-dimensional) the maximum amplification region has a value very close to the one at $Re = 300$. This can be related to the discussions concerning the discontinuity region, which illustrates a strikingly non-monotonic behaviour too.

The same behaviour of the maximum amplitude region is obtained in the upper shear layer region (figures 41 *a* and 41 *b*). Comparing the two- and three-dimensional approaches, we obtain very similar variations for $Re = 100$ and a considerable difference at $Re = 200$, where the three-dimensional case shows a striking decrease of the maximum amplitude, relatively to the two-dimensional case. The discrepancy at $Re = 300$ between the two- and three-dimensional cases is less pronounced. Hence, within the discontinuity region, we obtain the two following characteristics: a less rapid increase of the maximum amplitude as a function of Re and a considerable decrease of the maximum amplitude value in the three-dimensional case, compared to the two-dimensional case.

The same behaviour is obtained along the shear layer for the spectral amplitude variations (figure 41 *b*). The highest amplitudes are found for $Re = 200$, two-dimensional case. The steepest decreasing rate downstream is obtained for $Re = 200$, three-dimensional case This is linked to the behaviour discussed for the spectra, where the three-dimensional simulations allow a faster loss of coherence of the organized pattern. However, the periodic character persists much more for the v-velocity than for the u-velocity, as the u-component is hidden by the convection effect and therefore it is less sensitive to the travelling of the coherent vortices.

Secondly, we examine the behaviour of the instability process along the rear axis. The value and the position of A_{max} for the fundamental depends on the Reynolds number. It is precisely this dependence law that we discuss in the following. The spectral amplitude of the fundamental frequency is normalized by the maximum amplitude for each velocity component. The x-positions are normalized by X_{max}, the distance where the maximum amplitude appears (figures 42 *a* and 42 *b*). The increasing part of the curve to the maximum amplification corresponds to the establishment of the organized character of the process in respect to the von Kármán instability. It is found that this process is governed essentially by the same law for all the Reynolds numbers examined. The decreasing part of the curve illustrates the loss of the organized character downstream. As the organized pattern is more pronounced at the lower Reynolds number range, the slope of the decreasing part is found to increase from $Re = 100$ to 300. Nevertheless, a striking saturation effect is obtained beyond $Re = 200$.

Figure 43 shows the variation of X_{max} versus Reynolds number. We find that the position of the maximum amplitude approaches the cylinder as the Reynolds number increases. By the present three-dimensional complete Navier–Stokes equations approach we find that this variation is described by the law

$$X_{max} \sim Re^{-1/2}$$

as shown in figure 43.

In the same way, the variation of A_{max} versus Reynolds number is quantified by the law

$$A_{max} \sim Re^{1/2}.$$

It is interesting to note that a two-dimensional numerical study at low Reynolds number has been carried out by Zielinska & Wesfreid (1995) behind a triangle. The shape of the modes, the maximum amplitude evolution and its position as a function

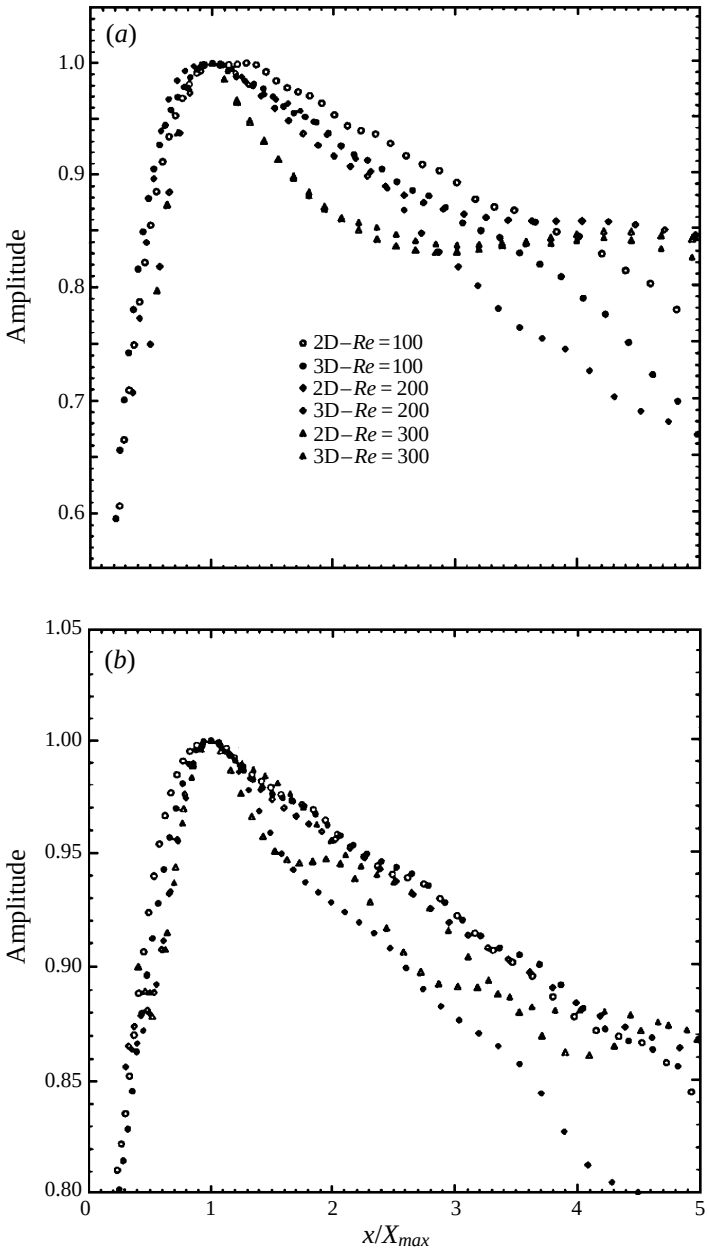

FIGURE 42. Normalized spectral amplitude versus x/X_{max}, along the rear axis: (*a*) *u*-component, (*b*) *v*-component,

of the Reynolds number agree with our study, although the body configuration is different. Concerning the normalized curve, they obtain the same kind of behaviour, which is also reported by Goujon-Durand *et al*. (1994), who have carried out an experimental study behind a trapezoidal body. They have also obtained similar laws for X_{max} and A_{max}. Hence, it seems that these features are universal and independent of the shape of the body.

In our present work, we establish the variation law of the maximum amplitude for

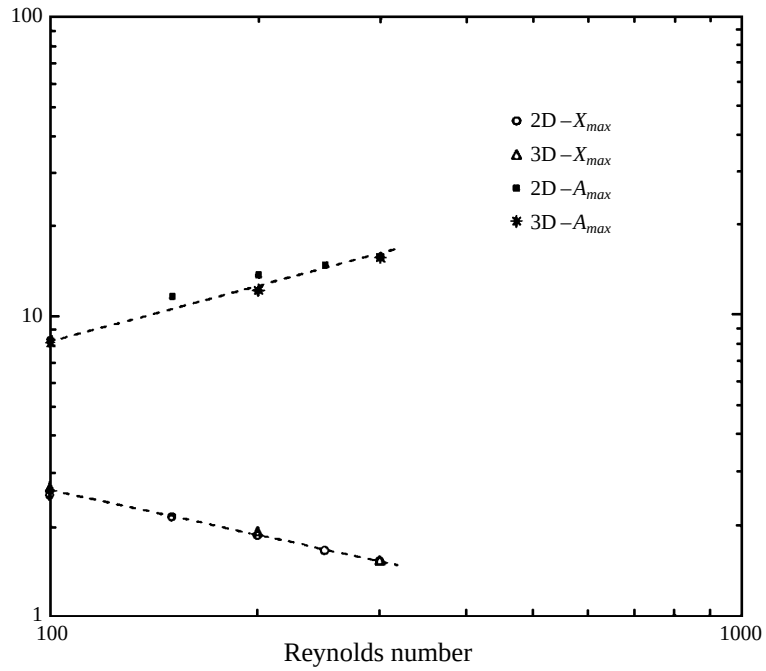

FIGURE 43. Variation law of X_{max} and A_{max} as functions of Reynolds number (logarithmic scales), $y/D = 0$.

the fundamental in the near wake and for the location of its maximum amplification as a function of Reynolds number, by taking into account the three-dimensional and nonlinear character of the flow transition.

6.8. *Critical Reynolds number of the first discontinuity*

The nature of the first discontinuity is hysteretic, as mentioned in the physical experiments by Williamson (1996*a*) and by Leweke & Provansal (1995). According to the stability theory, the related bifurcation has to be subcritical, whereas a smooth non-hysteretic bifurcation, as is the case of the first bifurcation (appearance of the alternating vortex pattern), is described as supercritical. The work by Noack & Eckelmann determined the critical Reynolds number at $Re = 170$, i.e. much earlier than the occurrence of the first discontinuity, according to the physical experiment. For these reasons they found that their transition was 'supercritical'. Barkley & Henderson have evaluated this critical Reynolds number as 188.5, from the linear stability analysis using Floquet equations and by imposing small disturbances. Their value places the critical Reynolds number later than the formation of the abrupt change in the experimental curve and, as expected, they described this process as a subcritical secondary instability. It was also expected that the linear theory places the critical threshold at higher values than the physical ones. Although the linear theory is an efficient methodology to assess critical values within a reasonable time, it is not sufficient to describe the nature of a transition process characterized by an abrupt step-like discontinuity. In the present work, we perform complete DNS simulations in the interval of Reynolds number 185–190. The results are presented on figure 44. The shape of the discontinuity as an abrupt change, as is the case in the experimental works, is clearly obtained, with a saturation effect at $Re = 187$, which is the critical

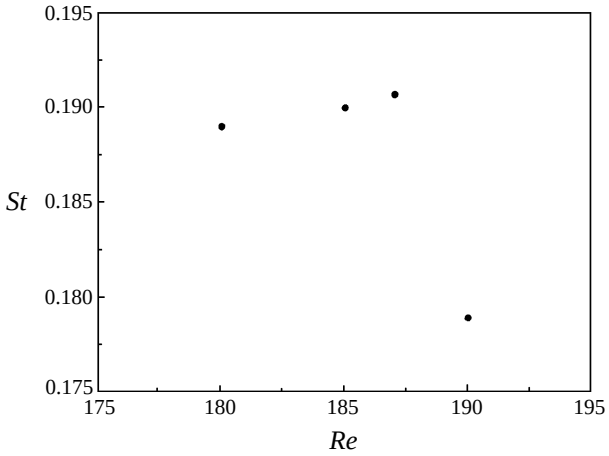

FIGURE 44. Strouhal number versus Reynolds number variation in the vicinity of the first discontinuity.

Reynolds number according to the present study. It is recalled that nothing has been introduced as perturbation to trigger this behaviour, which appears naturally through the Navier–Stokes equations system. As the fluctuations of the present flow have a finite amplitude, they interact nonlinearly in the system, simultaneously with small fluctuations which may be produced by the truncation errors. This approach, taking into account simultaneously the effects of all the possible ranges of fluctuations in the present system, as is also the case in the physical experiment, is able to set the critical Reynolds number earlier than the linear theory, but in the subcritical part of the process.

7. Conclusions

The present study contributes among other numerical and experimental studies to the knowledge of physical phenomena related with the three-dimensional transition to turbulence in a wake past a bluff body. The strategy adopted in this work consists of investigating the flow evolution produced spontaneously by the complete system of the Navier–Stokes equations, without observing the response of this system to a number of imposed perturbations, as the techniques of the stability theories do.

According to our objectives, this work dissociates the two-dimensional from the three-dimensional transition mechanisms appearing in the wake in the low Reynolds number range (100 to 300). It is clearly shown that the full Navier–Stokes equations system is able to predict an important transition feature occurring in the low Reynolds number range, beyond the first bifurcation: the frequency modulation in the Strouhal–Reynolds number relation, delimited by two clearly obtained discontinuities in this curve. It is shown that this transition feature is due to strictly three-dimensional effects. This is shown by using simultaneously the two-dimensional numerical simulation by the same code (its two-dimensional version). In addition, a very good agreement of the global parameters and the physical experiment is obtained.

While the few other three-dimensional numerical simulations appearing in the same period as our works have not yet predicted the shape of the whole discontinuity region, the present article shows the ability of the Navier–Stokes system to predict the formation of the overall region characterized by a frequency modulation in the *St–Re*

curve, followed by the rising part of the *St–Re* curve and showing the formation of the plateau effect, as observed in the physical experiment.

Moreover, this study provides an analysis of part of the phenomena related to the formation of the discontinuity region, based on quantified energy variations and on the evolution of the streamwise vorticity in the Reynolds number range 100 to 300. It is in particular shown that the frequency discontinuity region is associated with a discontinuity in the total kinetic energy distribution in the near wake, in the present Reynolds number range. This feature may contribute to an analysis of part of the physical phenomena which appear in the discontinuity region and it may be complementary to other views offered by linear stability theory or by oscillator model equations.

The present study provides the variation and decay properties of the onset of fluctuating motion in the near wake for the Reynolds numbers corresponding to an important transition state, due to purely three-dimensional effects. The quantification of these properties in the near wake concerns a crucial flow region, where the similarity laws are not valid. For these reasons this part of the study, performed by using the complete three-dimensional simulation, is useful for the understanding of the near wake structure past bluff bodies. It is remarkable that this kind of information has been the object of only experimental studies, concerning rather the far field of a wake and at much higher values of the Reynolds number. Therefore, the study of these mean properties is an original element of the present work.

Concerning the coherent structure development, the present study clearly shows, simultaneously with the development of the streamwise vortex structures, the persistance of the alternating vortex pattern over a long distance downstream. This is not the case for the majority of other ongoing studies on the three-dimensional transition around the cylinder. The authors believe that the attempt to reach high spanwise lengths should not involve the loss of a sufficient grid refinement, a risk if a higher spanwise size is preferred to the overall grid refinement. The grid refinement is not only needed in a reduced near-wall region, but in an extended region of several diameters around the cylinder, in order to preserve the physical representation of the alternating vortices. As the capabilities of present day supercomputers have a limit, a very careful compromise has to be made between these two aspects. This was the strategy chosen for the present work, for which a moderate spanwise length has been adopted, with a sufficiently extended fine-grid region. This ensured the prediction of the three-dimensional phenomena mentioned, without altering the alternating character of the main vortices, which is a fundamental property in these wake flows.

An original part of the present study has been made possible precisely due to the good compromise between these two aspects. One the one hand, it has been possible to track, for the first time at the present Reynolds number range, apart from the main alternating vortices, smaller-scale shear-layer instability vortices, from the three-dimensional simulation. Note that the trace of such structures is difficult to obtain experimentally at the present Reynolds number range, which actually characterizes the birth of the mixing-layer vortices, whose frequency is still very close to the Strouhal number. For this reason, tracking these structures experimentally is a more difficult task than for Reynolds number values beyond 2600 (as reported for instance in the pioneering visualizations of Crausse 1936).

On the other hand, by increasing the spanwise length from $2.25D$ to $3.72D$ the present study shows that a distortion of the main vortex rows occurs spontaneously and leads to the appearance of a wavy pattern qualitatively like mode A, of exper-

imental studies by Williamson (1992). Therefore, this study shows that the present spanwise waviness of the vortex street is an inherent feature of the three-dimensional transition for this flow, predictable by the complete system of the Navier–Stokes equations. Of course, this feature has to be examined in detail, through a parametric study on the spanwise length. In our ongoing studies and up to the limits of the supercomputers available, the investigation of the three-dimensional transition is in progress with higher spanwise lengths, but in this case too, the grid refinement is kept for all directions and in the whole domain.

Furthermore, the contour plots of the streamwise vorticity field clearly show the appearance of a distinct spanwise undulation of the main alternating eddies associated with the progressive birth of streamwise vortex loops. A drastic change of the overall pattern is obtained from Reynolds number 200 to 300, where the wavelength of the streamwise vortices is reduced as a function of Reynolds number. Indeed, the size of the streamwise vortices varies from $0.5D$ to $0.3D$ from $Re = 220$ to 300 and their wavelength from 3.2 to 0.7, with an abrupt change in the Reynolds number range 220–270. The fact of reduction of the length scales of the streamwise vortex structures is a feature also reported in the experimental visualizations by Williamson through the passage from mode A to mode B.

Another original part of this work, which to our knowledge appears for the first time in the literature, is the study of the amplification of the fundamental frequency, within the Reynolds number range corresponding to the discontinuities region. This paper quantifies in detail the spectral amplitude of the fundamental frequency along the rear axis and along the shear layer in the near wake, according to both the three-dimensional and the two-dimensional approaches.

It establishes the law of variation of the maximum spectral amplitude and of the location of this amplitude as a function of the Reynolds number. This is achieved by taking into account the nonlinearity and three-dimensionality of the physical process.

Moreover, in this study a way of establishing an accurate evaluation of the critical Reynolds number for the appearance of the first discontinuity by the complete nonlinear and three-dimensional approach is offered. The value of this number is found as 187 and its evaluation takes into account the influence of not only small-scale but especially of the finite-amplitude fluctuations, which are essentially related to the nature of the first discontinuity. For these reasons, the present study obtains the frequency drop earlier than the linear theories and closer to what is shown by the physical experiments.

The present work has been carried out in the group Ecoulements Monophasiques, Transitionnels and Turbulents (EMT2) of the Institut de Mécanique des Fluides de Toulouse (IMFT). The authors are grateful to the personnel of the two National Computer Centres of France, CNUSC and IDRIS for the computational time and the precious assistance provided to carry out this work and also the Cornell Supercomputing Center for having attributed part of CPU time and advises. They are also grateful to DRET-DGA, Délégation Générale pour l'Armement (post-doctoral grant n^o $93811 - 46/A000$) for having provided a one-year fellowship for H. Persillon at Cornell University, in the group of Professor Williamson, and to the French Ministry of Research and Education, for the attribution of the Doctoral fellowship of H. Persillon. This work has been substantially helped by the efforts of Dr G. Jin, for his principal contribution to the development of the two-dimensional version of the code ICARE, during his Doctorate thesis in IMFT, under the supervision of M. Braza. The authors are grateful for his precious help, related to the accomplishment of the

present study. The authors express many thanks to Professor Williamson (Cornell University) for the useful discussions and advises during the last six years. They are also grateful to Professors Ha Minh (IMFT), H. Boisson (IMFT) and M. Provansal (IRPHE, Institut de Recherches sur des Phénomènes Hors Equilibre, Marseille) for their advises and precious remarks which helped the progress of the present work. The authors acknowledge the contribution of Mr J. P. Bombaud, responsible for the computing facilities of the group EMT2 of IMFT for his continuous availability and help. They thank Mr Chorda (IMFT) for his contribution to configuration of part of the data. Mrs Rambouil and Mrs Domène of the reprographics and Mr Brunato of the photo-video service have provided a substantial help during the last five years.

REFERENCES

Albarède, P. & Provansal, M. 1995 The modelling of three-dimensional effects in the wake of a circular cylinder by a Guinzburg-Landau equation. *J. Fluid Mech.* **291**, pp. 191–222.

Amsden, A. A. & Harlow, F. H. 1970 The SMAC method: A numerical technique for calculating incompressible fluid flows. *Los Alamos Scientific Laboratory Rep.* LA-4370.

Barkley, D. & Henderson, R. 1996 Three-dimensional Floquet stability analysis of the wake of a circular cylinder. *J. Fluid Mech.* **322**, 215–241.

Bayly, B., Orszag & Herbert, T. 1988 Instability mechanisms in shear flow transition. *Ann. Rev. Fluid Mech.* **20**, 359–391.

Beaudan, P. & Moin, P. 1994 Numerical experiments on the flow past a circular cylinder at subcritical Reynolds number. *Tech. Rep. TF-62*. Thermosciences Division, Dept. of Mechanical Engineering, Stanford University.

Bloor, M. S. 1964 The transition to turbulence in the wake of a circular cylinder. *J. Fluid Mech.* **19**, 290–304.

Boisson, H. C. 1982 Développement de structures organisées turbulentes à travers l'exemple du sillage d'un cylindre circulaire. Thèse de Doctorat d'Etat-ès-Sciences, Institut National Polytechnique de Toulouse, France.

Braza, M. 1981 Simulation numérique du décollement instationnaire externe par une formulation vitesse-pression. Application à l'écoulement autour d'un cylindre. Thèse de Docteur-Ingénieur, Institut National Polytechnique de Toulouse, France.

Braza, M. 1986 Analyse physique du comportement dynamique d'un écoulement externe, décollé, instationnaire en transition laminaire-turbulente. Application: Cylindre circulaire. Thèse de Doctorat d'Etat-ès-Sciences, Institut National Polytechnique de Toulouse, France.

Braza, M. 1991*a* Méthode de résolution des équations de Navier-Stokes pour des écoulements three-dimensional ou two-dimensional instationnaires incompressibles: Code ICARE. *Rapport Interne TELET-IMFT* 72.

Braza, M. 1991*b* Etude expérimentale et numérique du décollement de la couche limite instationnaire sur modèle oscillant. Simulation numérique par résolution des équations de Navier-Stokes. *Annexe II du Rapport de Convention DRET-IMFM*.

Braza, M. 1994 Transition features in wake flows by means of numerical analysis. *Current Topics in the Physics of Fluids* **1**, 391–416.

Braza, M., Chassaing, P. & Ha Minh, H. 1985 A numerical study of the dynamics of different scale structures in the near wake of a circular cylinder in laminar to turbulent transition. In *Intl Conf. on Numerical Methods in Laminar and Turbulent Flow, Swansea, UK* (ed. C. Taylor *et al.*), pp. 672–686. Pineridge Press.

Braza, M., Chassaing, P & Ha Minh, H. 1986 Numerical study and physical analysis of the pressure and velocity fields in the near wake of a circular cylinder. *J. Fluid Mech.* **165**, 79–130.

Braza, M., Chassaing, P. & Ha Minh, H. 1990 Prediction of large-scale transition features in the wake of a circular cylinder. *Phys. Fluids* A **2**, 1461–1471.

Braza, M., Ha Minh, H. & Chassaing, P. 1984 Numerical simulation of the vortex shedding past a circular cylinder, using a pressure-velocity formulation. In *Intl Conf. on Numerical Methods for Transient and Coupled Problems, Venice, Italy* (ed. R. W. Lewis *et al.*), pp. 673–687. Pineridge Press.

Braza, M., Noguès, P., Tzabiras, G., & Ventikos, Y. 1994 Etude numérique d' écoulements turbulents 3D autour de sous-marins. *Rapport Final de la Convention DRET* 93/099.

Braza, M. & Persillon, H. & Sers, F. 1993 Prediction of certain transition characteristics in the wake of a circular cylinder in free and forced flow. In *IUTAM Symp. on Bluff-Body Wakes, Dynamics and Instabilities, Göttingen, Germany, 1992* (ed. H. Eckelmann, J. M. R. Graham, P. Huerre & P. A. Monkewitz), pp. 279–284. Springer.

Braza, M. & Sers, F. 1993 A parametric numerical simulation for the flow around a circular cylinder at low Reynolds numbers. Oral presentation and participation in the Report on the Session comparing computation of flow past circular cylinders with experimental data, by J. M. R. Graham, In *IUTAM Symp. on Bluff-Body Wakes, Dynamics and Instabilities, Göttingen, Germany, 1992* (ed. H. Eckelmann, J. M. R. Graham, P. Huerre & P. A. Monkewitz), pp. 317–324.

Coutanceau, M. & Bouard, R. 1977 Experimental determination of the main features of the viscous flow in the wake of a circular cylinder in uniform translation. Part 1. Steady flow. *J. Fluid Mech.* **79**, 231–256.

Crausse, E. 1936 Contribution expérimentale à l'étude des phénomènes transitoires et périodiques se produisant dans les lignes en mouvement. Thèse de Doctorat d'Etat-ès-Science, Université de Toulouse, France.

Crausse, E. & Baubiac, J. 1931 Sur l'application d'une méthode d'enregistrement à l'étude des tourbillons se produidant dans les liquides *C. R. Acad. Sci. Paris* **192**, 1355.

Daube, O. & Ta Phuoc Loc 1978 Etude numérique d'écoulements instationnaires de fluide visqueux, incompressible autour de corps profilés par une méthode combinée d'ordre O(2) et O(4). *J. Méc.* **17**, 651–678.

Dennis, C. S. R. & Chang, G. 1970 Numerical solution for steady flow past a circular cylinder at Reynolds numbers up to 100. *J. Fluid Mech.* **12**, 471–489.

Douglas, J. 1962 Alternating direction methods for three space variables. *Numerische Mathematik* **4**, 41–63.

Dusek, J., Le Gal, P. & Fraunié, P. 1994 A numerical and theoretical study of the first Hopf bifurcation in a cylinder wake. *J. Fluid Mech.* **264**, 59–80.

Eckelmann, H., Graham, J. M. R., Huerre, P. & Monkewitz, P. A. 1993 Selected Papers, *IUTAM Symp. on Bluff-Body Wakes, Dynamics and Instabilities, Göttingen, Germany, 1992*. Springer.

Eisenlohr, H. & Eckelmann, H. 1989 Vortex splitting and its consequences in the vortex street wake of cylinder at low Reynolds numbers. *Phys. Fluids* A **1**, 189–192.

Freymuth, M. 1966 On transition in a separated laminar boundary layer. *J. Fluid Mech.* **25**, 683–704.

Gaster, M. 1969 Vortex shedding from slender cones at low Reynolds numbers. *J. Fluid Mech.* **38**, 563–576.

Gerrard, J. H. 1966 The three-dimensional structure of the wake of a circular cylinder. *J. Fluid Mech.* **25**, 143–164.

Gerrard, J. H. 1978 The wake of cylindrical bluff bodies at low Reynolds number *Phil. Trans. R. Soc. Lond.* A **288**, 351.

Goujon-Durand, S., Jenffer, P. & Wesfreid, J. E. 1994 Downstream evolution of the Bénard-von Kármán instability. *Phys. Rev.* E **50**, 308–313.

Grove, A. S., Shair, F. H., Petersen, E. E & Acrivos, A. 1964 An experimental investigation of the steady separated flow past a circular cylinder. *J. Fluid Mech.* **19**, 60–80.

Hama, F. R. 1957 Three-dimensional vortex pattern behind a circular cylinder. *J. Aeronaut. Sci.* **24**, 156.

Hamielec, A. & Raal, J. 1969 Numerical studies of viscous flow around circular cylinders. *Phys. Fluids* **12**, 11–17.

Ha Minh, H. 1979 Application de la méthode implicite des directions alternées (ADI) à la résolution des équations de Navier–Stokes autour d'un cercle. *Rep. IMFT-TELET* M3-25.

Ha Minh, H., Boisson, H. C. & Martinez, G. 1980 Unsteady mixed convection heat transfer around a circular cylinder. *Trans. ASME: J. Heat Transfer* **13**, 35–44.

Harlow, F. H. & Welch, J. E. 1965 Numerical calculation of the time-dependent viscous incompressible flow of fluids with free surface. *Phys. Fluids* **8**, 2182–2186.

Henderson, R. 1995 Details of the drag curve near the onset of vortex shedding. *Phys. Fluids* **7**, 2102–2104.

Henderson, R. & Barkley, D. 1996 Secondary instability in the wake of a circular cylinder. *Phys. Fluids* **8**, 1683–1685.

Hinze, J. 1975 *Turbulence*. MacGraw-Hill.

Ho, C. M. & Huerre, P. 1984 Perturbed free shear layers. *Ann. Rev. Fluid Mech.* **16**, 365.

Huerre, P. & Monkewitz, P. A. 1990 Local and global instabilities in spatially developing flows. *Ann. Rev. Fluid Mech.* **22**, 473–537.

Jackson, C. P. 1987 A finite-element study of the onset of vortex shedding in flow past variously shaped bodies. *J. Fluid Mech.* **182**, 23–45.

Jain, P. C. & Rao, K. S. 1969 Numerical solution of unsteady viscous incompressible fluid flow past a circular cylinder. *Phys. Fluids Suppl. II* **12**, 57–64.

Jin, G. & Braza, M. 1993 A non-reflecting outlet boundary condition for incompressible unsteady Navier-Stokes calculations. *J. Comput. Phys.* **107**, 239–253.

Jin, G. & Braza, M. 1994 A two-equation turbulence model for unsteady separated flows around airfoils. *AIAA J.* **32**, 2316–2320.

Jordan, S. K. & Fromm, J. E. 1972 Oscillatory drag, lift and torque on a circular cylinder in a uniform flow. *Phys. Fluids* **15**, 371–376.

Karniadakis, G. E. & Triantafyllou, G. S. 1992 Three-dimensional dynamics and transition to turbulence in the wake of bluff objects. *J. Fluid Mech.* **238**, 1–30.

König, M., Noack, B. R. & Eckelmann, H. 1993 Discrete shedding modes in the von Kármán vortex street. *Phys. Fluids* A **5**, 1846–1848.

Kovasznay, L. S. G. 1949 Hot-wire investigation of the wake behind cylinders at low Reynolds numbers. *Proc. R. Soc. Lond.* A **198**, 174–190.

Landau, L. D. & Lifschitz, E. 1971 *Mécanique des Fluides* (ed. Mir.)

Lasheras, J.C. & Meiburg, E. 1990 Three-dimensional vorticity modes in the wake of a flat plate. *Phys. Fluids* A **2**, 371–380.

Leweke, T. & Provansal, M. 1995 The flow behind rings: bluff body wakes without end effects. *J. Fluid Mech.* **288**, 265–310.

Lin, C., Pepper, D. & Lee, S. 1976 Numerical methods for separated flow solutions around a circular cylinder. *AIAA J.* **14**, 900-907.

Mansy, H., Yang & P. Williams, D. R. 1994 Quantitative measurements of spanwise periodic, three-dimensional structures in the wake of a circular cylinder. *J. Fluid Mech.* **270**, 277–296.

Martinez, G. 1978 Caractéristiques dynamiques et thermiques de l'écoulement autour d'un cylindre circulaire à nombre de Reynolds modéré. Thèse de Docteur-Ingénieur, Institut National Polytechnique de Toulouse, France.

Mathis, C. 1983 Propriétés des composantes de vitesse transverses dans l'écoulement de Bénard-von Kármán aux faibles nombres de Reynolds. Thèse de Doctorat, Université d'Aix-en-Provence, France.

Mathis, C., Provansal, M. & Boyer, L. 1984 The Benard-von Kármán instability: an experimental study near the threshold. *J. Phys. Lett. Paris* **45**, 483.

Miller, G. D. & Williamson, C. H. K. 1994 Control of 3D phase dynamics in a cylinder wake. *Exps. Fluids* **18**, 26.

Mittal, R. & Balachandar, S. 1995 Effect of three-dimensionality of the lift and drag of nominally two-dimensional cylinders. *Phys. Fluids* **7**, 1841.

Noack, B. R. & Eckelmann, H. 1994 A global stability analysis of the steady and periodic cylinder wake. *J. Fluid Mech.* **270**, 297–330.

Noguès, P. 1995 Prédétermination d'écoulements turbulents de type sillage instationnaire two-dimensional et autour de configurations three-dimensional de sous-marin à géométrie quelconque. Thèse de Doctorat, Institut National Polytechnique de Toulouse, France.

Patera, A. T. 1984 A spectral-element method for fluid dynamics; laminar flow in a channel expansion. *J. Comput. Phys.* **54**, 468–488.

Peaceman, D. W. & Rachford, H. H. 1955 The numerical solution of parabolic and elliptic differential equations. *Japan Soc. Indust. Appl. Maths* **3**, 28–41.

Persillon, H. 1995 Analyse Physique par simulation numérique bi- et tri-dimensionnelle de la transition laminaire-turbulente dans l'écoulement autour d'un cylindre. Thèse de Doctorat, Institut National Polytechnique de Toulouse, France.

Persillon, H. & Braza, M. 1995 Etude de la transition tridimensionnelle du sillage d'un cylindre circulaire à faible nombre de Reynolds. *Congrès Français de Mécanique, Strasbourg.*

Persillon, H. & Braza, M. 1996 Physical analysis of the three-dimensional transition to turbulence in the flow around a circular cylinder by means of Direct Numerical Simulation. In *Advances in Turbulence, Sixth European Turbulence Conference-ETC-VI, Lausanne, Switzerland*. (ed. S. Gavrilakis, L. Machiels, & P. A. Monkewitz). Kluwer.

Persillon, H., Braza, M., Ha Minh, H. & Williamson, C. 1995*a* Prediction of three-dimensional transition in the flow past a circular cylinder at low Reynolds number. In *Tenth Turbulent Shear Flow Conference, Penn-State University, USA*. (ed. F. Durst *et al.*). Penn State University Press.

Persillon, H., Braza, M., Ha Minh, H. & Williamson, C. 1995*b* Non-linear instability and three-dimensional transition in the flow past a circular cylinder at low Reynolds number. In *IUTAM Symp. on Non-linear Instability and Transition in 3D Boundary Layer, Manchester, UK* (ed. P. W. Duck & P. Hall), pp. 207–216. Kluwer.

Persillon, H., Braza, M. & Jin, G. 1995*c* Prediction of transition features in the flow past a circular cylinder in three-dimensions. In *Fifth Intl Offshore and Polar Engineering Conf., The Hague, The Netherlands* (ed. J. S. Chung, J. Wardenier & H. Maeda). Intl Soc. Offshore and Polar Engrs.

Prasad, A. & Williamson, C. H. K. 1996 The instability of the separated shear layer from a bluff body. *Phys. Fluids* **8**, 1347–1349.

Prasad, A. & Williamson, C. H. K. 1997 Three-dimensional effects on turbulent bluff-body wakes. *J. Fluid Mech.* **343** 235–265.

Prigogine, I. 1982 *Physique, Temps et Devenir*. Masson.

Provansal, M., Mathis C. & Boyer, L. 1987 Bénard-von Kármán instability: transient and forced regimes. *J. Fluid Mech.* **182**, 1–22.

Reynolds, O. 1894 On the dynamical theory of incompressible viscous fluids and the determination of the criterion. In *Conf. R. Soc. of Lond., May 21, 1894* and *Phil. Trans. R. Soc. Lond.* A **123**.

Roshko, A. 1954 On the drag and shedding frequency of two-dimensional bluff bodies. *NACA Tech. Note* 3169.

Sers, F. 1992 Etude de mécanismes de transition two-dimensional dans le sillage d'un cylindre, à des nombres de Reynolds modérés. *Mémoire de Diplôme d'Etudes Approfondies, Institut National Polytechnique de Toulouse*.

Son, J. S. & Hanratty, T. J. 1969 Numerical solution for the flow around a circular cylinder at Reynolds numbers of 40, 200 and 500. *J. Fluid Mech.* **35**, 369–386.

Stuart, J. T. 1960 On the nonlinear mechanics of wave disturbances in stable and unstable parallel flows. Part 1. *J. Fluid Mech.* **9**, 353–370.

Szepessy, S. & Bearman, P. W. 1992 Aspect ratio and end plate effects on vortex shedding from a circular cylinder. *J. Fluid Mech.* **234**, 191–217.

Ta Phuoc Loc 1975 Etude numérique de l'écoulement d'un fluide visqueux incompressible autour d'un cylindre fixe ou en rotation *J. Méc.* **14**, 109–134.

Thoman, D. C & Szewczyk, A. A. 1969 Time-dependent viscous flow over a circular cylinder. *Phys. Fluids* **2**, 76–86.

Thompson, J. F., Thames, F. C. & Mastin, C. W. 1974 An automatic numerical generation of body-fitted curvilinear coordinates system for flows containing any number of arbitrary two-dimensional bodies. *J. Comput. Phys.* **15**, 299–319.

Thompson, M., Hourigan, K. & Sheridan, J. 1994 Three-dimensional instabilities in the cylinder wake. In *Intl Colloq. on Jets, Wakes, Shear Layers, Melbourne,* Paper 10.

Townsend, A. A. 1956 *The Structure of Turbulent Shear Flow*. Cambridge University Press.

Trichet, P. 1975 Etude de l'écoulement autour d'un cylindre et de son sillage proche. Thèse de 3^{eme} cycle, Université Paul Sabatier, Toulouse, France.

Tritton, D. J. 1971 A note on vortex streets behind circular cylinders at low Reynolds number *J. Fluid Mech.* **45**, 203–208.

Tuann, S. Y. & Olson, M. 1978 Numerical studies of the flow around a circular cylinder by a finite-element method. *J. Computers Fluids* **6**, 219–240.

Uberoi, M. S. & Freymuth, P. 1969 Spectra of turbulence in wakes behind circular cylinders. *Phys. Fluids* **12**, 1359–1363.

Van Dyke, M. 1982 *An Album of Fluid Motion*. Parabolic Press.

Waleffe, F. 1990 On the three-dimensional instability of strained vortices. *Phys. Fluids* A **2**, 76–80.

Wei, T. & Smith, C. R. 1986 Secondary vortices in the wake of circular cylinders *J. Fluid Mech.* **169**, 513–533.

Wieselsberger, E. 1921 Neuere Feststellungen uber die Gesetze des Flussigkeits und Luftwiderstand. *Physik Z.* **22**, 321.

Williamson, C. H. K. 1987 Three-dimensional transition in the near wake of a cylinder. *Bull. Am. Phys. Soc.* **32**, 2098.

Williamson, C. H. K. 1988 *a* Defining a universal and continuous Strouhal-Reynolds number relationship for the laminar vortex shedding of a circular cylinder. *Phys. Fluids* **31**, 2742.

Williamson, C. H. K. 1988 *b* The existence of two stages in the transition to three-dimensionality of a cylinder wake. *Phys. Fluids* **31**, 3165–3168.

Williamson, C. H. K. 1989 Oblique and parallel mode of vortex shedding in the wake of a cylinder at low Reynolds numbers. *J. Fluid Mech.* **206**, 579–627.

Williamson, C. H. K. 1992 The natural and forced formation of spot-like vortex dislocations in the transition of a wake. *J. Fluid Mech.* **243**, 393–441.

Williamson, C. H. K. 1995 Vortex dynamics in the wake of a cylinder. In *Vortices* (ed. S. Green), chap. 5. Kluwer.

Williamson, C. H. K. 1996 *a* Vortex dynamics in the cylinder wake. *Ann. Rev. Fluid Mech.* **28**, 477–539.

Williamson, C. H. K. 1996 *b* Three-dimensional wake transition. *J. Fluid Mech.* **328**, 345–407.

Williamson, C. H. K. & Roshko, A 1990 Measurements of base pressure in the wake of a cylinder at low Reynolds numbers. *Z. Flugwiss. Weltraumforsch.* **14**, 38–46.

Wu, J., Sheridan, J., Welsh, M. C, Hourigan, K. & Thompson, M. 1994 Longitudinal vortex structures in a cylinder wake. *Phys. Fluids* **6**, 2883–2885.

Zhang, H. & Fey, U. & Noack, B. R. & Eckelmann, H. 1995 On the transition of the circular cylinder. *Phys. Fluids* **7**, 779–794.

Zielinska, B. J. A. & Wesfreid, J. E. 1995 On the spatial structure of global modes in wake flow. *Phys. Fluids* **7**, 1418–1424.